Growing Diamond on Unusual Substrates

University of BRISTOL

Edmund Jack William Smith

School of Chemistry

University of Bristol

A dissertation submitted to the University of Bristol in accordance with the requirements for award of the degree of Doctor of Philosophy in the Faculty of Science

October 2021

Word count: 44682

Abstract

Diamond growth *via* chemical vapour deposition (CVD) is a powerful method, unlocking diamond's extreme properties to be used for a huge range of applications. Within this thesis, CVD diamond growth is performed on a variety of uncommon substrates.

Nanostructured surfaces can have bactericidal properties, and prior work has shown that by diamond-coating a particular nanostructured material – black silicon – can be an effective means to enhance the bactericidal properties. Fluorine-termination of the surfaces was able to enhance the ability of black silicon and diamond-coated black silicon to kill bacteria and resist bacterial growth.

Gallium nitride has begun to see demand for use in high-electron-mobility transistors (HEMTs) but is currently limited by the difficulty in removing the generated heat from these devices. With a specialised seeding technique using a mixture of micro- and nano-crystalline diamond and an aluminium nitride interlayer, diamond was grown with a very low thermal resistance at the interface ($TBR_{eff} = 1.41 \pm 0.35$ m^2 K GW^{-1}), almost an order of magnitude lower than the current state-of-the-art.

Block copolymers self-assembled into micelles were explored as a means of producing nano- to micro-scale templated diamond with control over the shape and size of the resultant structures. In order for growth to occur reliably, a step was developed to convert the polymer into a suitable diamond seeding. Using these micelles, many of the parameters commonly used in diamond growth were analysed from a unique perspective.

Growth areas larger than those usually available for research on diamond CVD are required for diamond to be of use in most industrial settings. Additionally, as an appendix, an older piece of equipment was converted into a hot filament reactor capable of high-quality growth on 50 × 50 mm substrates, with the potential to grow over 150 × 150 mm substrates.

Acknowledgements

There can be no doubt – without Prof. Paul May, I would never have been able to do this Ph.D. From my first summer project back in 2014, Paul has inspired me to love the field of CVD diamond, and it has been a joy to study and learn from him over the course of so many years. He has always been there to support me, both academically in one of our "do you have a moment?" chats in his office that inevitably lasted half an hour, and on a more personal level over a meal on a Friday lunchtime or at the bar during a conference.

BUDGie was always full of incredible people who could be relied on to lend a hand to help or an ear to listen. Dom made every conference so much better and every hour of waiting for the reactor to run so much more fun; I certainly couldn't have made it to the end without him. Max, Gary, Limin, Fabian, Ramiz, Gulnur, Robbie, Michael, Sophie, Matt, Hugo, Ben, Alex – every one of you made my time doing this Ph.D better. To the undergraduate students who got lumbered with me – thank you for doing the grunt work and listening to me prattle on.

James Smith and Ed Aldred deserve a mention too, as they both were always on hand to help fix some technical problem that we had no idea about, an ever-calming presence among the chaos of the lab. Thanks to Paul C., Paul D., Adrian and Aide of the workshops for all the help in making the complicated things I decided I needed. Thanks also to those who helped me gather data – in particular JC, who is a veritable wizard of SEM and helped me get most of the stunning images presented here.

Speaking of facilities, Rob Harniman, who started out as just my local AFM guy, has been incredible. I can't thank him enough for how he has inspired me and motivated me; what started out as a minor passing side project and ended up being the single piece of research I am most proud of. What we have achieved together is something I will always remember fondly.

To the many friends outside of work, be they *the chaps*, those from undergrad, from school, or even from a certain MMORPG, you've supported me more than I could ever ask for. You're all wonderful people I feel fortunate to be able to call friends.

And of course, I have to thank my family. Mum and Dad: without them, I would not be who I am. They gave me every opportunity they could, and I hope that I have made them proud. I could never thank them enough.

To think, all this just so I can say "Look, I'm a doctor, not an escalator".

Author’s declaration

I declare that the work in this dissertation was carried out in accordance with the requirements of the University's Regulations and Code of Practice for Research Degree Programmes and that it has not been submitted for any other academic award. Except where indicated by specific reference in the text, the work is the candidate's own work. Work done in collaboration with, or with the assistance of, others, is indicated as such. Any views expressed in the dissertation are those of the author.

SIGNED: ..... DATE: .....

Table of Contents

Publications

O. Dunseath, E. Smith, T. Al-Jeda, J. Smith, S. King, P. May, A. Nobbs, G. Hazell, C. Welch and B. Su, Studies of Black Diamond as an antibacterial surface for Gram Negative bacteria: the interplay between chemical and mechanical bactericidal activity, *Scientific Reports*, 9 (2019), 8815.

This publication was on the first set of antibacterial black diamond experiments discussed in Chapter 3. Contributions to this paper was experimental design, growth of samples used, data acquisition and review of the manuscript.

W. Waller, J. Pomeroy, D. Field, E. Smith, P. May and M. Kuball, Thermal boundary resistance of direct van der Waals bonded GaN-on-diamond, *Semiconductor Science and Technology*, 35 (2020), 095021.

This publication is a small part of Chapter 4, showing the growth of diamond onto GaN. Contributions were in producing the diamond-on-GaN films used and review of the manuscript.

E. Smith, A. Piracha, D. Field, J. Pomeroy, G. Mackenzie, Z. Abdallah, F. Massabuau, A. Hinz, D. Wallis, R. Oliver, M. Kuball and P. May, Mixed-size diamond seeding for low-thermal-barrier growth of CVD diamond onto GaN and AlN, *Carbon*, 167 (2020), 620.

This publication makes up a significant portion of Chapter 4.

N. Norouzi, W. Woudstra, E. Smith, G. Zulpukarova, K. Yao, V. Damle, R. Schirhagl, P. May, T. Kamp, Antimicrobial studies of black silicon and black diamond using Gram-positive bacteria, *ACS Applied Material and Interfaces*, under submission.

This publication comprises of the results from the latter half of Chapter 3. Contributions to this paper were in experimental design, growth of samples used, data acquisition and review of the manuscript.

List of tables

List of figures

Chapter 1 - Introduction

1.1 Diamond and its diverse properties

Diamond is well known as a precious material, historically mainly due to its scarcity and its beauty when used for jewellery [1]. However, its vast array of extreme properties has seen diamond gain attention for use in scientific and engineering applications; of relevance in this work is diamond's high thermal conductivity (2×10^3 W m^{-1} K^{-1}), very low thermal expansion coefficient (1×10^{-6} K), extreme mechanical hardness (90 GPa) and modifiable electrical conductivity – ranging from undoped diamond being highly insulating (10^{13} Ω cm) to doped diamond being a wide-band semiconductor of 5.4 eV, as well as diamond being chemically and biologically inert [2]. For a more in-depth discussion of diamond's history and wide range of properties, references [2] and [3] are recommended, but a concise summary is presented here.

Diamond is a tetrahedral sp^3-hybridised lattice of carbon with a 3-dimensional structure. This is unlike graphite – the most common allotrope of carbon – which has a layered 2-dimensional sp^2-hybridised structure. Both structures are shown in figure 1.1. Graphite is more thermodynamically stable than diamond – making diamond a metastable allotrope in standard conditions – but the large activation barrier for interconversion effectively prohibits diamond from converting into graphite in mild conditions [4].

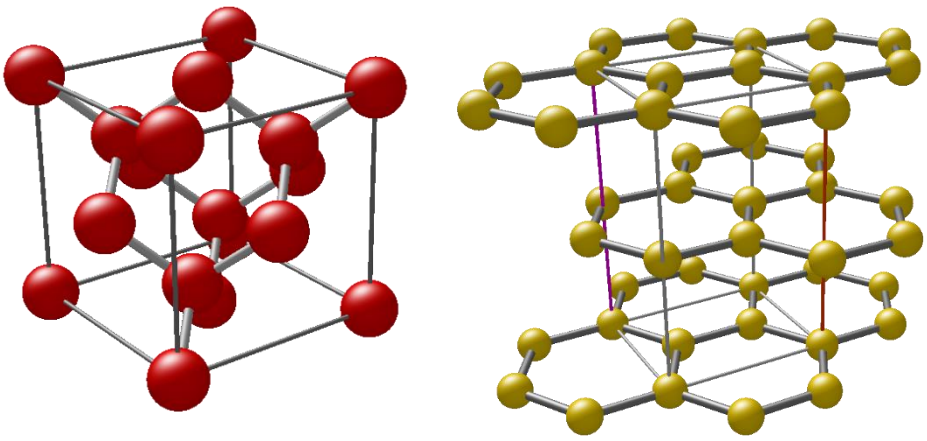

Figure 1.1: Structure of diamond (left) and graphite (right).

Carbon's two main solid phases can exist in a wide range of pressures and temperatures, overlapping as metastable forms, shown in Figure 1.2. The existence of the metastable allotropes is driven by the conditions required for the conversion between the forms; the activation energy required to convert diamond to graphite without a catalyst is 367 kJ mol^{-1}, so the rate of reaction is effectively zero at temperatures below 2000 K. [5]

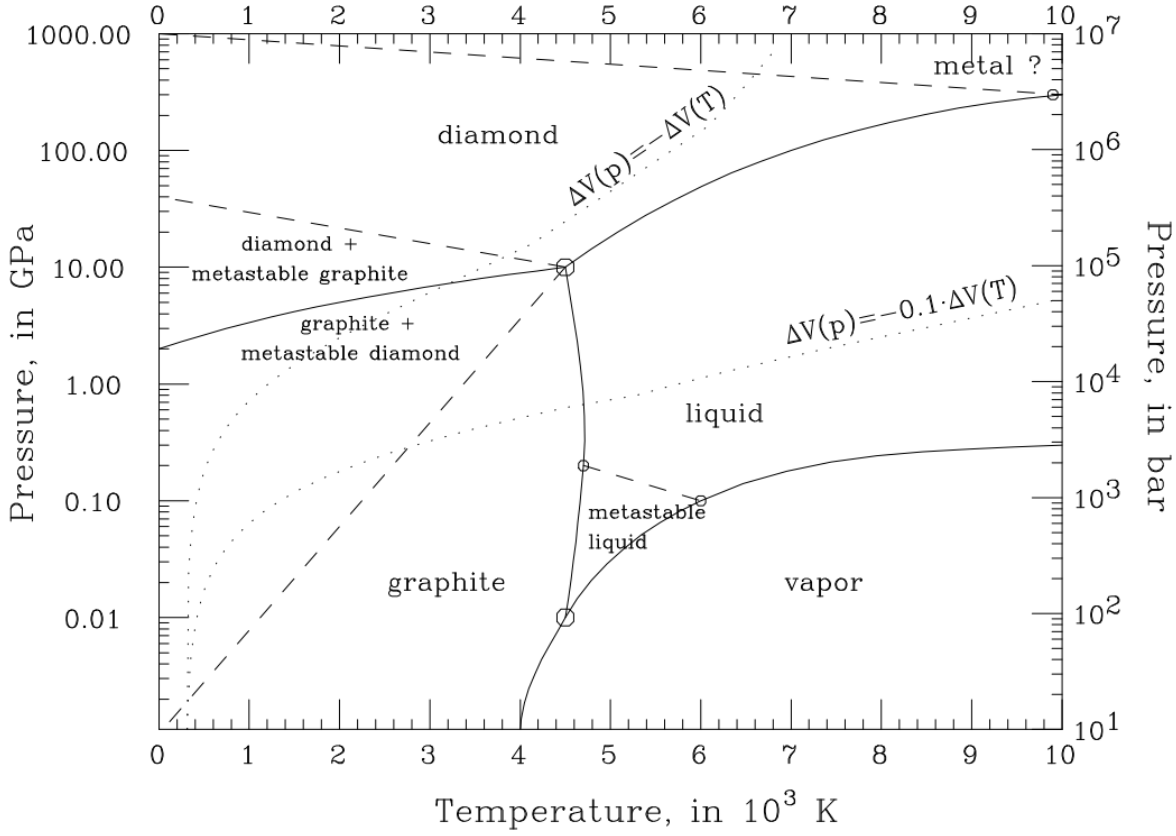

Figure 1.2: Phase diagram of carbon, showing the regions where diamond exists both as a stable and as a metastable form of carbon. In standard conditions (293 K, 0.1 MPa), carbon exists as either graphite or metastable diamond. Adapted from [6].

Carbon has several other allotropes with a range of structures, such as lonsdaleite [7] (hexagonal sp^3 carbon found in meteorites) and glass-like carbon [8] (glassy, ceramic sp^2 carbon with some graphitic properties), as well as amorphous carbon and diamond-like carbon [9] (mixtures of sp^2- and sp^3-hybridised carbon without any long-range order). Nanoscale allotropes of carbon have been shown to have diverse and impressive properties; most notably in recent years, graphene has drawn a lot of focus in the scientific community for being a flexible-yet-strong material with high electrical conductivity [10], with a wide range of dopants

further improving its electrocatalytic performance [11]. Carbon fullerenes, in particular nanotubes, have found use in a range of applications especially for their electrical conductivities [12].

Unlike the many highly conductive sp^2-hybridised forms of carbon, sp^3-hybridised diamond is highly insulating. However, using dopants (commonly boron, nitrogen, or phosphorus) can allow the electrical conductivity of diamond to approach metallic values [13]. Diamond has potential as a next-generation semiconductor (alongside SiC, GaAs and GaN), making use of diamond's wide band gap as it allows a higher device power before intrinsic breakdown compared to Si-based devices [14]. Diamond's superlative thermal conductivity is also of great interest, in particular for its utilisation as heat management for high-power devices, such as GaN-based transistors [15] – this is discussed in much greater detail in Chapter 4.

Being chemically and biologically inert, diamond is well-suited to applications in a range of biological areas, from brain-computer interfaces [16] to drug delivery [17] to antibacterial surfaces [18] – the last of which is explored further in Chapter 5.

1.2 Diamond growth techniques

1.2.1 Natural diamond vs. synthetic diamond

Diamond is a naturally occurring material, formed in the very high pressure (5 GPa) and high temperature (1200 °C) conditions of the Earth's upper mantle, approximately 160 km below the surface, with the largest natural diamonds having grown over the course of millions of years. Volcanic activity can push these diamonds up near enough to the surface to be mined [19]. However, naturally occurring diamond has many limitations to its use in industrial and scientific applications: its scarcity and value as a gemstone makes it expensive to use; the lack of control over its growth size means obtaining diamond of a useful size is challenging; and a range of naturally occurring impurities can alter the diamond's properties [20].

Natural diamond is qualitatively classified into four categories, based on the nature of the impurities present: types Ia, Ib, IIa and IIb [21]. Ia and Ib are indicative of nitrogen impurities, with Ia being by far the most commonly found type, and containing a higher level of nitrogen but usually in aggregates, while Ib have nitrogen singly substituted throughout the lattice [22]. Diamond with very low levels of impurities are classed as type IIa, while IIb contain substantial boron impurities, resulting in the diamond being a p-type semiconductor [2].

As such, the concept of synthetic diamond is very appealing, as a synthetic fabrication process could allow diamond to be produced in large amounts for a relatively lower cost, grown into useful sizes and shapes for the desired applications, and with the potential of finely-tuned incorporation of dopants when desired to modify its properties to suit a particular need. Since the 1950s, there have been various techniques developed to try to grow diamond.

1.2.2 High Pressure High Temperature diamond

Initial attempts to create synthetic diamond replicated and exceeded the high temperatures (1500-3000 °C) and very high pressures (5 GPa) where diamond forms in nature, utilising the high-pressure high-temperature (HPHT) technique [23,24]. In this technique, graphite is dissolved into a molten metal (which acts as a catalyst) at high temperature while compressed to high pressures by a hydraulic press and anvil system, which results in the diamond precipitating into individual grains of single-crystal diamond with sizes reaching up to several millimetres.

However, HPHT diamond often contains nitrogen or boron impurities turning the resultant material yellow-brown or blue respectively, which makes it undesirable for gemstones and many electronic applications. These impurities come from the solvent/catalyst combinations used for growth, with the two most common methods using Fe-Co (which readily dissolves nitrogen into it which then is incorporated into the diamond during growth) and Fe-Al-B (which incorporates boron from the catalyst itself) [21]. Additionally, with the lack of control over shape and size during growth, HPHT diamond is not suited for use as a coating or heat sink. As such, most HPHT diamond is used in mechanical industrial applications as coatings for cutting tools, and as grit powders for grinding and polishing. Overall, HPHT diamond is a useful material, but the diamond produced is limited in size and unable to fully benefit from many of diamond's properties [25].

1.2.3 Chemical Vapour Deposition diamond

With the limitations of HPHT diamond identified, another method was developed using a hydrocarbon gas as fuel, with much lower pressures (0.1-0.5 atm) and lower temperatures (700-1000 °C) which could slowly but continuously grow diamond to larger scales with more defined growth shapes [26]. These systems use either plasmas or hot filaments to fragment the hydrocarbon gas into radicals which deposit onto a substrate as diamond. Hydrogen gas is added to the process gas mixture because after fragmentation, the resulting H atoms etch away any graphitic or non-diamond material which is co-deposited during growth [27]. This basic method outlines a broad set of processes called chemical vapour deposition (CVD) [28]. CVD allows diamond growth to be fine-tuned, with control over purity, size and shape of the diamond grown, along with some control over various properties through the growth conditions used and the addition of dopants during growth, resulting in CVD being a more versatile technique than HPHT.

However, CVD diamond growth does have some limitations. Growth rates for the most common CVD processes are usually in the range of 10-30 µm/h, with rates of 60 µm/h only being attained with comparatively high pressures (500 Torr) [29], while growth rates up to 180 µm/h can be used to generate high-quality HPHT diamond [30]. CVD also requires growth onto a substrate, so there are additional decisions required as to the material to use: this is discussed in details in Section 1.2.5.

Activation of the feedstock gases can be achieved through a range of techniques [3], but only two techniques will be focussed on here. These techniques, namely hot filament and microwave plasma-assisted, are very commonly used due to their versatility and ease of use. They are both used in the Bristol University Diamond Group and are discussed in depth in Chapter 2.

1.2.4 Detonation nanodiamond

An effective method for producing nanodiamond is to mimic the natural growth conditions momentarily using explosives. By detonating carbon-rich explosives such as TNT-hexogene mixtures in a sealed container – ensuring that there is insufficient oxygen present for complete combustion of the explosive – the resultant soot can contain up to 80% diamond crystallites with approximately 5 nm diameter, with the explosive providing both a source of carbon and energy for the reaction. [31]

1.2.5 Substrates for CVD growth

As previously mentioned, CVD requires a substrate onto which the diamond is deposited; the choice for this material has many considerations.

Firstly, during growth the substrate is heated to a high temperature (700-1000 °C) [32], so requires a suitably high melting point. Additionally, given the lower-than-atmospheric pressures used during growth, the vapour pressure of the material can also be important, as even though it may not melt during growth, the substrate may give off vapour and contaminate the growth chamber. As such, the substrate material must be stable in the conditions required for CVD growth.

Substrates also require a similar coefficient of thermal expansion to diamond to avoid cracking or delamination of the diamond during cooling post growth. At the start of growth, the substrate is heated to the growth temperature by the plasma, resulting in expansion. The diamond then grows onto this expanded substrate, and when growth ends and the temperature reduces, both the diamond film and the substrate contract. During this contraction, a mismatch of thermal expansion coefficients results in compressive stresses in the diamond film and can cause bowing, cracking, flaking or even delamination of the grown film. [33]

Another consideration is adherence between the diamond and the substrate. If the substrate is able to form a carbide at the interface between the layers, then delamination is less likely, as a carbide layer enables some relief of the stresses caused by thermal expansion mismatching and bonds the layers together. If no carbide can be made (for example, Cu, Ag, Au or sapphire), then the diamond will delaminate on cooling; conversely, materials that very readily carbidise (such as Ni, Ti and Fe) can act as a 'carbon sink', absorbing the carbon into them as growth continues, forming a growing carbide layer. This carbide layer prohibits diamond growth until the substrate is saturated and significantly alters the physical properties of the substrate. [33]

As such, the choice of material for the substrate is complex. While the choice is dependent on the desired application, many materials are unsuitable for use from the criteria. Diamond itself presents the best material for the substrate, allowing for homoepitaxial growth and being compatible with the growth conditions. However, most applications of diamond benefit from heteroepitaxial growth, that is diamond grown onto another material: for this, one of the most common is single-crystal Si, as this is a low-cost material, highly available and suitable for the growth environment.

1.3 The chemistry of diamond growth

1.3.1 Mechanisms of growth

With CVD diamond, the process gases – here CH_4 and H_2 – flow into a chamber and diffuse towards the substrate. As they flow, they pass through the activation region (for example, a hot filament or a microwave plasma), fragmenting the gases to produce reactive free radicals (H, C_xH_y, where $x<3$ and $y<6$) and increasing the gas temperature to ~1500 °C. These radical fragments react with each other and reach a steady-state equilibrium situated just above the substrate surface. Some of the radicals strike the substrate surface where they may adsorb, migrate around, and desorb, or with the right conditions, attach to the growing diamond surface and propagate the diamond lattice.

The gas mixture usually consists of 1–5% CH_4 in H_2, depending on the reactor type and the properties of diamond desired, with lower CH_4 often yielding larger diamond grains at a slower growth rate.

Atomic hydrogen, H, is generated *in situ* from H_2 – either by thermal decomposition in hot filament systems or by electron impact in plasma systems. H atoms perform a few crucial roles in CVD growth by:

i. Terminating "dangling bonds" left on the deposition surface which could otherwise allow reconstruction of the sp^3 diamond surface to sp^2 graphite;
ii. Etching sp^2 graphitic carbon when it is deposited, removing graphite impurities during growth;
iii. Splitting longer chains of gas-phase hydrocarbons into smaller molecules, preventing polymer deposition;
iv. Creating reactive radicals (e.g. CH_3) from neutral species (CH_4) in the gas mixture to deposit onto the substrate.

Figure 1.3 shows how deposition occurs over the three steps: site activation by H, followed by CH_3 addition at the activated site, then the formation of the C-C bond resulting in overall growth of the diamond surface. As such, diamond deposition can be described as a step-wise addition of carbon atoms onto a diamond surface, catalysed by an excess of hydrogen [3]. There has been repeated debate over the exact mechanism, in particular, the specific conditions desired for the activated site [34] and the most important carbon-containing radical [35] These specifics are also dependent on the gas-phase chemistry, the means of activation – dependent on the reactor type – and the orientation of the diamond lattice. However, the specifics of the mechanism are not important to this work beyond the relevance of the gas chemistry and the reactor type, so are not further explored.

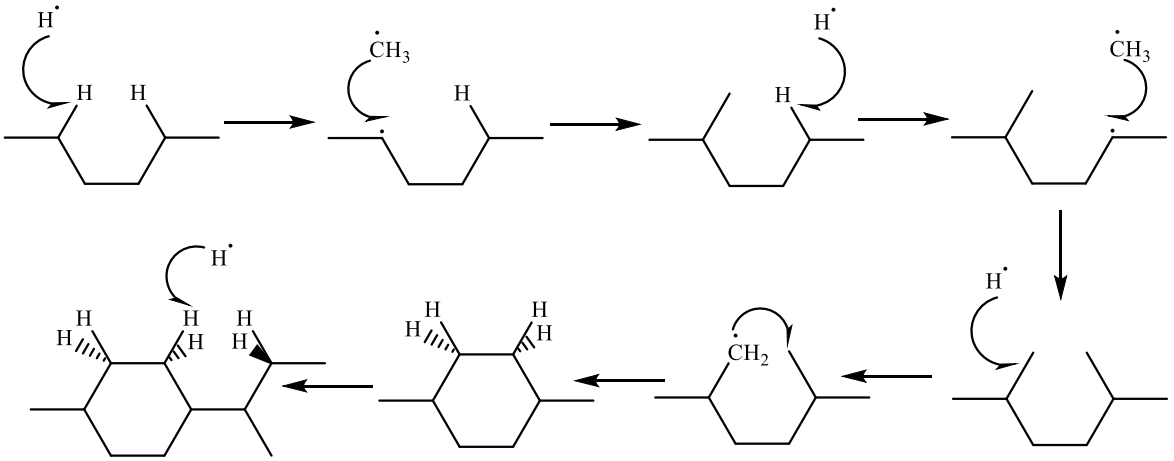

Figure 1.3: The mechanism of the reaction of H and CH_3 radicals with a diamond surface, resulting in diamond growth. Reproduced from [36].

1.3.2 Addition of dopants

Gases other than hydrogen and the carbon source may be added to the CVD gas mixture, which affect both the growth rate and the morphology of the grown diamond. Some gases only alter growth without becoming incorporated into the diamond, while others impact both the growth chemistry and the resultant diamond properties. Further information on both how doping is performed and the effect on the grown diamond can be found in [37] for boron doping and [38] for nitrogen doping. As doping is not explored in this project, no further detail is discussed.

1.3.3 α-parameter

Crystal lattices are commonly described using an *x,y,z* coordinate system for the faces of the crystal, with diamond's main surfaces for growth being the square (100) surface and the triangular (111) surface [33]. Other less conventional crystalline faces such as (110) and (113) can be observed when growing thicker films [39]. Temperature and gas composition both determine the growth rates for these surfaces independently due to kinetics, which can in turn allow for some control over the morphology of the diamond grown. The most used term is that of α-parameter, which provides a measure of the growth rate of the (111) surface relative to the (100), shown in equation 1.1.

$$\alpha = \sqrt{3}\left(\frac{v_{100}}{v_{111}}\right) \tag{1.1}$$

where v_{100} and v_{100} are the growth rates for the <100> and <111> directions respectively.

Similarly, the β and γ parameters are the rates of (110) and (113) relative to (100) respectively [40].

The significance of the α-parameter on the morphology of the resultant diamond is dependent on the nature of the diamond grown. When growing single-crystal diamond, α-parameter determines if the diamond is cubic (α=1), octahedral (α=3) or cubo-octahedral ($1 < \alpha < 3$); for polycrystalline films, a lower α yields a predominantly (100) surface with square facets, while a higher α produces triangular (111) facets, and between those a mixture of the two. [40]

1.3.4 Influence of seeding on growth and crystal morphology

Some substrate materials will nucleate diamond on their surface without some form of surface pre-treatment [41], with diamond being the obvious example – diamond can quite easily be used as a substrate for further diamond growth, with the surface morphology dictating how the growth occurs initially [42]. Cubic boron nitride also readily allows for nucleation [43], and stable carbide-forming materials – such as Si, W and Mo – generally nucleate one to two orders of magnitude faster than non-carbide-forming materials (Cu, Au) [44].

For increased nucleation to occur on other materials, there are several approaches, the main two being scratching and adding diamond seeding for the diamond to grow from. Diamond seeding acts exactly as one might expect – providing diamond material for growth to occur on directly [45]. This seeding may be done using diamond of different sizes, from nanodiamond on the order of nanometres in diameter up to microdiamond four orders of magnitude larger.

Scratching is thought to aid growth in many ways, from minimising the interfacial energy on sharp convex surfaces, adding dangling bonds and breaking surface bonds, relief of strain fields, the ability for carbon to saturate a sharp edge more easily, and removal of surface oxides enabling easier bonding [46]. All these effects are known to contribute to an increase in nucleation rate, with the impact of each depending on the material and the extent of scratching. To carry out this surface roughening procedure, different approaches are used, with sonication of the substrate in a nanodiamond solution being one of the most common, and another being manual abrasion using diamond grit. The diamond abrades the surface, making sharp edges for nucleation. [41]

Crystal morphology is driven by two main mechanics: the starting morphology of the diamond and the growth conditions. Single-crystal diamond – that is, a piece of diamond that consists of only one single grain, and therefore has no grain boundaries – can usually only be obtained when growing from a single-crystal diamond initially; there are methods to produce single-crystal using iridium substrates [47] but this technique is not widely used due to its complexity. Polycrystalline diamond – diamond material consisting of a number of grains joining at grain boundaries of sp^2 carbon – is much more widely used, as films of polycrystalline diamond can be grown on a wide range of substrates. These films are usually identified by the size of the largest grains, ranging from ultrananocrystalline (2-5 nm), to nanocrystalline (10s-100s of nm), to microcrystalline (1s-100s of μm), with differing properties being accessible with each scale. The size of the nucleation crystals have some impact on the resultant films [48].

However, for example, using growth conditions that are best suited for microcrystalline diamond will result in microcrystalline diamond, even if a nanodiamond seeded substrate or a single-crystal diamond substrate is used initially. As such, the growth conditions usually dictate the morphology of the diamond film produced. The growth conditions are dependent on the reactor and technique used, but often a lower methane percentage results in a larger grain, and the addition of other gases to the CVD feedstock reduces grain sizes. [49]

1.4 Thesis outline

The central focus of this thesis is exploring diamond growth on a range of substrates that are not commonly used for diamond growth. Most diamond growth is performed on polished, flat substrates of silicon, tungsten, molybdenum, or diamond, limiting the applications of the resultant material. As such, the primary aim is to grow diamond onto unusual substrates to allow diamond's excellent properties to be utilised in applications where previously they could not. As a secondary aim, a large-area reactor was developed to allow for diamond films to be grown on "industrially-relevant" scales.

Subsequently, this thesis is separated into seven chapters, with each experimental chapter focussing on a specific substrate area to be explored. Chapter 1 provides a brief overview of the core details of CVD diamond growth, and Chapter 2 proceeds to cover the specifics of the techniques used for this thesis, detailing the apparatus and methods used for synthesis and characterisation of the diamond produced experimentally. Chapter 3 focusses on the use of a textured silicon substrate called "black silicon", then CVD growth to coat the black silicon with a thin film of diamond to yield "black diamond" and exploration of its use as an antibacterial surface. Chapter 4 explores growing diamond films onto semiconductors, especially GaN, for use as a heat sink, requiring a specialised seeding technique to ensure a low thermal resistance between the layers. Chapter 5 investigates the novel use of self-assembled polymer micelles as a pattern to grow structured diamond shapes with nanoscale resolution. Chapter 6 provides a concise summary of Chapters 3, 4 and 5 and presents future work which should be done to expand on this thesis.

Additionally, appendix A details the design, construction, and optimisation of a large-area CVD reactor, allowing growth over much larger areas than existing reactors while still retaining the ability to tune growth conditions for the desired substrates.

References

1 Ward, F. *Diamonds*. Gem, Bethesda, MD, 1998.

2 Field, J. E. *The Properties of Natural and Synthetic Diamond*. Academic Press, London, 1992.

3 May, P. W. Diamond thin films: a 21st-century material. *Phil. Trans. R. Soc. Lond. A*, 358 (2000), 473-495.

4 Bundy, F. P. *J. Geophys. Res.*, 85 (1980), 6930.

5 Butenko, Y. V., Kuznetsov, V. L., Chuvilin, A. L., Kolomiichuk, V. N., Stankus, S. V., Khairulin, R. A., and Segall, B. *J. Appl. Phys.*, 88 (2000), 4380.

6 Steinbeck, J., Braunstein, G., Dresselhaus, M. S., Venkatesan, T., and Jacobson, D. C. *J. Appl. Phys.*, 58 (1985), 4374.

7 Frondel, C. and Marvin, U. B. *Nature*, 214 (1967), 587-589.

8 Harris, P. J. F. *Philos. Mag.*, 84 (2004), 3159-3167.

9 Heimann, R. B., Evsyukov, S. E., and Koga, Y. *Carbon*, 35 (1997), 1654-1658.

10 Geim, A. K. and Novoselov, K. S. *Nature Mater.*, 6 (2007), 183-191.

11 Wang, L., Sofer, Z., and Pumera, M. *ACS Nano*, 14 (2020), 21-25.

12 Popov, V. N. *Mater. Sci. Eng., R*, 43 (2004), 61-102.

13 May, P. W., Ludlow, W. J., Hannaway, M., Heard, P. J., Smith, J. A., and Rosser, K. N. *Diamond Relat. Mater.*, 17 (2008), 105-117.

14 Balmer, R. S., Brandon, J. R., Clewes, S. L. et al. *J. Phys. Condens. Matter*, 21 (2009), 364221.

15 Wang, A., Tadjer, M. J., and Calle, F. *Semicond. Sci. Technol.*, 28 (2013), 055010.

16 Nistor, P. A., May, P. W., Tamagnini, F., Randall, A. D., and Caldwell, M. A. *Biomaterials*, 61 (2015), 139-149.

17 Man, H. B. and Ho, D. *Phys. Status Solidi*, 209 (2012), 1609-1618.

18 May, P. W., Clegg, M., Silva, T. A. et al. *J. Mater. Chem. B*, 4 (2016), 5737-5746.

19 Harlow, G. E., ed. *The Nature of Diamond*. Cambridge University Press, Cambridge, UK, 1998.

20 Robertson, R., Fox, J. J., and Martin, A. E. *Phil. Trans. R. Soc. A*, 232 (1934), 463-535.

21 Burns, R. C., Hansen, J. O., Spits, R. A., Sibanda, M., Welbourn, C. M., and Welch, D. L. *Diamond Relat. Mater.*, 8 (1999), 1433.

22 Walker, J. *Rep. Prog. Phys.*, 42 (1979), 1605.

23 Hall, H. T. Ultrahigh-Pressure Research. *Science*, 128 (1958), 445-449.

24 Barnard, A. S. *The Diamond Formula - Diamond synthesis: a gemmological perspective*. Butterworth Heinemann, Oxford, 2000.

25 Davies, G. *Diamond*. Adam Hilger, Bristol, 1984.

26 Eversole, W. G. *US Patent nos 3030187, 3030188*. 1958.

27 Angus, J. C., Will, H. C., and Stanko, W. S. *J. Appl. Phys.*, 39 (1968), 2915.

28 Matsumoto, S., Sato, Y., Tsutsumi, M., and Setaka, N. *J. Mater. Sci.*, 17 (1982), 3106.

29 Bolshakov, A. P., Ralchenko, V. G., Shu, G. et al. *Mater. Today Commun.*, 25 (2020), 101635.

30 Babich, Y. V., Feigelson, B. N., and Yelisseyev, A. P. *Diamond Relat. Mater.*, 13 (2004), 1802-1806.

31 Krueger, A. *Chem. - A Eur. J.*, 14 (2008), 1382.

32 Ahmed, W., Rego, C. A., Cherry, R., Afzal, A., Ali, N., and Hassan, I. U. *Vacuum*, 56 (2000), 153.

33 May, P. W. *Carbon Based Nanomaterials*. Trans Tech, 2010.

34 May, P. W. and Mankelevich, Y. *J. Phys. Chem. C*, 112 (2008), 12432.

35 McCauley, T. G., Gruen, D. M., and Krauss, A. R. *Appl. Phys. Lett.*, 73 (1998), 1646.

36 Ashfold, M. N. R., May, P. W., Rego, C. A., and Everitt, N. M. *Chem. Soc. Rev.*, 23 (1994), 21.

37 Fujimori, N., Nakahata, H., and Imai, T. *Jpn. J. Appl. Phys.*, 29 (1990), 824.

38 Charles, S. J., Butler, J. E., Feygelson, B. N. et al. *Phys. Status Solidi A*, 2485 (2004), 2473.

39 Silva, F., Bonnin, X., Achard, J., Brinza, O., Michau, A., and Gicquel, A. *J. Cryst. Growth*, 310 (2008), 187.

40 Brinza, O., Achard, J., Silva, F., Bonnin, X., Barroy, P., De Corte, K., and Gicquel, A. *Phys. Status Solidi A*, 205 (2008), 2114.

41 Liu, H. and Dandy, D. S. *Diamond Relat. Mater.*, 4 (1995), 1173.

42 Ren, Z.- Y., Liu, J., Su, K., Zhang, J.- F., Zhang, J.- C., Xu, S.- R., and Hao, Y. *Chinese Phys. B*, 28 (2019), 129103.

43 Koizumi, S., Murakami, T., Inuzuka, T., and Suzuki, K. *Appl. Phys. Lett.*, 57 (1990), 563.

44 Spitzyn, B. V., Bouilov, L. L., and Derjaguin, B. V. *J. Cryst. Growth*, 52 (1981), 219.

45 Thomas, E. L. H., Mandal, S., Ahmed, A.-I.- et al. *ACS Omega*, 2 (2017), 6715.

46 Lux, B. and Haubner, R. *Diamond and Diamond-like Films and Coatings*. Plenum Press, New York, 1991.

47 Fischer, M., Brescia, R., Gsell, S. et al. *J. Appl. Phys.*, 104 (2008), 123531.

48 May, P. W. and Mankelevich, Y. A. *J. Phys. Chem. C*, 112 (2008), 12432.

49 Richley, J. C., Fox, O. J. L., Ashfold, M. N. R., and Mankelevich, Y. A. *J. Appl. Phys.*, 109 (2011), 063307.

Chapter 2 – Experimental methods

2.1 Hot filament CVD

Hot filament (HF) CVD utilises filaments – usually made of refractory metals – resistively heated by a direct current to produce a high temperature (>1500 °C) to activate the gas mixture, with deposition occurring on substrates mounted nearby [1].

University of Bristol Diamond Group has two home-built HF CVD reactors used for growing diamond thin films: one "undoped" and one "doped". B_2H_6 leaves residual contamination after use, so the "doped" reactor always results in at least a low level of boron-doping during growth even without a flow of B_2H_6, while the "undoped" chamber has no boron contamination and can also be used for nitrogen doping. Figure 2.1 shows a schematic design of the reactor and photographs of the actual reactor.

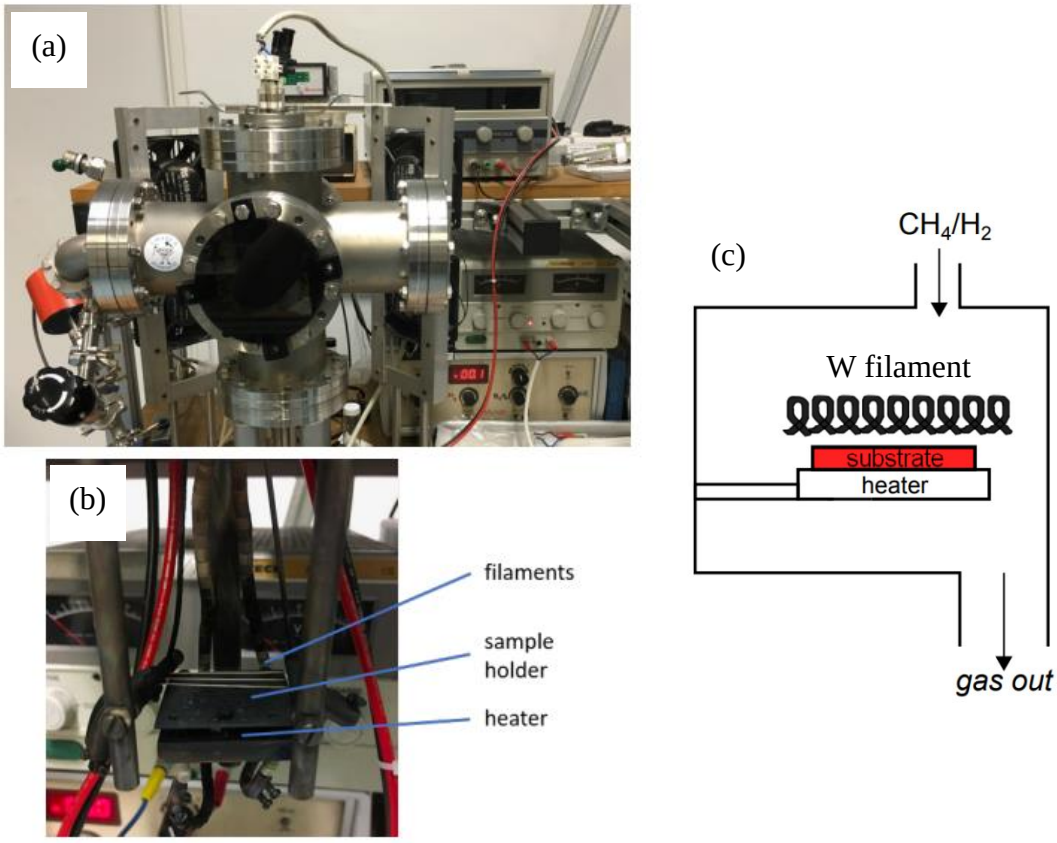

Figure 2.1: (a) Photograph of the undoped hot filament (HF) CVD reactor. (b) Photograph of the sample stage and filament setup of the reactor. Adapted from [2]. (c) Schematic of HF CVD reactor. Adapted from [3].

Before growth, 0.25 mm-diameter tantalum filaments were fitted using springs to tension them, so they remained taut even with the thermal expansion from heating when the reactor was running. Tantalum was used as it is relatively unreactive to the feedstock gases and can maintain these temperatures with only a small amount of thermal expansion. 3 filaments were used, each approximately 70 mm long, and with 25 A applied at 8-12 V applied in parallel, growth was carried out at approximately 250 W.

Once the filaments were in place, the substrates for growth were placed on the substrate holder, with a total area of 25 × 15 mm available for uniform growth. This limited growth area was one of the primary motivations of the development of a large-area reactor presented in Appendix A. Substrates could be of any material that would be able to survive the growth environment and any shape so long as they fit within the growth area, making HF CVD well suited to a wide range of applications. The substrate surface was usually maintained at 4 mm beneath the filaments for optimal growth conditions, and the reactor design allowed the substrate holder to be repositioned to accommodate a range of sample thicknesses. Before placing them into the reactor, substrates were usually coated with a dispersal of nanodiamond to act as seed crystals which enabled much better nucleation density. The techniques used in seeding are discussed in Section 2.4.

The filament-substrate holder assembly was loaded into the chamber which was then pumped down for at least 60 minutes, reaching a base pressure of ~80 or ~10 mTorr for the undoped and doped chambers respectively, both using a 2-stage rotary pump. During this time and during growth, the substrate holder was heated to ~300 °C by a built-in resistive wire to degas adsorbates. Degassing these oxygen-containing adsorbates prevented the filaments oxidising and breaking within the first 5 minutes of growth [4]. During diamond deposition, the Ta wires slowly carburised from the methane, making them brittle and prone to snapping rather than being able to expand and contract in response to temperature changes. This carburisation caused a changing resistance of the filaments, and subsequently varied the voltage and power applied by the power supply, which only provided a fixed current.

Growth in these reactors was usually performed at 20 Torr, using gas flows of 200 and 2.00 standard cubic centimetres per minute (sccm) of H_2 and CH_4 respectively, with 3.5 sccm of 5% B_2H_6 in H_2 added for boron-doped growth. This equated to 1% CH_4 in H_2, with 850 ppm B_2H_6 when added. These flow rates were measured and controlled by individual mass flow controllers (MFCs) for each gas. The gases flowed in through the side of the chamber, allowing

good mixing both in the pipes and in the chamber, before being pumped out of the bottom of the chamber, which ensured they flowed past the substrates after activation.

Overall, these standard parameters yielded good quality diamond thin films on a range of samples, with growth rates of ~0.5 µm h^{-1}. Due to the differing applications of the samples produced, conditions were varied and are detailed more thoroughly in their relevant sections, with films ranging in thickness from 10s of nm to 10s of µm.

2.2 Microwave plasma-assisted CVD

Microwave (MW) plasma-assisted CVD uses the coupling of microwave energy through a dielectric quartz window into gas-phase electrons, which then collide with and heat the gas. This results in dissociation of the molecules to form a plasma containing the reactive species desired for the CVD process [1].

For this project, a 2.45 GHz ASTeX-type reactor was used, shown in Figure 2.2. Samples were placed on a Mo or W disk, which itself sat on a Mo or W spacer wire, wound into a circle, and placed onto the water-cooled baseplate. This spacer reduced the effectiveness of the water-cooling for the disk and sample, allowing for the surface of the substrate to reach optimal growth temperatures without requiring the chamber itself to get hot. The spacer achieved this by reducing the conduction of heat from the disk (heated by the plasma) to the water-cooled baseplate. By varying the thickness of the spacer, the substrate temperature could be modified, ranging from ~600 °C without a spacer up to >1000 °C using 0.25 mm diameter wire or thicker while at standard growth plasma conditions. Similarly, increasing the thickness of the disk increased the substrate temperature. Varying spacer and disk thickness was the preferred method for changing the substrate temperature, as they allowed the plasma conditions to be unaffected, reducing the number of parameters changed.

The baseplate was then loaded into the chamber and pumped to a base pressure of <20 mTorr using a 2-stage rotary pump before any gases were added. Hydrogen gas was then added and the pressure set to 15 Torr. The MW power supply was turned on, striking a plasma at a power of 700 W, resulting in a large spherical purple plasma. In the event that a plasma did not strike, the waveguide was tuned until the plasma struck, with the tuning altering the phase of the standing wave until an anti-node was well-placed to provide the gas-phase electrons with sufficient energy to sustain the plasma discharge directly above the substrate.

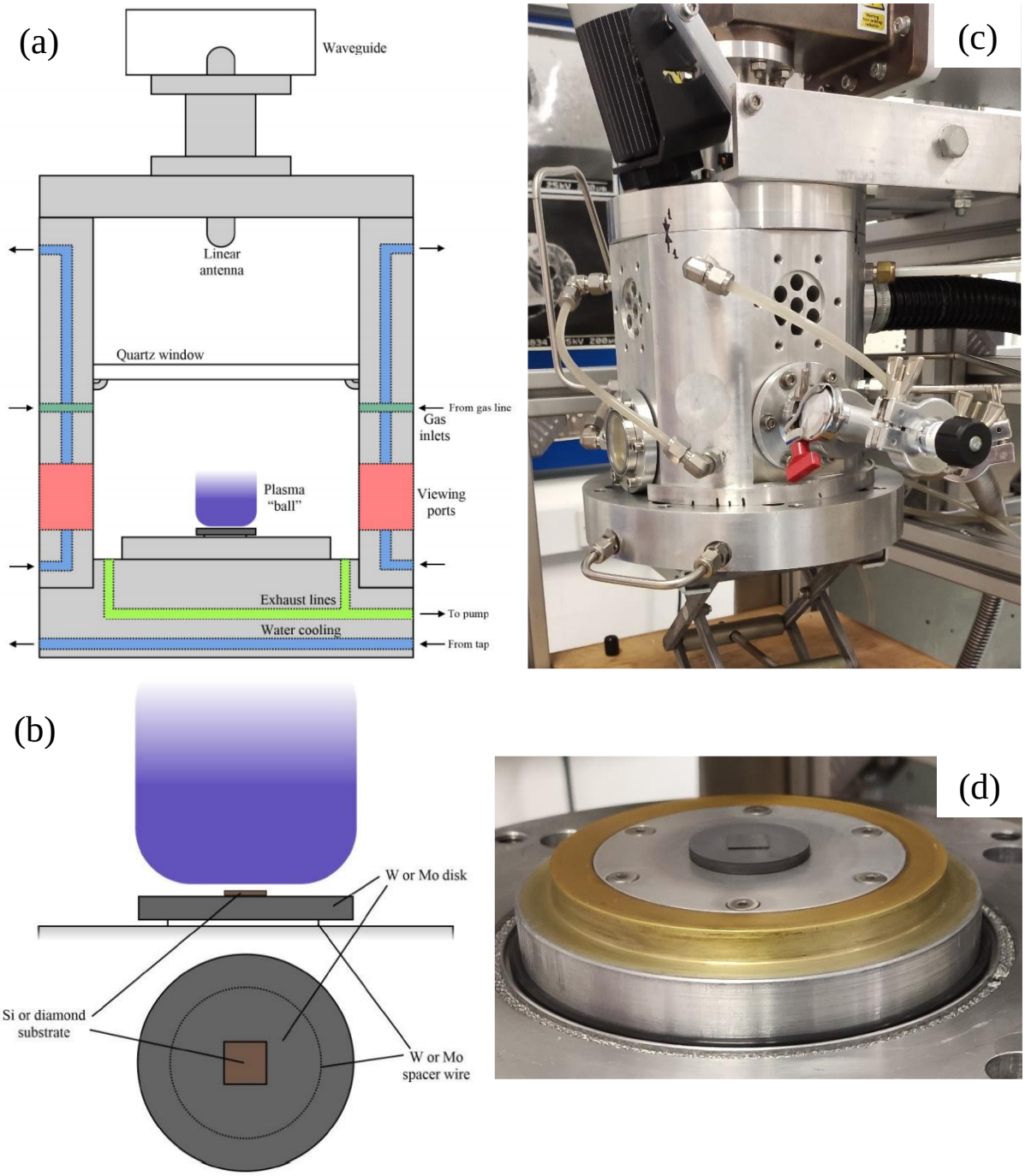

Figure 2.2: (a) Schematic diagram of the microwave (MW) CVD reactor, and (b) enlarged schematic diagram of the wire-disk-substrate assembly. Microwaves generated by the magnetron enter *via* the waveguide, transmitted by the antenna, and produce a plasma centred on an anti-node of the standing wave. Substrate temperature is increased by direct radiation from the plasma and reduced by cooling from the baseplate, with the wire and disk thicknesses determining the extent of cooling. The gas mixture is flowed in through the inlets and exhausted through the outer edge of the baseplate, with the exhaust rate controlled by an automated butterfly valve to maintain the desired pressure inside the chamber. (c) and (d) Photographs of the MW CVD reactor used experimentally. Schematics from [5].

The reactor conditions were then adjusted to those required for growth, with pressure being increased first to reduce etching of the sample from electron and ion bombardment. As pressure was increased, the plasma shrank, until more power was added and then would stabilise as a small ball located directly above the substrate. CH_4 was added as pressure reached ~50 Torr, because it was found to be easier to keep the plasma stable by adding it while the conditions were transitioning from the strike conditions to the growth conditions. The CH_4 addition was quickly noticeable as the characteristic green C_2 emission band started at the top of the plasma and crept down until the entire plasma was uniformly pale green. Standard growth pressures and powers were 100-150 Torr and 1000-1500 W, respectively (1500 W being the maximum for the MW power supply), with a gas flow of 300 sccm H_2 and 12.5 sccm CH_4 equating to a mixture of 4% CH_4 in H_2. Using 120 Torr and 1500 W with a spacer of 0.20 mm diameter produced a substrate temperature of ~900 °C and a diamond growth rate of ~5 μm h^{-1}.

Substrate temperature was measured using a 2.2 μm-wavelength one-colour pyrometer which monitored the substrate *via* a viewport in the top of the chamber. The pyrometer provided an estimate of the temperature using a comparison of the material's emitted radiation of 2.2 μm to that of a perfect black-body in the same conditions, the ratio of which is called the emissivity [6]. As diamond films were grown in the reactor, the emissivity of the substrate surfaces changed, both from changes in surface roughness and the composition of the surface material itself (e.g. Mo to diamond), meaning that all temperatures "measured" had significant uncertainty, especially for thicker films. Most materials do not have a constant emissivity with changing temperature, so for all growth presented herein, an empirical emissivity for each material was determined in a hydrogen plasma at 100 Torr and 1000 W using a 0.10 mm diameter spacer *via* comparison to a two-colour pyrometer – these values are presented in Table 2.1. These values were obtained in a pure hydrogen plasma because one of the measured wavelengths of the two-colour pyrometer coincides with one of the prominent emissions from CH_4-containing plasmas, thus affecting the two-colour reading and making one-colour pyrometry preferred.

Table 2.1: Emissivity values used for determining surface temperature by one-colour pyrometry for the various materials used. These values were determined by comparing the reading on the one-colour pyrometer compared to a two-colour pyrometer in a 1000 W, 100 Torr H_2 plasma.

Material	Emissivity
Single-crystal diamond	0.13
Polycrystalline diamond	0.19
Silicon (polished)	0.19
GaN	0.17
AlN	0.25
Tungsten	0.17
Molybdenum	0.17

Substrate material, size and shape is more significant in MW CVD than in HF CVD, as the substrate effectively acts as the antenna on the node at the bottom of the reactor chamber, with the plasma centred on an anti-node of the standing wave. As such, the plasma itself is altered as the diamond grows – this is not significant during shorter growths but can become noticeable when doing growth on the order of 100s of μm thick.

As the substrate acts as an effective antenna, changing the shape and size of the substrate (or having multiple substrates) also alters the power density relative to the substrate, making heating of the sample(s) from the plasma vary with changing sample size. In order to minimize this effect, samples used throughout this project are 10 × 10 mm squares where possible.

2.3 Experimental growth conditions

Tables 2.2 and 2.3 present the experimental growth conditions standardly used throughout the work done in this thesis for the hot filament and microwave CVD reactors respectively. These conditions were varied to suit the specific experimental requirements, and the variations used are specified in the relevant chapters.

Table 2.2: Standard growth conditions used for hot filament (HF) CVD reactor growth of diamond films.

Undoped and doped HF CVD parameters	
Filament power (W)	250
Filament material	0.25 mm diameter W wire
Filament length (mm)	70 (each)
Heater power (W)	16
Gas pressure (Torr)	20
H_2 flow (sccm)	200
CH_4 flow (sccm)	2.00
CH_4:H_2 ratio	1:100
Growth area (mm^2)	25×15
Growth rate (µm h^{-1})	0.5
For B-doped growth only	
B_2H_6 (5% in H_2) flow (sccm)	3.5
B_2H_6 concentration (ppm)	850

Table 2.3: Standard growth conditions used for microwave plasma-assisted (MW) CVD reactor growth of diamond films.

MW CVD parameters	
MW input power (W)	1000-1500
Microwave frequency (GHz)	2.45
Gas pressure (Torr)	100-150
H_2 flow (sccm)	300
CH_4 flow (sccm)	12.5
CH_4:H_2 ratio	1:24
Growth area (mm^2)	10×10
Spacer wire thickness (mm)	0.10-0.30
Substrate temperature (°C)	700-1000
Growth rate (µm h^{-1})	2-5

2.4 Substrate material and seeding techniques

2.4.1 Silicon

As mentioned in Section 1.2.5, the choice of substrate material is important for diamond growth. While tungsten, molybdenum, and diamond itself are commonly used substrates, all the work within this project uses silicon as the main substrate material for a number of reasons. Silicon is cheap and easy to work with, allowing suitable sizes and shapes of samples to be produced with ease. Si also has a similar thermal expansion coefficient to diamond (Si = 2.6×10^6 K^{-1}, diamond = 1.0×10^6 K^{-1}) which causes low internal stresses in the diamond film upon cooling so that delamination rarely occurs. Hence, polished Si wafers were used to test and optimise the growth carried out in Chapter 6. The surface of Si can be modified easily, for example by using reactive-ion etching (RIE), the sample can be etched to leave needles of silicon on the order of 10 nm in diameter – a material termed "black silicon" (bSi). Diamond growth onto bSi and changing the chemical terminations of both Si and diamond surfaces is the focus of Chapter 3 of this thesis.

Si is well suited to being a handle-wafer for many applications. Chapter 4 explores the use of self-assembled polymer micelles as a diamond templating material, with these micelles being deposited onto Si squares prior to growth. This proved to be a suitable method to allow nano-scale structures to be placed into CVD diamond growth conditions and removed to be characterised by various microscopy methods. Similarly, Chapter 5 used Si as a handle wafer for gallium nitride and aluminium nitride layers to be grown on, which helped to reduce the thermal expansion mismatch between diamond and the GaN/AlN films.

2.4.2 Seeding using manual abrasion

To assist in diamond nucleation on the Si, nucleation sites need to be added to the otherwise polished smooth surface of the silicon wafers. Manual abrasion is a simple and effective technique to achieve this. For manual abrasion, two samples were cleaned with methanol and dried, then a small quantity of microdiamond crystals (~1-3 µm diameter, supplied by van Moppes) were placed on one sample, and the other sample placed on top so that the polished surfaces faced each other with the microdiamond between. The samples were then ground into each other for 1-2 minutes until both surfaces appeared to have been abraded uniformly, then both were rinsed in methanol again and dried before use.

Manual abrasion increases nucleation sites in two ways: by scratching the surface of the polished samples and from the implantation of nanodiamond fragments into the surface – combining the two main method of improving nucleation density as outlined in 1.3.4. Scratching the surface provides many facets to encourage CVD diamond growth to occur. Some implanted diamond remains following growth, as is evidenced by occasional much larger diamond crystals in the films grown using this seeding technique. However, given the requirement of the surface of the samples to be abraded for this technique, it is not a suitable method for seeding any samples with more delicate surfaces. As such, this technique is only used for seeding samples to be used as flat control samples for comparison to bSi samples in Chapter 3.

An alternative method for abrading the substrates is by placing them in a solution containing nanodiamond and sonicating; however, this method was deemed unsuitable for the experiments, as the sonication would destroy the delicate bSi needles and was unable to produce the mixed-seeding required for the diamond-on-GaN.

2.4.3 Electrospray seeding

When manual abrasion was not a suitable technique to use, for example when using delicate samples such as bSi, an alternative method of seeding using an electrostatic spray ("electrospray") technique was utilised [7]. For this technique, a suspension of diamond particles (usually detonation nanodiamond, ~3 nm diameter, supplied by Amando) in methanol was prepared, using an ultrasonic probe to break up nanodiamond aggregates for 30 minutes immediately prior to seeding. 10 drops of nanodiamond solution (1 wt% in water) were added to 30 mL of methanol for use as the suspension. For Chapter 4, where a mixture of micro- and nanodiamond seeding was desired to minimise thermal barriers, a range of seeding solutions were used – the details of these mixtures are discussed further there.

The electrospray apparatus was located inside an electrically insulated polycarbonate box. The samples to be seeded were loaded onto a grounded rotating plate using conductive carbon pads, and the plate rotated at ~3 revolutions per second using a battery powered motor. 3 mL of the seeding solution was then placed into an injection syringe which passed through the side of the insulating box. A 35 kV potential difference is applied to the nozzle of the syringe using a power supply built in-house, causing the suspension to be sprayed towards the grounded samples, with the methanol evaporating on the way. As a result, the nanodiamond was

deposited uniformly across the samples. 3 mL of standard seeding solution usually provided a near-monolayer of nanodiamond, with the density of seeding adjusted by changing the concentration or volume of seeding solution used. A schematic diagram of the apparatus used for electrospray seeding is shown in Figure 2.3.

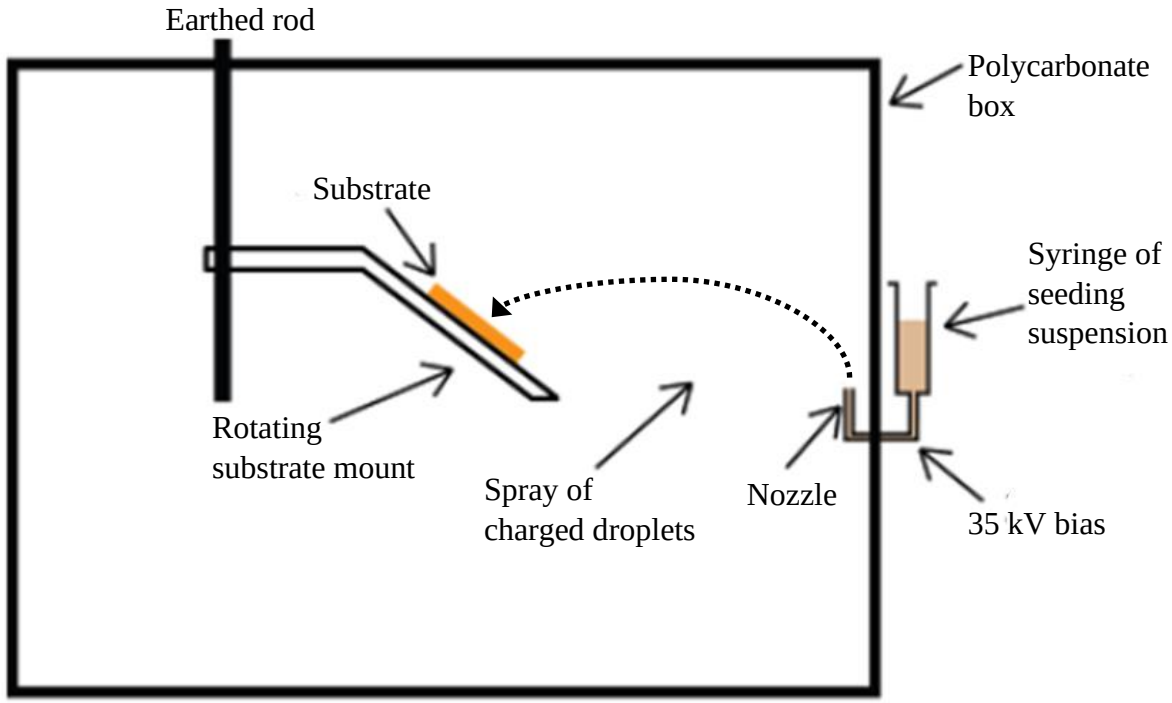

Figure 2.3: Schematic diagram showing the electrospray apparatus used to seed samples. A nanodiamond suspension is placed in the injection syringe, then ionised by an electrostatic potential difference, causing the nanodiamond to coat the substrate uniformly, with the solvent evaporating before reaching the substrate. Adapted from [7].

2.4.4 Submersion seeding

Electrospray seeding was effective at coating most substrates regardless of the 3D surface texture of the substrate, providing a good coating of nanodiamond even over many bSi samples. However, for some of the bSi, electrospray was unable to coat the full length of the needles, so an alternative method was developed. The same standard seeding solution as used for electrospray (see 2.4.3), following 1 hour of sonication, was used to submerge the bSi samples for 1 hour. In this time the nanodiamond particles in suspension diffused to the exposed surface and stuck to it *via* a combination of electrostatic and van der Waals forces. The samples were then removed from the suspension and gently dried with compressed air. This method produced a near-monolayer of nanodiamond seeds coating the entire surface of all bSi samples used, regardless of the length or density of the needles.

2.5 Surface termination of samples

2.5.1 Hydrogen termination

Standard procedures used in both HF and MW CVD diamond growth usually result in diamond films being hydrogen-terminated. However, for some experimental work, samples needed to be re-terminated with hydrogen after they had been exposed to ambient air for a long period or the surface had been terminated with another element (O, F, NH_2) for other experiments. For this, hydrogen termination was carried out in the MW CVD reactor using a sequence of conditions. The sample was loaded on a disk on a 9 mil (0.23 mm) Mo wire, and the chamber pumped to <20 mTorr. H_2 gas was flowed into the chamber at 300 sccm. The first step used a plasma at 80 Torr and 1100 W, achieving a substrate temperature of ~850 °C, to desorb the existing termination on the diamond surface. The pressure and power were then reduced to 40 Torr and 750 W respectively, giving a temperature of ~500 °C, allowing H to bond to the diamond surface. Finally, the power was reduced to 0 W, allowing the substrate to cool to room temperature in a hydrogen atmosphere. Each step was performed for 2 minutes to allow conditions to fully stabilise.

2.5.2 Oxygen, fluorine, and ammonia terminations

A modified version of an Edwards S150A sputter coater was used to terminate diamond surfaces with O, F, and NH_2. The design has been altered to generate a uniform 2.1 kV DC plasma between the electrodes at a pressure of ~1 Torr over an area of ~80 cm^2, allowing many samples to be terminated simultaneously [8]. For all three terminations, the optimal duration was determined using water contact angle (see 2.6.3) to ensure full termination with minimal plasma exposure to reduce surface etching. Conditions and durations for these terminations are shown in Table 2.4.

Table 2.4: Conditions used for termination of diamond surfaces.

Gas	Pressure / Torr	Duration / s
O_2	1.0	8
SF_6	0.5-1.0	10
NH_3	1.5	60

2.6 Characterisation techniques

2.6.1 Scanning electron microscopy

Scanning electron microscopy (SEM) – schematic shown in Figure 2.4 – is one of the core techniques used in characterisation of CVD diamond, because SEM is able to render images below the resolution limit of light (~200 nm). A filament is heated in high vacuum causing electrons to be emitted, which are focussed into a beam with electromagnetic lenses to create an "electron gun". These electrons hit the sample and are scattered while also causing secondary electrons to be ejected. All these electrons are collected and, by rastering the electron beam from point to point over the sample, the intensities of the secondary electrons can be captured and displayed as a 2D image of the sample surface with a resolution of ~50 nm. Thick undoped diamond samples are insulating and hard to image, and usually are sputter-coated in a thin (2-3 Å) layer of gold or silver to reduce charging.

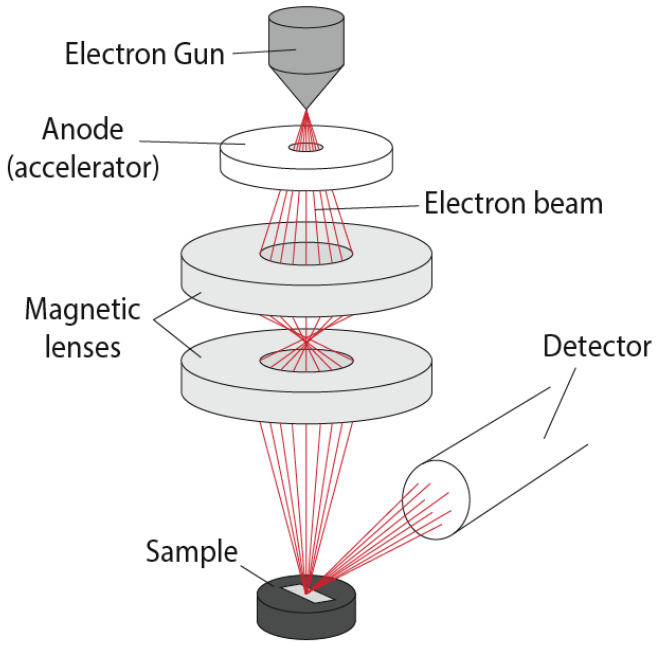

Figure 2.4: Schematic of a scanning electron microscope (SEM). Adapted from [9].

To obtain clear images, cross-sections were often desired, requiring samples to be cleaved to give a surface for the electrons to impact. Cleaving of samples was done using an Oxford Lasers laser machining system to mill a line onto the back of the sample, and then manually cleaving the sample to split along the line.

Overall, SEM can quickly provide a qualitative assessment of the uniformity and coverage of diamond films, and give quantitative data on the thickness of diamond grown and the size of diamond grains, although this often requires samples to be broken. As such, a Jeol IT300 SEM was used throughout this project, albeit usually after all other characterisation for a given sample has been done. Some images were gathered by Dr. Jean-Charles Eloi when the SEM facility had limited availability.

2.6.2 Raman spectroscopy

Raman spectroscopy is a non-destructive means of characterising CVD diamond films. Using lasers with wavelengths of 325, 514 and 785 nm, characteristic Raman peaks can be observed for both sp^3 and sp^2 carbon, and from the intensity of these peaks, qualitative assessment of the diamond can be made. These peaks are observable due to a polarisability shift in the diamond, where a relatively high-energy photon interacts with a phonon mode of the crystal structure, which manifests as a stretching between the (111) planes, resulting in excitation and subsequent decay to a higher vibrational energy – an example of an Anti-Stokes shift.

This change in energy is denoted as the Raman shift, which for sp^3 carbon is observed at 1332.6 cm^{-1}. Raman shift due to polarisability such as that in diamond is uncommon, as usually Raman shift is due to an observed dipole moment (which is what traditional IR spectroscopy looks for), but this is not present in a perfect diamond crystal. As such, Raman spectra at different wavelengths of incident light promote different Raman modes, with sp^3 carbon becoming less prominent at longer wavelengths as graphitic sp^2 modes dominate, with two main bands at ~1370 cm^{-1} and ~1580 cm^{-1}.

These graphitic bands, labelled as the D and G modes for the 1370 and 1580 cm^{-1} shifts respectively, result from different sources [10,11]. The G band (‘ordered Graphitic mode’)is due to the E_{2g} vibration mode, with “stretching” of pairs of sp^2 atoms in the rings and chains of the graphite, causing the shift in polarisability [12], is usually seen as a sharp peak at 1853 cm^{-1} in bulk graphite. The D mode at 1370 cm^{-1} is not observed in defect-free graphite, with the relative intensity of the D peak being indicative of the size of the graphitic crystals, and named D mode for “disorder-induced mode”. However, the cause of the D mode is still debated, with the prevailing theory being that it results from a double-resonant Raman process that enhances a specific phonon wave vector and phonon frequency for a given laser energy [10].

Subsequently, the D and G modes are often observed even in high-quality polycrystalline diamond, due to the mixture of sp^2 and sp^3 carbon at the grain boundaries. The G mode is usually observed as a broad band when looking at CVD diamond, as the stretching mode experiences a range of environments, resulting in a range of energies for the vibrational modes. Similarly, the D mode is often observed as a sharp peak, although usually much smaller than the sp^3 diamond peak which occurs nearby.

With ready access to a Renishaw 2000 Raman spectrometer, Raman data at 514 nm is often used in this project, with other wavelengths of laser used when trying to specifically highlight either the diamond peak or the D and G modes.

2.6.3 Water contact angle

For testing various surface terminations in Chapters 3 and 4, a semi-quantitative method to determine relative hydrophobicity was used, which utilised water contact angle on the surface of the sample. Using a Krüss DSA100 drop shape analyser, a small volume (~5 mm^{-3}) of water was dropped onto a sample, an image taken, and then the angle between the water droplet and the surface was determined using *Advance* software. A hydrophilic surface (i.e. O-terminated diamond) gave a small angle and a hydrophobic surface (i.e. F-terminated diamond) gave a large angle. Figure 2.5 shows an image produced by the software, including the calculated fitting produced.

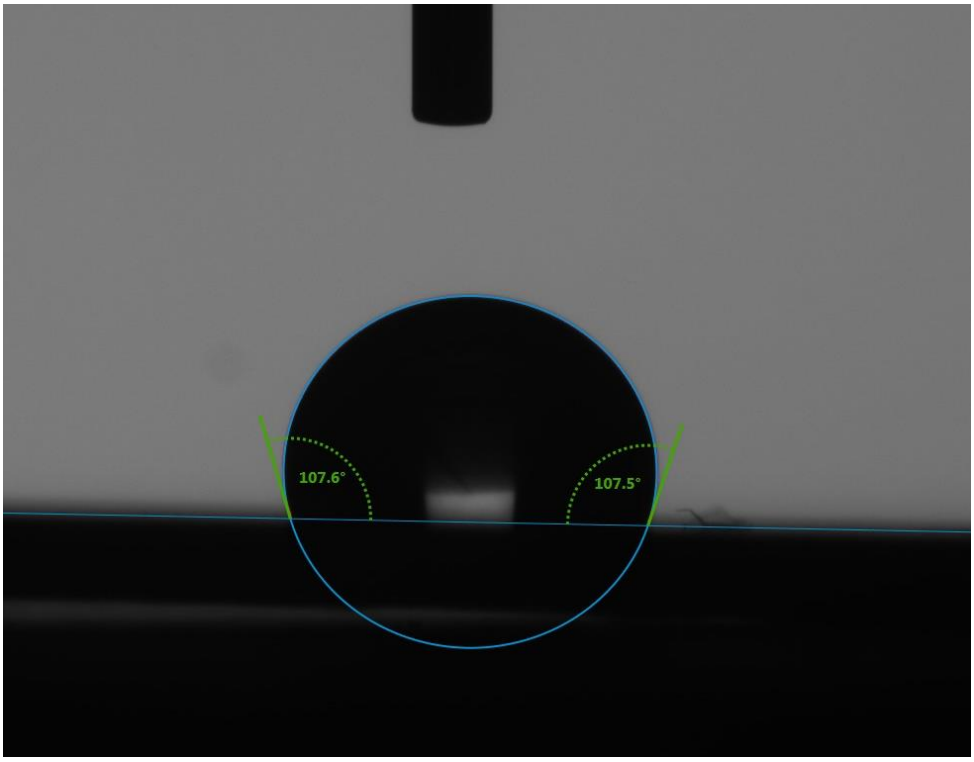

Figure 2.5: Water droplet on a hydrogen-terminated flat diamond sample, as seen using the *Advance* software. Angles are calculated by the software relative to the baseline across the surface of the sample.

2.6.4 Atomic force microscopy

Atomic force microscopy (AFM) is another form of scanning microscopy. AFM probes usually consist of a cantilever – which is oscillated at a known frequency – with a nanosharp tip. This tip contacts the surface of the sample, changing the deflection of the cantilever, which is detected and provides the datum for that point being measured. When the tip is rastered across the sample, it builds an image of the topography of the surface. This technique can resolve the surface at a resolution of <1 nm when desired, but the mechanical hardness of diamond wears out the tips, so for larger areas, a larger interval between points is needed, reducing the resolution. Chapter 4 explores the use of nano-scale structures as a means of templating diamond growth, so a Peakforce Multimode 8 AFM was used extensively to quantify the resultant material, with all AFM data gathered by Dr. Robert Harniman. However, the technique is of little benefit when looking at bulk diamond – especially as the surface roughness of polycrystalline diamond will rapidly blunt the tip – so AFM was not utilised for any of the other experimental work in this thesis.

2.6.5 Transient thermoreflectance

Transient thermoreflectance (TTR) is a method which allows the overall impact of thermal barriers resulting from interfaces between layers to be determined [13]. This technique, developed and operated by collaborators in the Bristol CDTR, uses a rapid, contactless laser reflectance method to map TBR_{eff} for as-grown wafers, with no need for device fabrication [14]. A schematic diagram of the TTR set-up is shown in Figure 2.6.

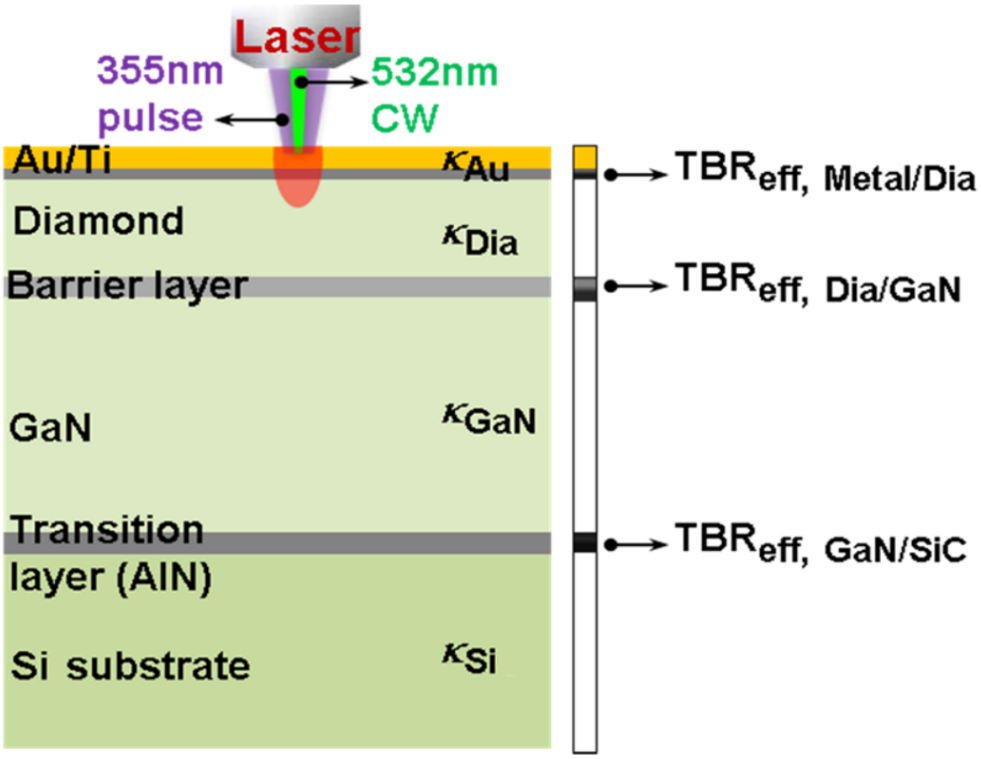

Figure 2.6: Schematic diagram of both the sample structure and the transient thermoreflectance (TTR) measurement method. The left side lists the various materials making up the layered structure of the sample, the middle lists relevant thermal conductivities, κ, and the right side shows the three main interfaces that are considered. Adapted from [15].

For TTR analysis, the diamond surface of each sample was coated with a 100 nm Au transducer layer, with a 10 nm Cr adhesion layer between the Au and the diamond. For these data, the TTR equipment used a 355 nm pulsed-laser (10 ns pulse duration, 30 kHz pulse rate, ~25 µm spot radius) to heat the surface, while a 532 nm continuous wave probe laser (~1 µm spot radius) monitored the changes in surface reflectivity. This change is directly proportional to

the temperature of the material surface, and subsequent fitting to a model allows the thermal properties of the structure to be determined. This technique is discussed in further detail in Chapter 4, where it is used to determine quantitatively the quality of the interface between diamond films and GaN/AlN.

All TTR data were gathered by D. Field, who also fitted the data to produce TBR_{eff} values with assistance from J. Pomeroy and Z. Abdallah, all members of the CDTR.

2.6.6 X-ray tomography

X-ray tomography (XRT) is a non-destructive analytical technique that computationally combines a series of cross-section scans into a 3-dimensional model. X-rays are sequentially fired through a sample, which is rotated between scans, with the detector measuring the attenuation of the X-ray intensity across the sample, which is dependent on both the quantity and the properties of the material it has passed through. From these scans, the quality of a diamond film can be assessed, as well as the presence of any delamination, as this shows up in the image as an area of low material density. The system used was a Zeiss XRadia Versa 520 with voxel resolution of ~1.5 × 1.5 μm when operated at 80 kV and 7 W with a 40× objective lens.

These data are of great use when looking at materials which are likely to delaminate, or where the uniformity of the diamond-substrate interface is of great interest. Therefore, XRT is used in Chapter 4 to give a qualitative assessment of the interface. All XRT data were gathered by G.R. Mackenzie.

2.7 Chapter Summary

This chapter provided an overview of the techniques for growth, seeding, surface termination and characterisation carried out in the work this thesis details. For the growth techniques, the step-by-step process for growth in both the hot-filament and microwave-plasma CVD reactors have been presented, along with 'standard' growth conditions used for the majority of the diamond growth herein. Similarly, the conditions used for seeding the samples prior to growth and for surface termination after growth have been provided. For the numerous characterisation techniques, a concise summary of how they function and what their results show is presented.

Chapter 3 is focussed on growth of thin films of diamond onto a material called black silicon. Given the fragility of the black silicon's surface structure, electrospray seeding was used, followed by growth in the hot-filament CVD reactors. HF CVD was chosen as boron-doped diamond was desired and only these reactors could support boron-doped growth. Additionally, the slower growth rate was vital in ensuring a very thin (<0.2 μm) diamond film was grown to retain the surface morphology. The surfaces of these films were then terminated with hydrogen, oxygen, fluorine, and ammonium to assess the effect of termination on bacterial growth on their surface. SEM and Raman spectroscopy were used to characterise the growth, and water contact angle to determine the effect of the termination methods.

The diamond films grown onto gallium nitride and aluminium nitride used in Chapter 4 were all made in the microwave CVD reactor following seeding by electrospray, with both thin (~2 μm) and thick (~100 μm) layers grown. SEM and Raman spectroscopy were used to examine the diamond films that were grown, XRT to examine the diamond-on-Gan/AlN structure, and TTR to characterise the thermal boundary resistance of the structure.

When working on the self-assembled polymer micelles that are presented in Chapter 5, initially HF CVD was used, but most of the project was carried out using the MW CVD reactor for growth. Seeding was done by manual abrasion when required, but the micelles themselves were deposited onto unseeded Si substrates prior to growth. AFM was used to characterise the micelles before and after growth steps, with SEM and Raman spectroscopy only able to be used on the thickest structures grown.

References

1 May, P. W. Diamond thin films: a 21st-century material. *Phil. Trans. R. Soc. Lond. A*, 358 (2000), 473-495.

2 James, M. C. *Aluminium and Oxygen Termination of Diamond for Thermionic Applications*. Ph.D thesis, University of Bristol, Bristol, UK, 2019.

3 Martin, T. L. *Lithium oxygen termination as a negative electron affinity surface on diamond: a computational and photoemission study*. University of Bristol, Bristol, UK, 2011.

4 Tsutsumoto, T. *Thin Solid Films*, 317 (1998), 371.

5 Croot, A. *Boron and nitrogen in diamond: an ab initio simulation, plasma emission spectroscopy and material deposition & characterisation study*. University of Bristol, Bristol, 2018.

6 Abedrabbo, S., Hensel, J. C., Gokce, O. H., Tong, F. M., Sopori, B., Fiory, A. T., and Ravindra, N. M. *MRS Online Proceedings Library*, 525 (1998), 95.

7 Fox, O. J. L., Holloway, J. O. P., Fuge, G. M., May, P. W., and Ashfold, M. N. R. *Mater. Res. Soc. Symp. Proc.*, 1203 (2010), J17.

8 Al-Jeda, T. *Construction and Operation of a Plasma System to Fluorinate and Aminate the Surfaces of Diamond Thin Films*. University of Bristol, Bristol, 2018.

9 Choudhary, O. P. and Choudhary, P. *Int. J. Curr. Microbiol. Appl. Sci.*, 6 (2017), 1877.

10 Reich, S. and Thomsen, C. Raman spectroscopy of Graphite. *Phil. Trans. R. Soc. Lond. A*, 362 (2004), 2271.

11 Kostić, R., Mirić, M., Radić, T., Radović, M., Gajić, R., and Popović, Z. V. *Acta Physica Polonica A*, 116 (2009), 718.

12 Ferrari, A. C. *Solid State Commun.*, 143 (2007), 47.

13 Pomeroy, J. W., Simon, R. B., Sun, H., Francis, D., Faili, F., Twitchen, D. J., and Kuball, M. *IEEE Electron Device Lett.*, 35 (2014), 1007.

14 Pomeroy, J. W., Simon, R. B., Sun, H., Francis, D., Faili, F., Twitchen, D. J., and Kuball, M. *IEEE Electron Device Lett.*, 35 (2014), 1007.

15 Zhou, Y., Anaya, J., Pomeroy, J. et al. *ACS Appl. Mater. Interfaces*, 9 (2017), 34416.

16 May, P. W., Rego, C. A., Ashfold, M. N. R. et al. The Production of CVD Diamond-Coated Wires and Free-Standing Diamond Tubes. *Proc. 4th Int. Conf. New Diamond Sci. Technol.* (1994), 211.

Chapter 3 – Diamond growth on black silicon and using black diamond as an antibacterial surface

3.1 Chapter objectives

Bacterial resistance is rapidly becoming a major issue, with new strains being more able to survive existing antibiotic treatments; as such, other approaches of stopping bacterial proliferation are being investigated. One such method is using a surface capable of rupturing the cells physically rather than chemically, with a material called black silicon seen as a promising option for this. However, the viability of black silicon for real-world applications is limited, in part due to its brittle nature, making it unsuitable for most uses: by using a thin coating of diamond on the black silicon, the durability could be improved while offering the opportunity to also enhance the antibacterial potential of the surface. This chapter focuses on exploring this opportunity.

The aim of this project was to expand on the work done previously within the University of Bristol Diamond Group with respect to diamond-coated black silicon, black diamond (D-bSi). Three sets of samples were utilised to explore different variables, with the focus on achieving an effective coating of the bSi samples with diamond, and any subsequent surface termination.

The first set of experiments used black silicon (bSi) with an intermediate needle length and separation to previous work, with the aim of exploring and optimising these parameters for bactericidal properties against Gram-negative *E. coli*. Additionally, a range of surface terminations were applied to both the bSi and D-bSi samples to assess the impact of hydrophobicity and hydrophilicity in causing bacterial death. The results were sufficiently conclusive that the results were published [1], and this experimental set also made the core of a undergraduate project [2].

The second experiment built on the understanding of the first, using two sets of smaller and more densely packed needles to be more suitable for the smaller Gram-positive *S. aureus* bacteria. With a smaller needle size and reduced spacing, these posed a greater challenge for diamond growth, trying to balance fully coating the needles without overgrowing and making them too thick to be effective at killing the bacteria. This set were also used as the basis of an undergraduate MSci project [3].

The third set aimed to expand on the second, using *S. aureus* and *S. epidermidis*, both Gram-positive bacteria. From the results of the second set, longer bSi needles were selected with a similar separation. Diamond coating of these bSi needles proved to be the most challenging, as the greater length further exacerbated the challenges faced for the second set, ultimately requiring a new seeding technique to be developed. Bacterial testing showed promising results, and a publication was being prepared at the time of writing.

Much of the repetitive growth runs were carried out by undergraduate MSci students Olivia Dunseath (1st set) and James McGrath (2nd set) as well as by visiting PhD student Kaili Yao (3rd set) under the instruction of the author. SEM images of bSi and D-bSi before bacterial testing for the 3rd set were obtained by Jean-Charles Eloi. Bacterial culturing, testing and SEM images after bacterial exposure were obtained by Gavin Hazell and Sophie King (1st set, University of Bristol) and Neda Nouruzi (2nd and 3rd set, University Medical Center Groningen).

3.2 Introduction

3.2.1 Black Silicon

Black silicon (bSi) is a term given to describe silicon which has been synthetically nanostructured to feature high-aspect-ratio spikes or needles, with the light absorbing nature of these needles making the material appear black. These spikes can be generated through a few different techniques, usually utilising plasma etching methods [4], with the spikes themselves forming through anisotropic etching of the Si surface alongside deposition of micromasks [5,6]. bSi formation is usually undesirable in Si wafer manufacture, but the material has found applications in photovoltaics [7] and biomedical sensing [8], so much so that it is commercially available for these uses. Figure 3.1 shows an example of the bSi used for the work in this thesis, but the length and separation of the needles, as well as the radius of the needles themselves, can all be controlled by the etching conditions used; bSi needles ranging from <1 µm to 10s of µm can be produced.

The appearance of bSi is due to the low reflectivity and high absorbance of the spikes, resulting from the needles being of similar scale as the wavelength of visible light [9]. As such, bSi is of interest for solar cell technologies due to its absorbance of much of the incident light [7].

Similarly, the extremely high surface area of the bSi structure has made it of notable interest in electrochemical applications as an electrode when the Si is doped to be conductive [10].

However, the property of bSi of most interest in this thesis is its potential to act as a bactericidal surface, with the nanostructure similar to that of a cicada's wings, which are naturally effective at killing bacteria [11]. This similarity was explored showing bSi to be effective against both *P. aeruginosa* and *S. aureus* – Gram-negative and Gram-positive bacteria respectively [12]. However, bSi is a fragile material with the needles being both thin and brittle, which significantly limits its use in most real-world applications [10]. Not only does mechanical damage to or even loss of the needles reduce the bactericidal efficacy of the bSi, but the isolated needles themselves pose a potential health hazard when floating in the air, being of similar size and shape to asbestos fibres. Unless the needles can be strengthened, bSi remains of little value as a bactericidal surface outside of a laboratory testing environment, hence the requirement to coat them with diamond.

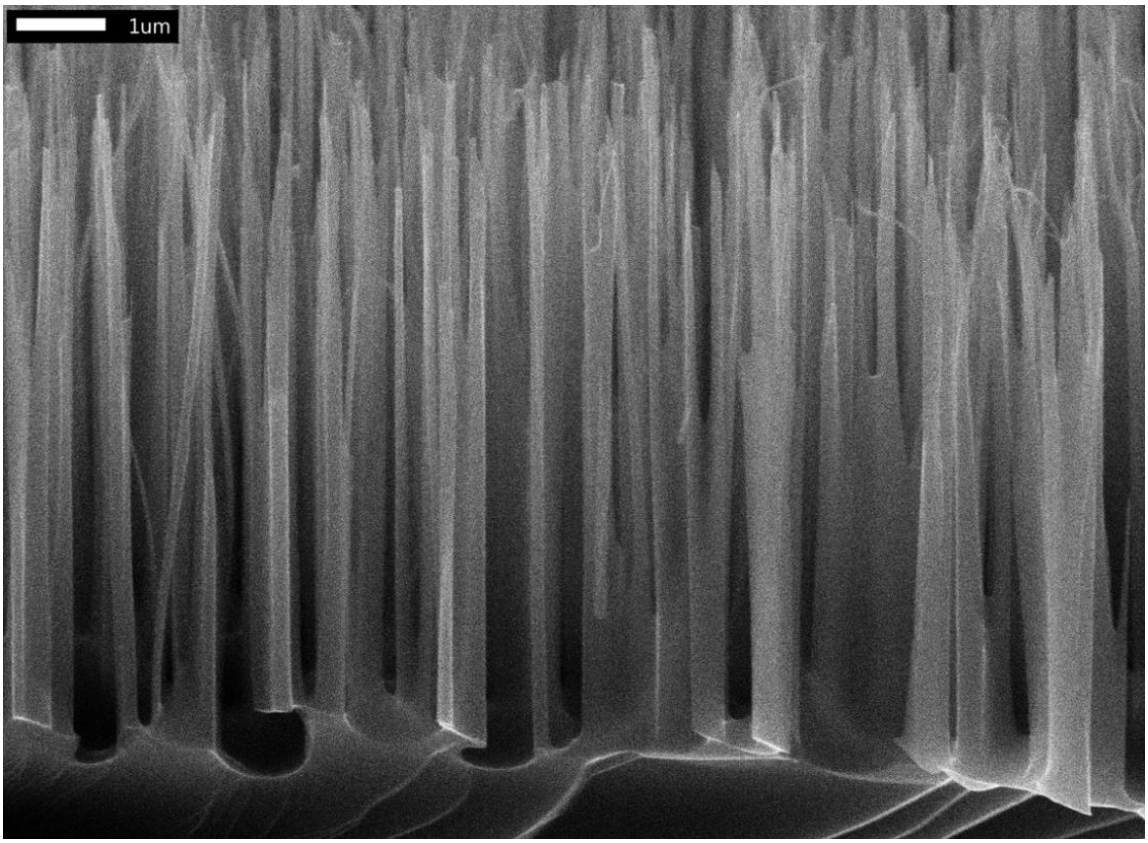

Figure 3.1: Black silicon cross-section seen *via* SEM, with needles ~5 µm long, tip separation of ~0.5 µm and tip radius of ~10 nm.

3.2.2 Bacteria and biofilms

As bacteria evolve to resist human efforts to kill them, in particular by developing resistance to antibiotics, the threat to human health from harmful bacteria is becoming a major concern. Most current antibacterial methods focus on preventing bacterial reproduction, with antibiotics the primary means of controlling infections. However, new antibiotics are expensive to produce but limited in profitability, which means pharmaceutical developers are less willing to invest money into researching them [13]. As such, alternative methods of reducing bacterial growth are becoming of increasing importance.

Bacteria are at their most vulnerable to antibiotics either before or shortly after they attach to a surface. However, once the bacteria have begun to reproduce, many pathogenic bacteria produce a matrix of extracellular polymeric substances (EPSs) which coat the surface forming a biofilm – this is called biofouling. These biofilms protect the bacteria, making once-treatable bacterial strains 10s to 100s of times less sensitive to previously effective antibiotics [14]. Biofouling on materials inside the human body, such as implants, is untreatable, with the only method to remove pathogenic bacterial biofilms being to remove the implanted material and physically clean it [15].

Bacterial adhesion on non-living surfaces usually occurs in two steps. The first is called the docking phase, where bacteria adhere to the surface *via* a range of forces, predominantly van der Waals, electrostatic and steric, and this step is often reversible. The second step is the typically irreversible anchoring step, where the adherent bacteria may begin to produce EPS, allowing the biofilm to form and greatly enabling further bacterial growth and cellular adhesion of other microorganisms [16]. As such, if bacterial growth can be stopped before anchoring can occur, then the bacteria are less able to reproduce. This can be achieved both by nature and synthetically through modifications of the surface, which is discussed further in Section 3.1.3.

Bacteria are usually separated into two classifications – Gram-positive and Gram-negative – which group bacteria based on their type of cell walls. A schematic diagram of the differences is shown in Figure 3.2. Gram-positive bacteria are the more common and their cell wall consists of only 30-100 nm thick peptidoglycan (PG), a series of repeating disaccharides that cross-link to provide rigidity and protect the cell membrane. Gram-negative bacteria have a more complex cell wall, with only a thin layer (~8 nm) of PG which is capped with an additional lipid membrane and a coating of lipopolysaccharides [17]. The additional layers offer protection against antibiotics and make the cell wall more rigid. Conversely, Gram-positive bacteria are

more flexible and thus more able to withstand mechanical stresses. As such, Gram-positive bacteria are more able to conform to a rougher surface without rupturing the cell wall. However, Gram-negative bacteria also have the additional means to anchor themselves to surfaces, as they are able to express organelles called *fimbriae*. *Fimbriae* are proteins which look similar to hairs, and aid in anchoring by producing EPS.

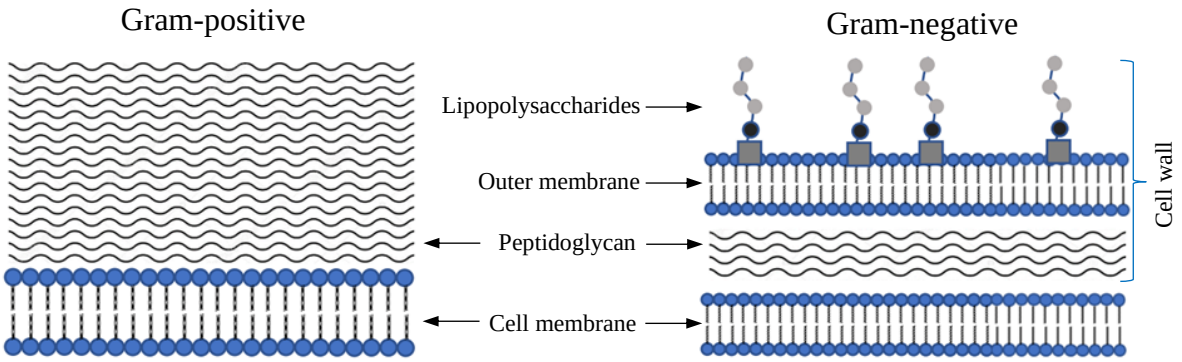

Figure 3.2: Cell wall compositions of both Gram-positive (left) and Gram-negative (right) bacteria.

Within this project, both Gram-positive and Gram-negative bacteria were used. For Gram-negative experiments, *Escherichia coli* was used. *E. coli* is commonly found in mammalian digestive systems and most strains are not considered harmful, with cells usually rod-shaped and ~ 2 µm long. *E. coli* can also be cultured easily in laboratory environments, so is often used for bactericidal testing. *E. coli* expresses *fimbriae*, which can serve as an easy visual means to determine if the cells are healthy – if there are no *fimbriae* expressed, then this suggests that the bactericidal material has successfully impeded the bacterial growth [18].

Staphylococcus aureus was chosen for Gram-positive bacteria experiments, as *S. aureus* is another commonly found bacterium, growing readily on skin, with many non-harmful strains available for experimentation. However, some strains of *S. aureus* are life-threatening and account for one of the most common causes of hospital-acquired infections. As such, extensive studies have been carried out on *S. aureus*, so the structure of the cell wall is well understood. Their PG layer is composed largely of *N*-acetylglucosamine, providing a lot of rigidity to the cell wall, and the cells are usually spherical with diameter less than 1 µm [19]. This presents a very different structure to attempt to combat through bactericidal surfaces than those of *E. coli*. *S. aureus* may also produce a biofilm through EPS production, with the strains that produce EPS often being more antibiotic-resistant [20].

3.2.3 Surface modification to resist bacterial growth

Nature has found many ways to stop large-scale bacteria growth, usually through two main methods: either by making it hard for biofilms to form on a surface, or by having some mechanism to kill bacteria before they can form a biofilm. As such, many artificial methods to resist and kill bacteria emulate those found in nature.

Bacteria-resistant materials are those that are effective at preventing bacteria from reproducing and from forming biofilms. The most commonly found method to achieve this in nature utilises surface wettability, either to make the surface hydrophobic or hydrophilic, both of which can assist in resisting bacterial growth. Increased hydrophobicity of surfaces has been shown to reduce how easily bacteria can adhere to that surface, and hence reduce biofilm formation [21]. A good example of this is lotus leaves, the surface of which is superhydrophobic, causing a high water contact angle, resulting in water forming droplets and rolling off of the leaves, taking any other material such as bacterial cells with it [22]. This also provides advantages to materials in aqueous environments, as the hydrophobic surface results in an air layer between the material and the bacteria-containing solution, again reducing the ability of the bacteria to adhere to the surface [23]. In contrast, a hydrophilic surface can be beneficial for bacterial resistance when in an aqueous environment, as the surface adsorbs a layer of water molecules, providing a barrier to bacterial adherence both sterically and energetically [24]. However, this resistance only functions when in an aqueous environment, somewhat reducing its efficacy.

Conversely, bactericidal materials are those which kill bacterial cells on contact, either chemically or physically. Humans have developed many chemical routes to kill bacteria, the most apparent of which is the use of antibiotics, but other materials such as using silver nanoparticles are also used. These methods utilise chemistry to degrade bacterial cell walls, killing the bacteria.

Nature has also developed physically bactericidal materials, usually utilising nanoscale protrusions from the surface. Gecko skin is covered in an array of spinules ~2 μm long which have been shown to be a highly effective at killing *P. gingivalis*, a Gram-negative bacterium [25]. Similarly, cicada wings, with a hexagonal array of nanopillars, each pillar ~200 nm tall and spaced ~170 nm tip-to-tip, were shown to be effective at killing *P. aeruginosa*, another Gram-negative bacterium [12]. Dragonflies also have a similar structuring on their wings, however, the pillars are of bimodal lengths, with half ~190 nm and half ~310 nm, providing similar bactericidal properties [26].

These materials were reported to be effective at killing bacteria, with the prevailing theory of the mechanism being based on the cell wall stretching to the point of rupture, determined through modelling of the cicada wing structure [27]. Figure 3.3 shows the side elevation diagram of a bacterium between two nanopillars. The bacterium, driven through a combination of gravity and van der Waals forces, stretches over the nanopillars as it attempts to fill the spaces between the pillars. The difference between the surface area that is directly in contact with the material (S_A) and the surface area that is not in contact with the material (S_B) determines the stretching degree. When the stretching degree reaches a certain threshold, the bacterial cell will rupture, killing it. Using this model, it was found that most Gram-negative bacteria can be killed by the nanopillar structure on cicada wings; with only 1-3 layers of PG, the cell wall is relatively flexible allowing this stretching to occur. In contrast, the maximum membrane stretching for Gram-positive bacteria was not enough to cause rupture, as the 10-50 layers of PG cause the cell wall to be rigid. As such, this model suggests that the bactericidal property of these nanopillars could be enhanced through increasing sharpness of the pillars (causing more of a puncturing effect) and by increasing the spacing between the pillars.

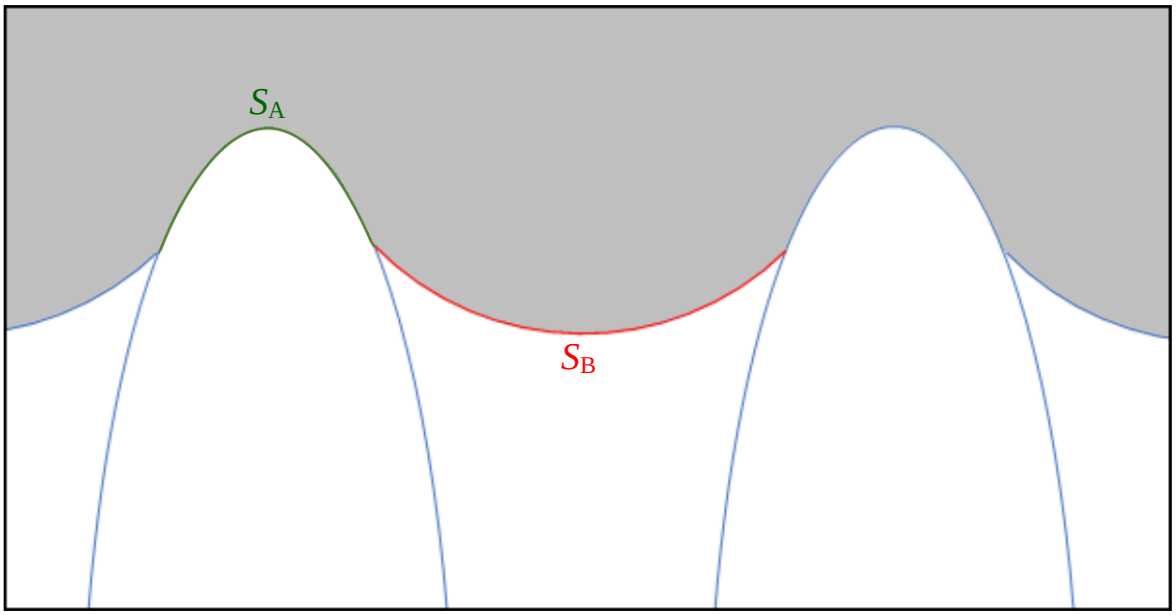

Figure 3.3: A side elevation representation of a bacterium sinking between two nanopillars. S_A is the surface area of the cell wall touching the pillar, and S_B is the surface area suspended between the two pillars. As the bacterium sinks, the cell wall is stretched across the nanopillar, eventually causing the cell wall to rupture. Adapted from [27].

3.2.4 Prior work using bSi as a bactericidal surface

Black silicon, with its ability to be modified both in the height of its needles and in the spacing of them, therefore has great potential for use as a bactericidal material. Some initial work showed that bSi structures were effective at killing bacteria in a similar way to cicada wings [12], and further research carried out at the University of Bristol showed that diamond-coating of bSi to produce black diamond (D-bSi) did not diminish the bactericidal properties of the surface [10]. D-bSi is also more robust than bSi, with the diamond coated needles being more able to withstand mechanical stresses than the uncoated bSi needles.

Further work explored the effect of the size of the bSi and D-bSi needles using a range of needle lengths, tip diameters and needle densities [28]. Firstly, growing diamond onto the bSi did round off the tips, but did not reduce the bacterial death rate, confirming that the mechanism for cell death was not simply penetration of the sharp bSi needles, supporting the mechanism of cell wall rupture due to stretching as proposed by Xue [27].

The main results of this work determined that the needle length was much less significant than the needle density with respect to bacterial death; as a trend, a higher needle density resulted in more *E. coli* death. However, this was also shown to need careful balancing – too high a needle density and the bacterial cells simply sit on top of the needles, exhibiting a "bed of nails" effect [29]. Conversely, too sparse and the bacterium can lie between the needles, rather than being stretched over them. Additionally, when the needles were too short, the bacteria were not stretched enough to rupture before they settled at the bottom of the nanostructured surface, leading to reduced bacterial death.

Also highlighted in the prior work was the comparative efficacy of bSi and D-bSi at killing Gram-negative and Gram-positive bacteria. bSi and D-bSi were both effective as bactericidal surfaces for Gram-negative *E. coli* but were unable to kill significant quantities of Gram-positive *S. gordonii*. This was attributed to *S. gordonii* having a thicker cell wall and thus being more rigid and less prone to rupturing [28].

The effect of motility was also considered to be significant, with *E. coli* being a motile bacterium, attempting to spread horizontally to find a better anchor, and thus causing more cell wall strain across the surface of the bSi and D-bSi more, in turn resulting in a higher cell-death count. Conversely, *S. gordonii* is non-motile, growing in chains and not spreading out, leading to less strain on the cell wall [28].

3.3 Experimental methods

3.3.1 Black silicon preparation

For the first two experimental sets, the 100 mm diameter black silicon wafers used were all provided by Colin Welch at Oxford Instruments Plasma Technology (Yatton, Bristol). The bSi samples were prepared using reactive ion etching (RIE) in a Cl_2/O_2 plasma. In this technique, an inductively coupled radio frequency (RF) power was used to sustain a plasma, and a second RF supply was then coupled to one electrode to create a DC bias. This bias in turn caused ion bombardment to occur on the substrate at a rate which was controlled by the power supply. Sustaining this plasma for 10 minutes using Cl_2 (48 sccm) and O_2 (2 sccm) at 15 mtorr, with the RF supplies providing 100 and 600 W to the reactor respectively, resulting in a bias of -227 V, resulted in the production of bSi with needles with a range of heights. During RIE, the wafer was cooled by He gas flowing at 10 sccm across the back of the wafer to maintain 20°C [1]. For the third set, a 300 mm diameter bSi wafer was provided by Tom Kamp of Lam Research (Ca, USA), using a similar RIE technique.

Before use, these wafers were manually cleaved using a diamond-tipped scribe to produce squares of ~10×10 mm, with great care taken when handling them to ensure that the bSi side of the wafers were undamaged before use.

3.3.2 Seeding of bSi samples

Samples for all three sets were seeded using the electrospray seeding technique outlined in Section 2.4.3, using a standard seeding solution. This solution consisted of 10 drops (~40 µL per drop) of a detonation nanodiamond colloid (3.3 ± 0.6 nm, 1 wt% in water, Amando) in 30 mL of methanol. When optimising the growth of diamond on a given set of bSi samples, the volume of seeding solution was sometimes varied to ensure that the needles were coated uniformly over their entire length.

In order to ensure statistical reliability in the subsequent bactericidal test, a number of identical samples had to be prepared, along with a control sample, for each test. Our collaborators who performed these tests informed us that 6 identical samples is the minimum number for this purpose. As such, 6 samples were simultaneously seeded per batch, with all the samples for each experimental set seeded consecutively on the same day to reduce variation from seeding solution aggregation. The seeded samples were then mixed together to randomise any minor

variations from the seeding, with the intention of ensuring any inconsistencies in the seeding would be applied across the entire sample set rather than just one individual set of conditions.

For the third set of samples, the bSi was found to be too densely packed for electrospray to fully coat the needles. As such, an alternative seeding method, outlined in Section 2.4.4, was developed, based on submersion of the samples in the seeding solution. The development and optimisation of this is discussed further in Section 3.5.

3.3.3 Diamond growth

Diamond growth for all experimental work in this chapter was carried out in the HF reactors as described in Section 2.1. Growth conditions were mostly consistent across all the sample sets, with the only varied parameters being growth duration and diborane addition. The first experimental set were made in the undoped HF chamber, while the other two were made in the B-doped HF chamber and included a flow of 3.5 sccm of 5% B_2H_6 in H_2 in the gas mixture during growth. Growth duration was varied to find an optimal diamond film thickness, with a uniform coating of diamond on the needles, but without overgrowth causing the needles to become too blunt.

The B-doping was not considered to be relevant to the bactericidal nature of the D-bSi due to the primary mechanism of bacterial death being that of cell wall rupture thought to be primarily controlled by the distribution of the needles and their surface termination; however, it made these same samples useful for separate experiments as electrochemical electrodes, unrelated to this thesis.

Similarly, the primary goal of the growth was to ensure that the majority of the bSi needles were coated with a uniform and pin-hole free diamond coating, as this would allow for the mechanism of cell rupture to occur fully on the diamond surface. As such, the grain size was not considered to be an important criterion in optimising the growth conditions.

3.3.4 Termination of samples

A diamond surface can be readily functionalised using chemical or plasma methods to alter its chemical and electrical properties. As such, one of the main foci of this chapter is modifying the surface termination of the D-bSi to see the impact of varying hydrophilicity/hydrophobicity

on bactericidal ability. To do this, terminations were carried out as described in Section 2.5.2, with O, F and NH_2 terminations all tested for the first experimental set. Following on from the results in this set, it was determined that only the F termination was of particular interest, so the later sets only explored fluorination of the bSi and D-bSi samples.

3.3.5 Control samples

A flat diamond sample to act as a control was prepared for every set of D-bSi sent for bacterial testing. These are not discussed in depth in the subsequent sections, as all of these samples were prepared identically for each set. A 10×10 mm laser-cut square of single-crystal Si (100) was seeded by manual abrasion, then diamond was grown onto this using the same conditions as the given D-bSi sample set, except for 8 h rather than a few min, to produce a ~3 µm-thick microcrystalline diamond film with surface roughness of ~0.25 µm. The control samples were then terminated simultaneously with the given D-bSi sample set to ensure identical termination.

Along with 'flat' diamond control samples, both flat Si and uncoated bSi samples were also provided as controls for bacterial culture experiments. These samples were also terminated to allow for conclusions to be drawn across a broader range of conditions.

3.3.6 Characterisation

SEM, Raman spectroscopy and water contact angle were all used to characterise the samples produced in this chapter – see Sections 2.6.1, 2.6.2 and 2.6.3 respectively.

SEM was chosen as it allowed an effective means to observe the uniformity of the diamond coating on the bSi samples. Samples were mechanically cleaved to give a clean edge, allowing cross-sectional images to be taken. SEM was also used for assessment of damage done to bacterial cells – these later images were taken by Sophie King of Bristol Dental School for the first sample set and by Neda Norouzi of University Medical Center Groningen (UMCG) for the latter sets.

Raman spectroscopy provided insight into the quality of the diamond grown, however, given the thicknesses of the nano-diamond coatings grown, they showed an expected significant sp^2 contribution.

Water contact angle was used to provide a measure of relative hydrophobicity of the samples. However, with the mixture of surface roughness values due to the structure of bSi, the flat

samples were expected to be incomparable to the D-bSi and bSi samples. Water contact angle tests did provide a useful means to confirm the presence of F, O or H terminations, with significant differences observed in the angles for these.

3.3.7 Bactericidal testing

To test the bactericidal nature of the bSi and D-bSi samples, cultures of bacteria were grown by our collaborators at the Bristol Dental School or Groningen University. For each experiment, broth cultures of the given bacterial strain were grown in Tryptic Soy Broth (TSB, Oxoid) for 16 h at 37°C in aerobic conditions. The first experiment used *E. coli* DH5-α, the second used *S. aureus* ATCC 12600, and the third used both *S. aureus* ATCC 12600 and *S. epidermidis* ATCC 12228. The methods used for the culturing for the first set are detailed in [1], and the method used for both the second and third set are outlined in [3].

Live/dead assay was used by our collaborators for all experimental sets as a simple quantitative means to determine bacterial death and hence bactericidal efficacy of the surfaces. Samples were rinsed with 70% ethanol and air-dried, then submerged into 2 mL of the bacterial suspension for 1 h at 37°C. The samples were then rinsed with tris-HCl buffer to remove any loose bacterial cells. Using a bacterial viability stain (BacLight Live/Dead), the samples were incubated in darkness for 15 min at 21°C, then rinsed in phosphate-buffered saline (PBS). 4 images per sample were taken using fluorescence microscopy, where numbers of live (SYTO9, green) and dead (propidium iodide, red) cells were recorded.

Colony-forming unit (CFU) count was also used to assess longer-term bacterial growth on the surfaces resulting from biofilm formation. For this, samples were rinsed with 70% ethanol, then 2 mL of the bacterial suspension was added to each sample and then incubated at 37°C for 24 h. Samples were then gently washed in PBS to remove any non-adhered bacteria, then sonicated in 1 mL PBS for 5 min to detach adhered bacteria into suspension with the PBS. These suspensions were then serially diluted in 10-fold steps with PBS, before being spread over TSB agar plate. The TSB plates were incubated at 37°C – to emulate human body temperature – for 14 h, and then the number of colonies counted. This was only done for the Gram-positive bacteria experiments.

3.4 Results

3.4.1 Diamond-on-7 µm bSi for Gram-negative *E. coli*

The bSi chosen for this experiment had needles of a range of heights up to ~7 µm long and a suitable needle density of ~3 μm^{-2} – although much lower density of the 7 µm needles – shown in Figure 3.4. Growth was carried out on these needles for 60 minutes, resulting in a uniform coating along the entire length and with SEM images showing consistent growth on samples from the first growth runs to the last, presented in Figure 3.5.

The surface termination was then modified, with control samples of flat diamond included for comparison. The effect of these terminations on the hydrophobicity of the surfaces was then assessed using water contact angle, the results of which are presented in Table 3.1, along with literature values where appropriate.

These samples were then exposed to the *E. coli* bacterial solution and Live/Dead staining, with the results shown in Figure 3.6.

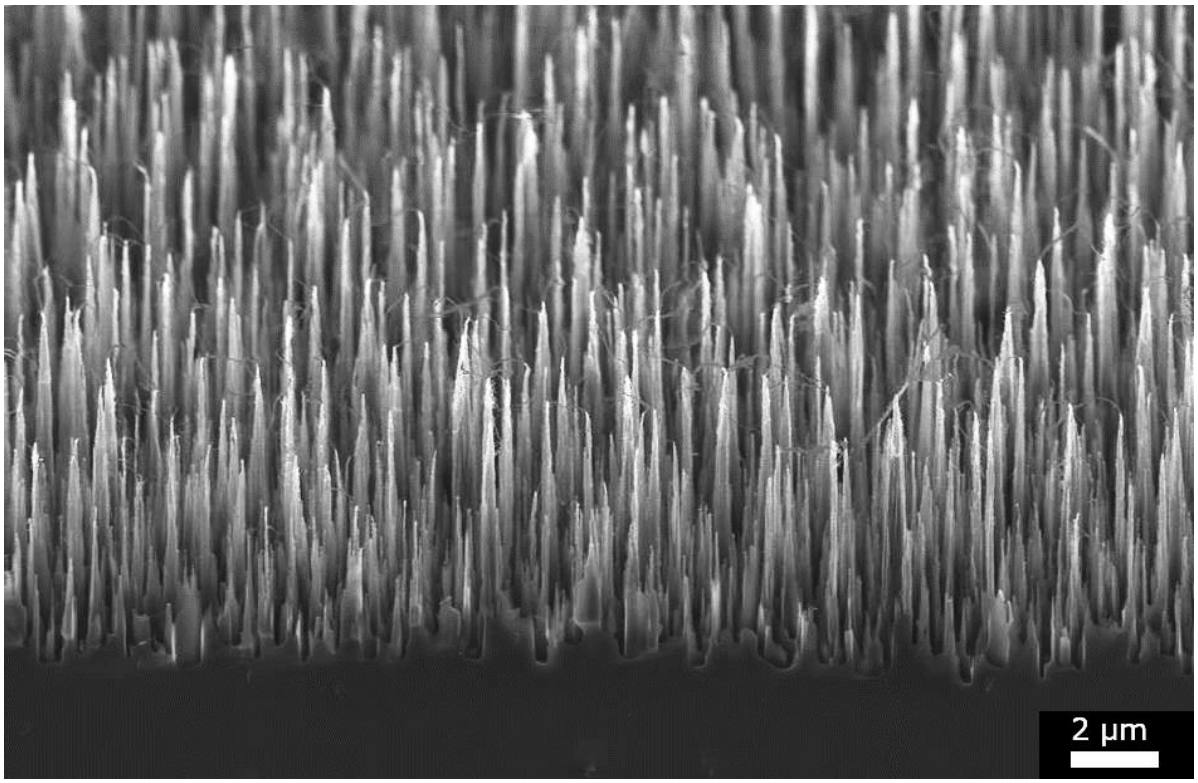

Figure 3.4: SEM image of bSi used for experimental work with *E. coli*. Tallest needles are ~7 µm.

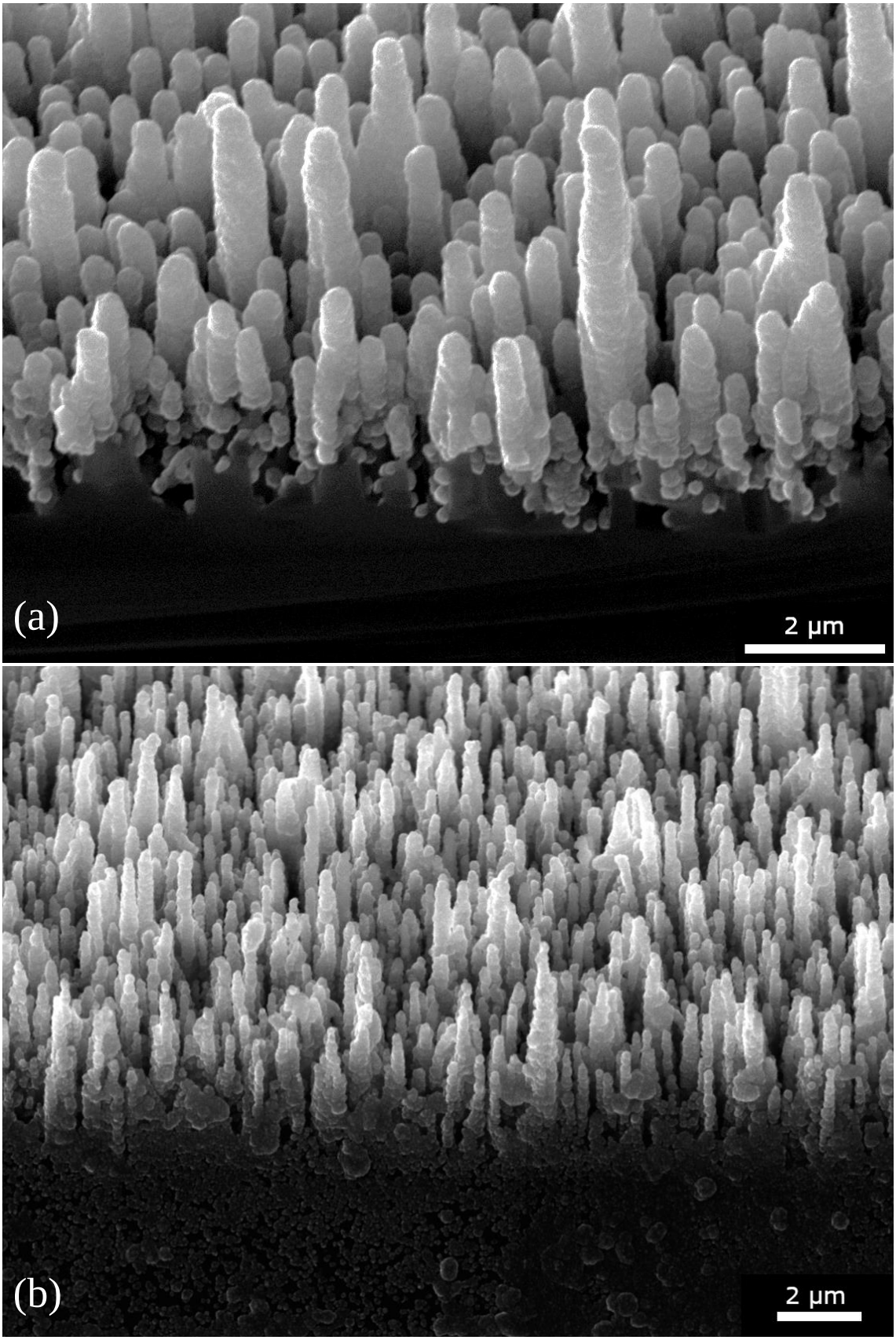

Figure 3.5: SEM images of diamond-coated bSi used for *E. coli* experiments. (a) is one of the first set of samples coated, and (b) is one of the last set. Both show good coverage over the whole length of the needle.

Table 3.1: Water contact angle results for the samples used for *E. coli* experiments. Literature values from [30] are included where appropriate. *Although the bSi needles were not deliberately terminated, they will likely have a native oxide layer of a few nm thickness.

Sample surface	Termination	Contact angle / °	Literature / °
bSi	Not terminated*	84	-
Flat diamond	H	64	83
	O	49	75
	F	104	107
	NH_2	57	-
D-bSi	H	85	-
	O	5	-
	F	137	-

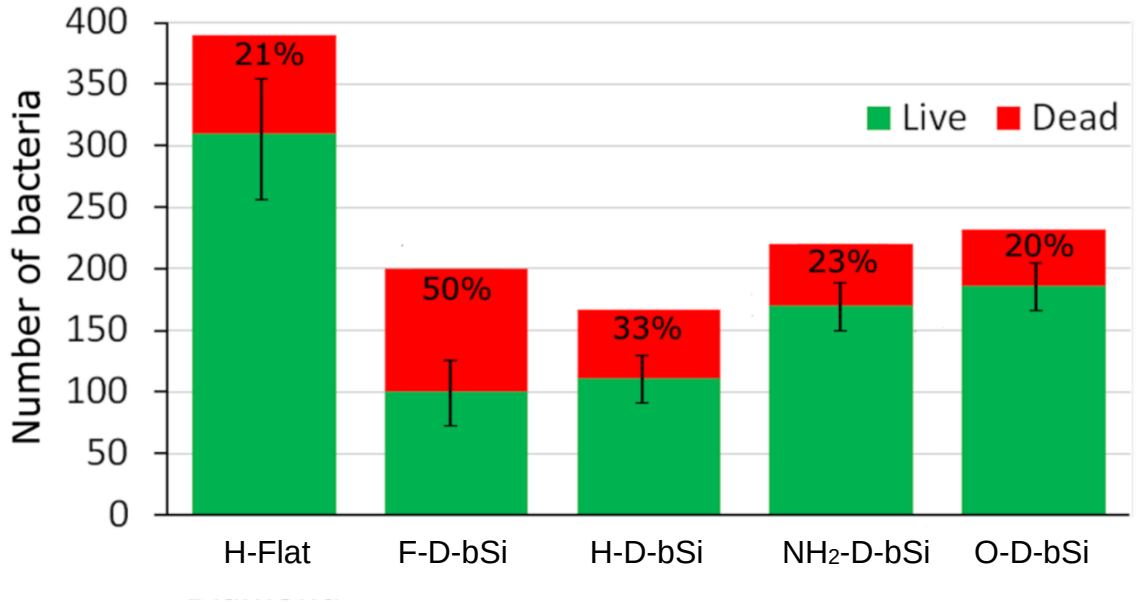

Figure 3.6: *E. Coli* bacterial viability as determined using Live/Dead staining for different terminations on identical D-bSi samples, with a H-terminated flat diamond control. Total numbers of bacteria adhered to the samples, along with the numbers of living (green) and dead (red) cells indicated. The percentage of dead cells for each sample is indicated and error bars represent one standard deviation of the number of dead cells based on 4 samples tested for each termination.

3.4.2 Diamond-on-1.3 µm bSi pyramids and 2.5 µm needles for Gram-positive *S. aureus*

For this experimental set, two sets of bSi samples were chosen, shown in Figure 3.7; one batch were uniform needles of ~2.5 µm, but a needle density of ~3 μm^{-2}, and the other were pyramidal in shape, on average 1.3 µm – these are shown in Figure 3.7 (a) and (b) respectively.

Using the 1.3 µm pyramidal bSi, growth was carried out for 60 minutes initially, but the surface morphology became overgrown, shown in Figure 3.8, so growths were carried out for 30 and 45 minutes additionally, shown in Figure 3.9 (a) and (b). However, these were considered too smooth to be capable of causing cell wall rupture and so no bacterial testing was performed.

Diamond coating of the 2.5 µm needles was initially done for 60 minutes, but this caused overgrowth as shown in Figure 3.10. As such, 40 and 20 minute growth runs were carried out, with 20 minutes providing suitable growth, shown in Figure 3.11 (a) and (b).

Both H- and F- terminations were carried out using the 20 minutes D-bSi using the 2.5 µm needles, but the samples wetted completely during water contact angle testing, so no angles could be determined.

Live/Dead assay was then carried out following exposure to *S. aureus*, with results shown in Figure 3.12, and then incubated for 24 hours to provide to allow for counting of colony forming units, presented in Figure 3.13.

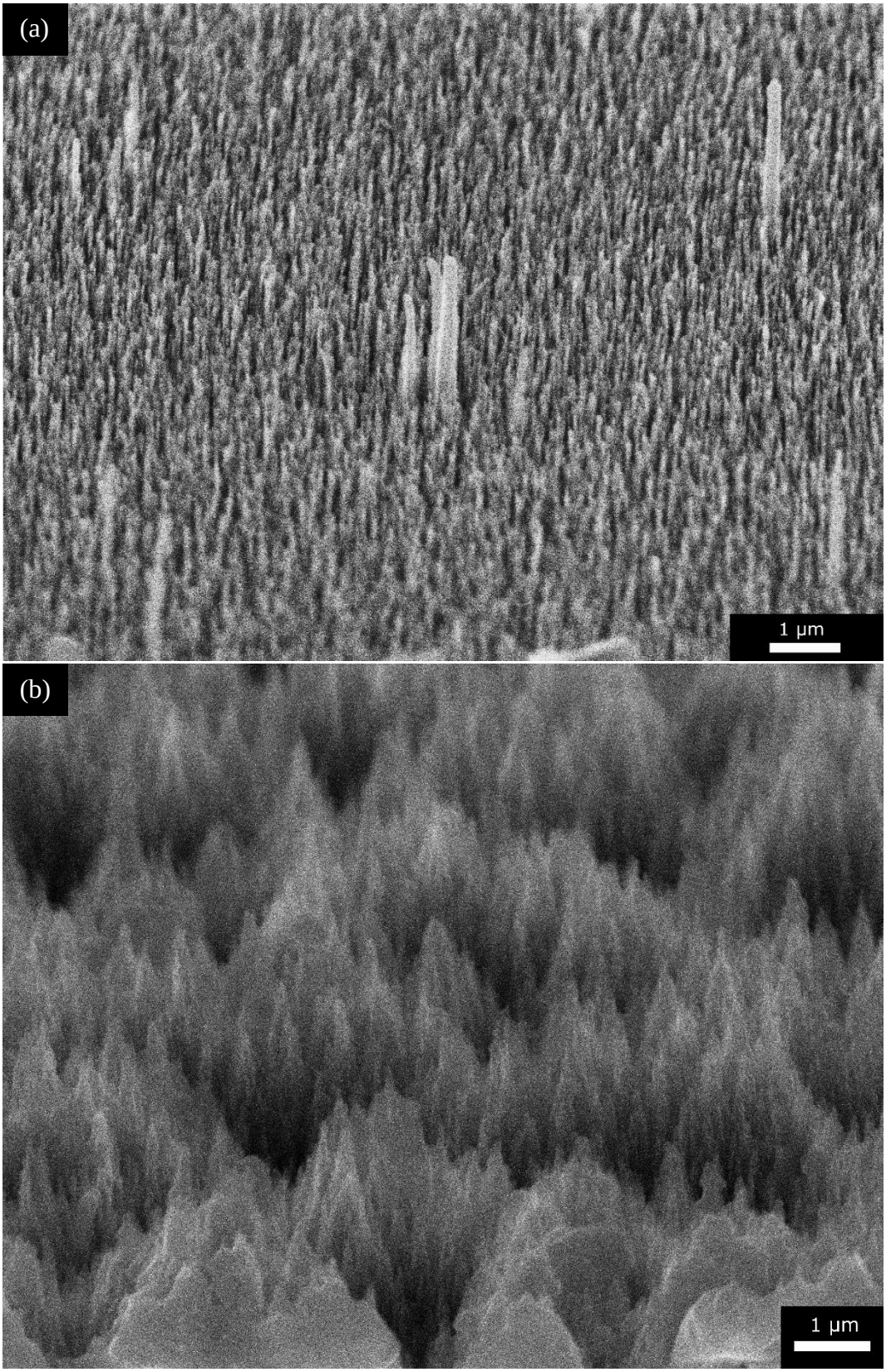

Figure 3.7: SEM images of bSi used for experimental work with S. aureus. (a) uniform needles are ~2.5 µm, with a few taller needles at ~5 µm. (b) pyramidal needles, average 1.3 µm, but with a wide range of heights.

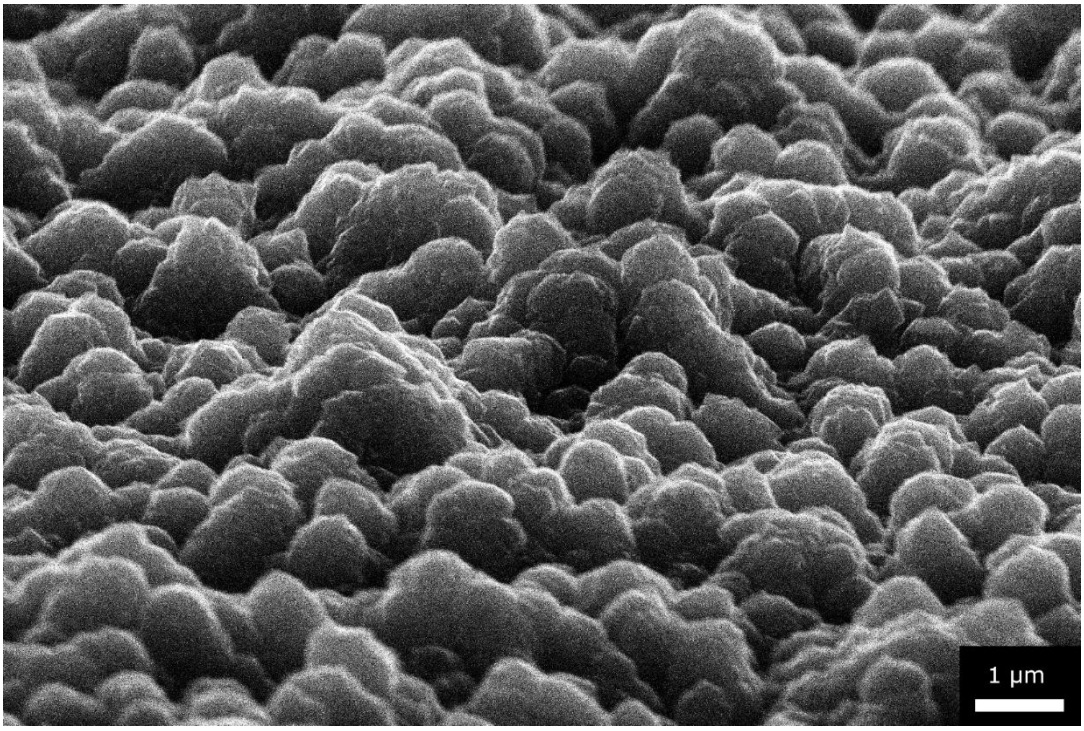

Figure 3.8: SEM image of D-bSi, 60 min growth on the 1.3 µm pyramidal bSi.

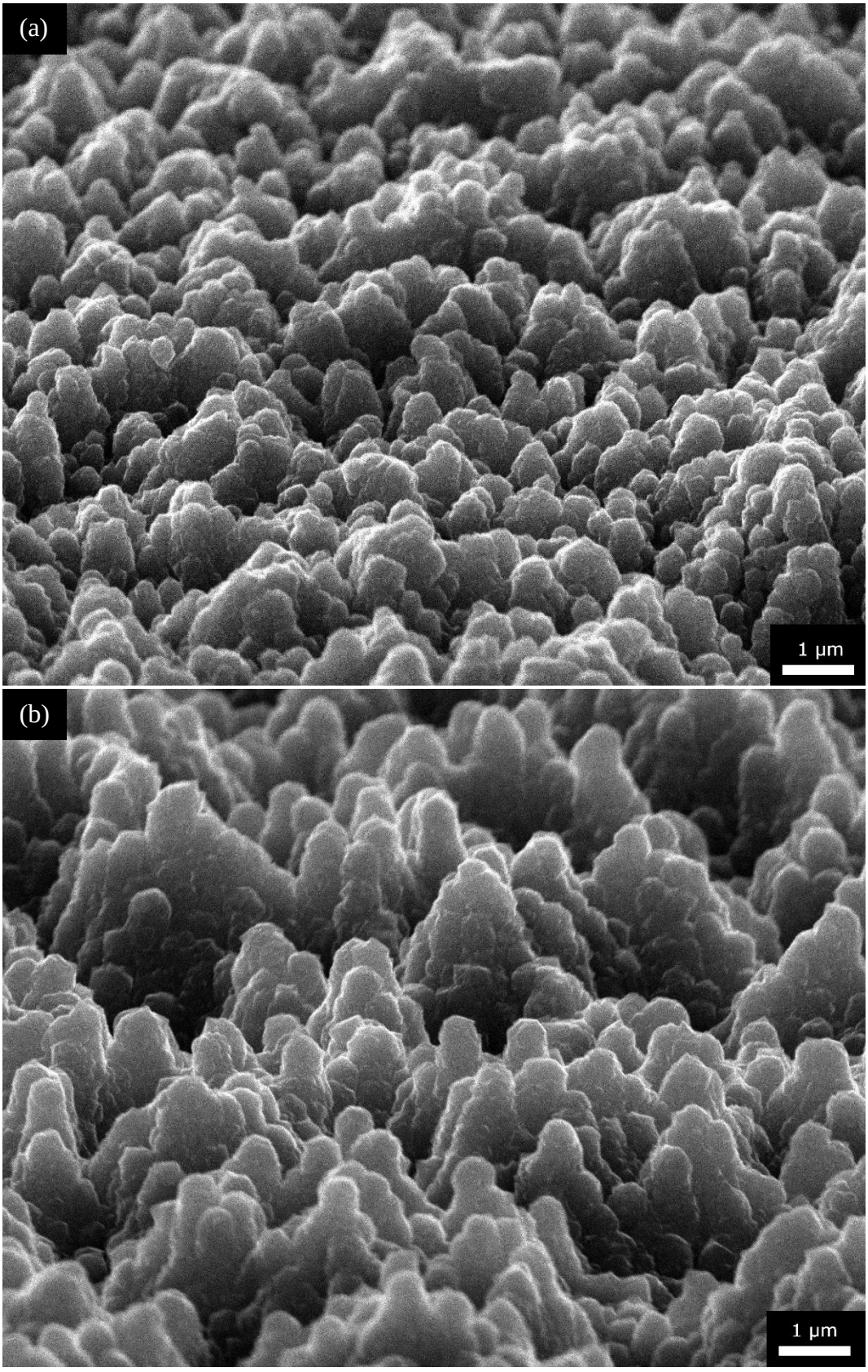

Figure 3.9: SEM images of D-bSi, (a) 30 min and (b) 45 min growth on the 1.3 µm pyramidal bSi.

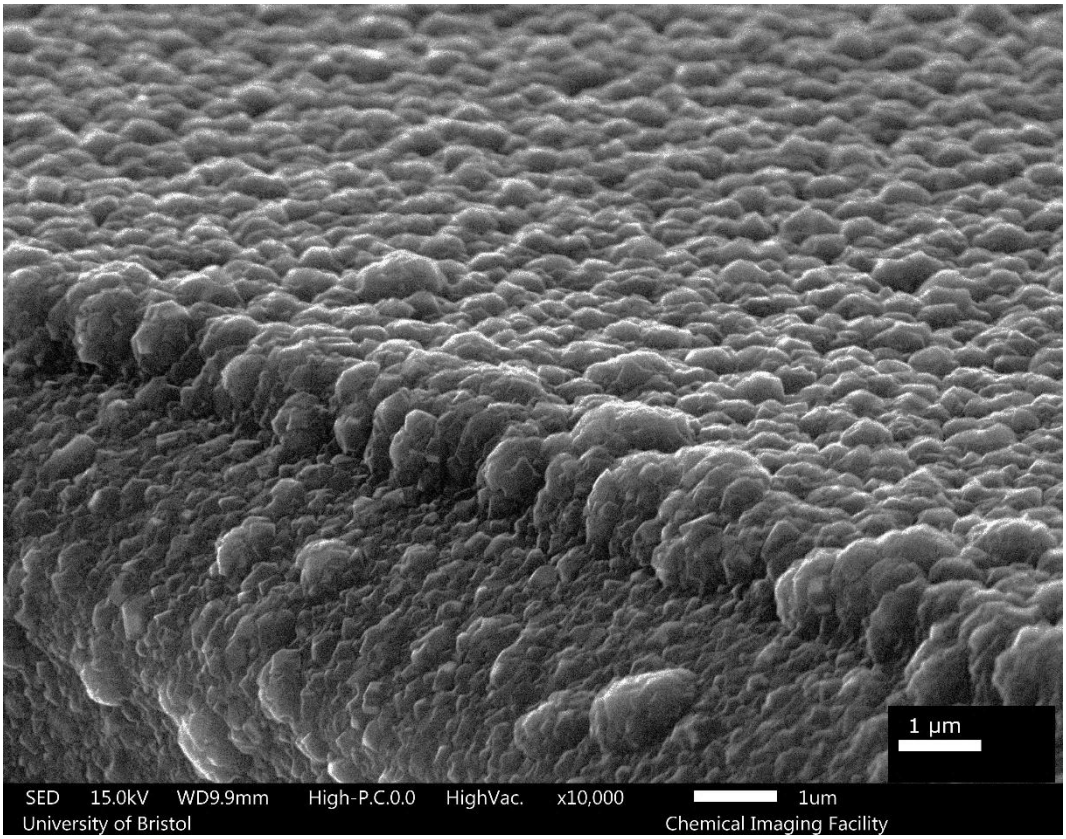

Figure 3.10: SEM image of D-bSi, 60 min diamond growth on the 2.5 µm bSi.

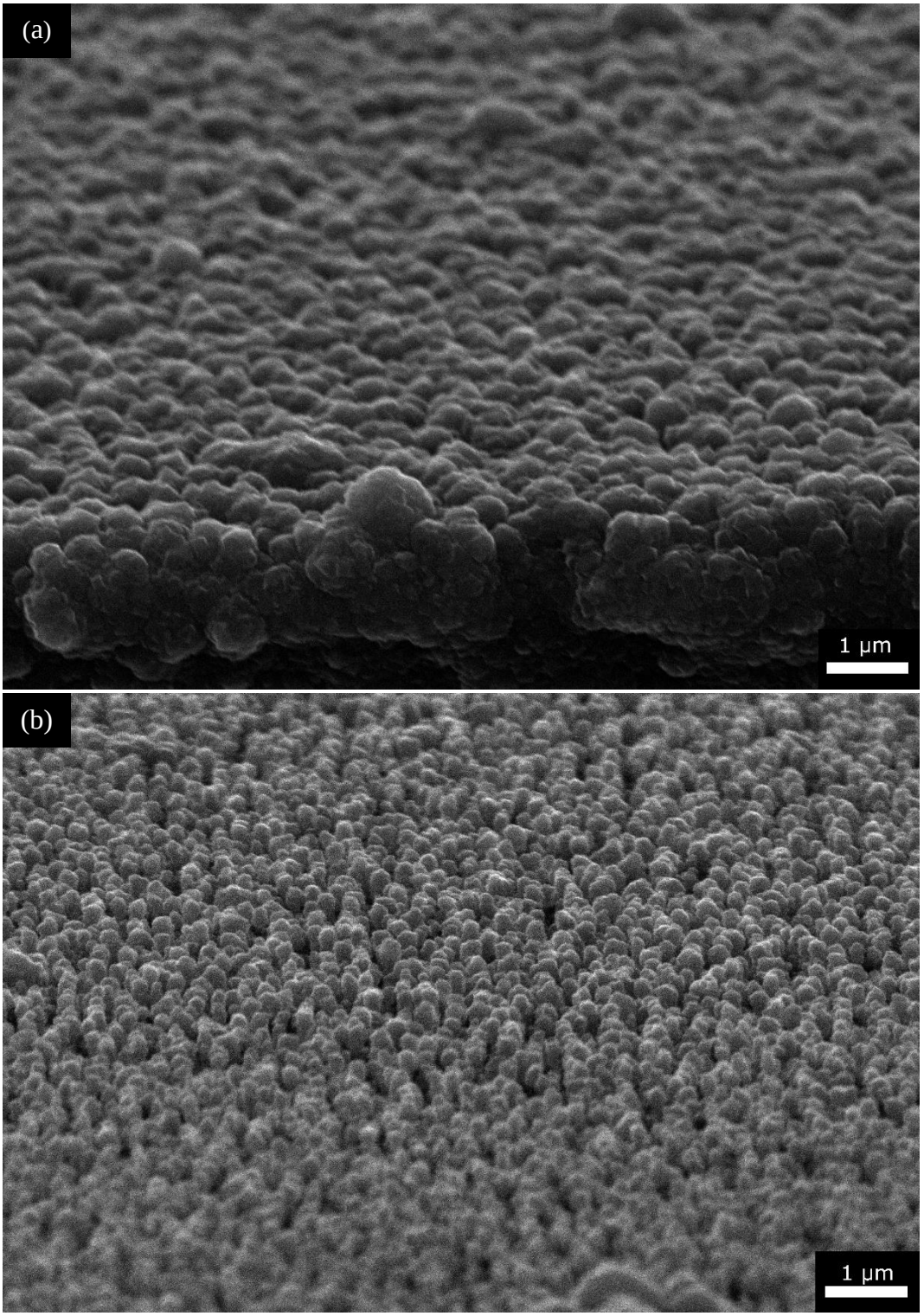

Figure 3.11: SEM images of D-bSi, (a) 40 min, and (b) 20 min diamond growth on the 2.5 µm bSi.

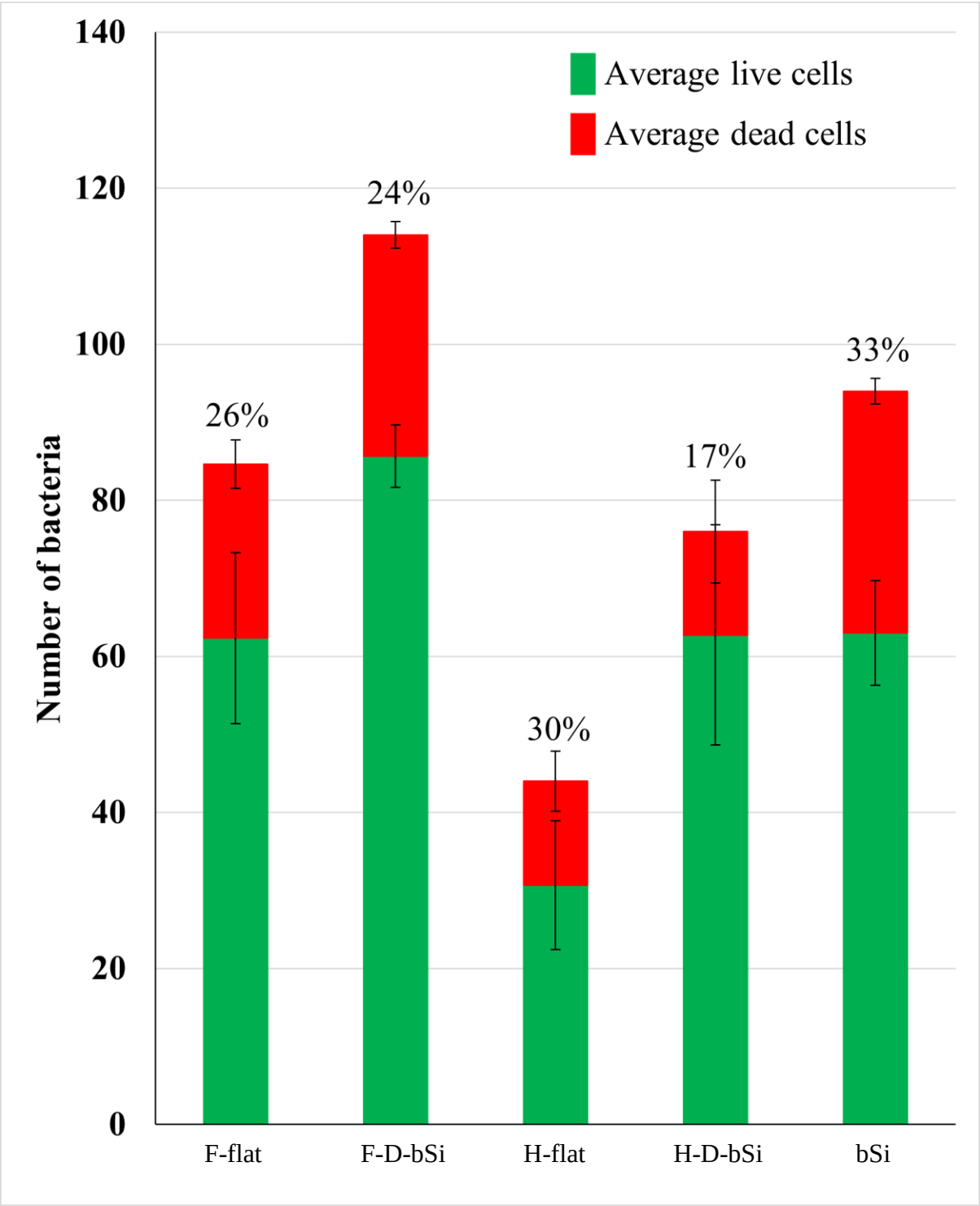

Figure 3.12: *S. aureus* bacterial viability as determined using Live/Dead staining for H- and F- terminations on D-bSi and flat diamond samples, with a bSi control. Total numbers of bacteria adhered to the samples, along with the numbers of living (green) and dead (red) cells indicated. The percentage of dead cells for each sample is indicated and error bars represent one standard deviation of the number of live and dead cells across 3 regions of the samples tested for each termination.

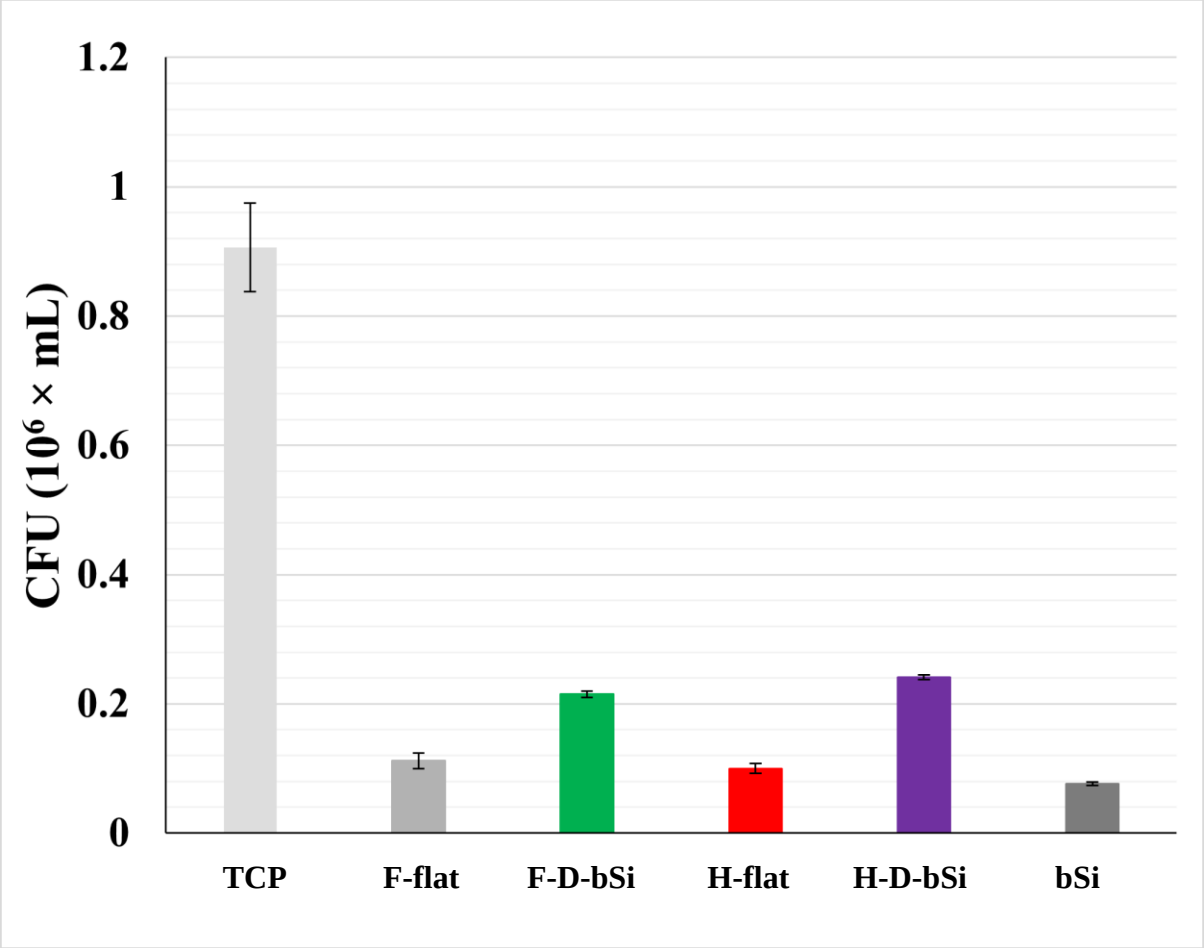

Figure 3.13: *S. aureus* CFU count following 24 h of incubation at 37°C on both H- and F-terminated flat diamond and D-bSi surfaces, as well as bSi and TCP controls for comparison. Data are presented as averages of 32 measurements across each sample, with error bars showing one standard deviation in these data.

3.4.3 Diamond-on-5 µm bSi for Gram-positive *S. aureus* and *S. epidermidis*

With the limited success of the previous experimental set, another set of bSi needles were used for testing; these were ~5 µm long and much thinner tips of ~20 nm, overall giving a needle density of ~10 μm^{-2}, shown in Figure 3.14. Initial attempts to grow following electrospray seeding (Figure 3.15) produced poor coverage of the needles, so an alternative seeding method was utilised, submerging the bSi into a seeding solution for a range of durations and followed by growth for 15 minutes, with the grown samples shown in Figure 3.16. The optimal seeding duration was determined to be 60 minutes, followed by 30 minutes of growth to achieve the thin uniform diamond coating on the needles shown in Figure 3.17.

Fluorine termination was then performed on the D-bSi and flat diamond control samples, and the effect on hydrophobicity was analysed by water contact angle measurements, shown in Table 3.2, with example images shown in Figure 3.18.

The samples were then incubated for 1 hour with the two bacterial species, with the Live/Dead assays presented in Figure 3.19 for *S. aureus* and Figure 3.20 for *S. epidermidis*.

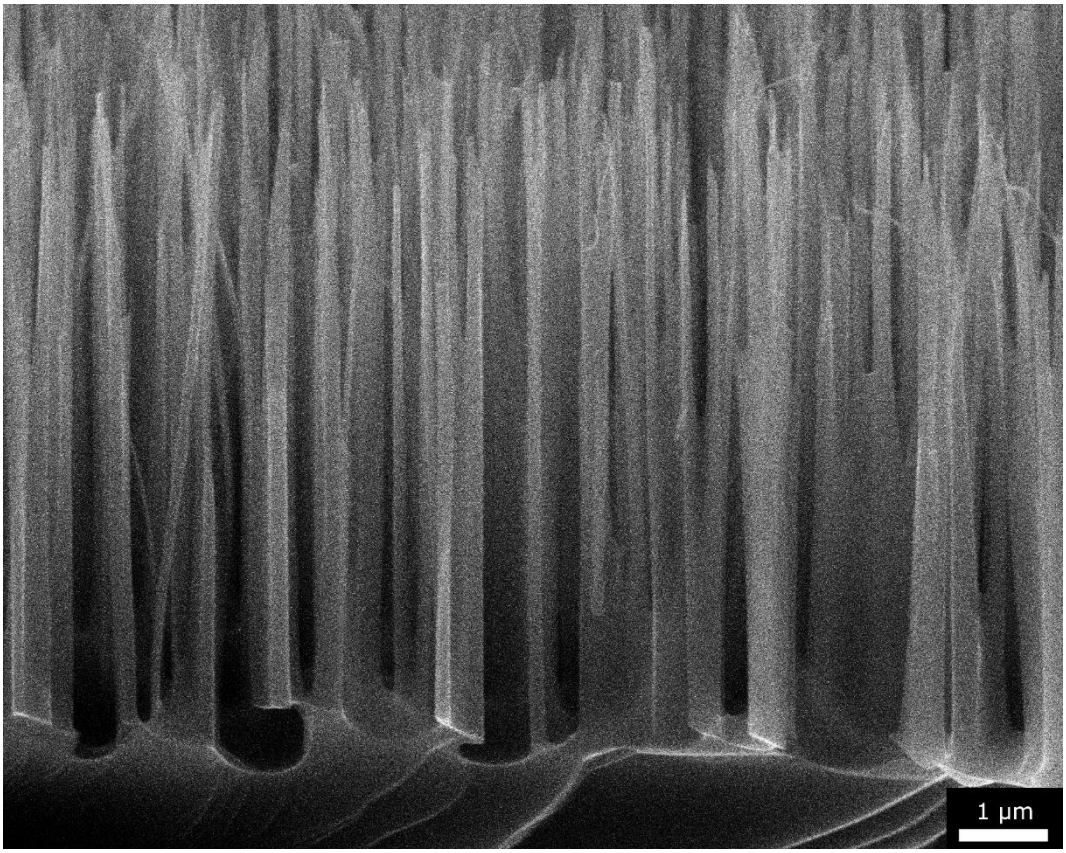

Figure 3.14: SEM image of bSi used for experimental work with *S. aureus* and *S. epidermidis*. Needles are ~5 µm, with tips ~20 nm in diameter.

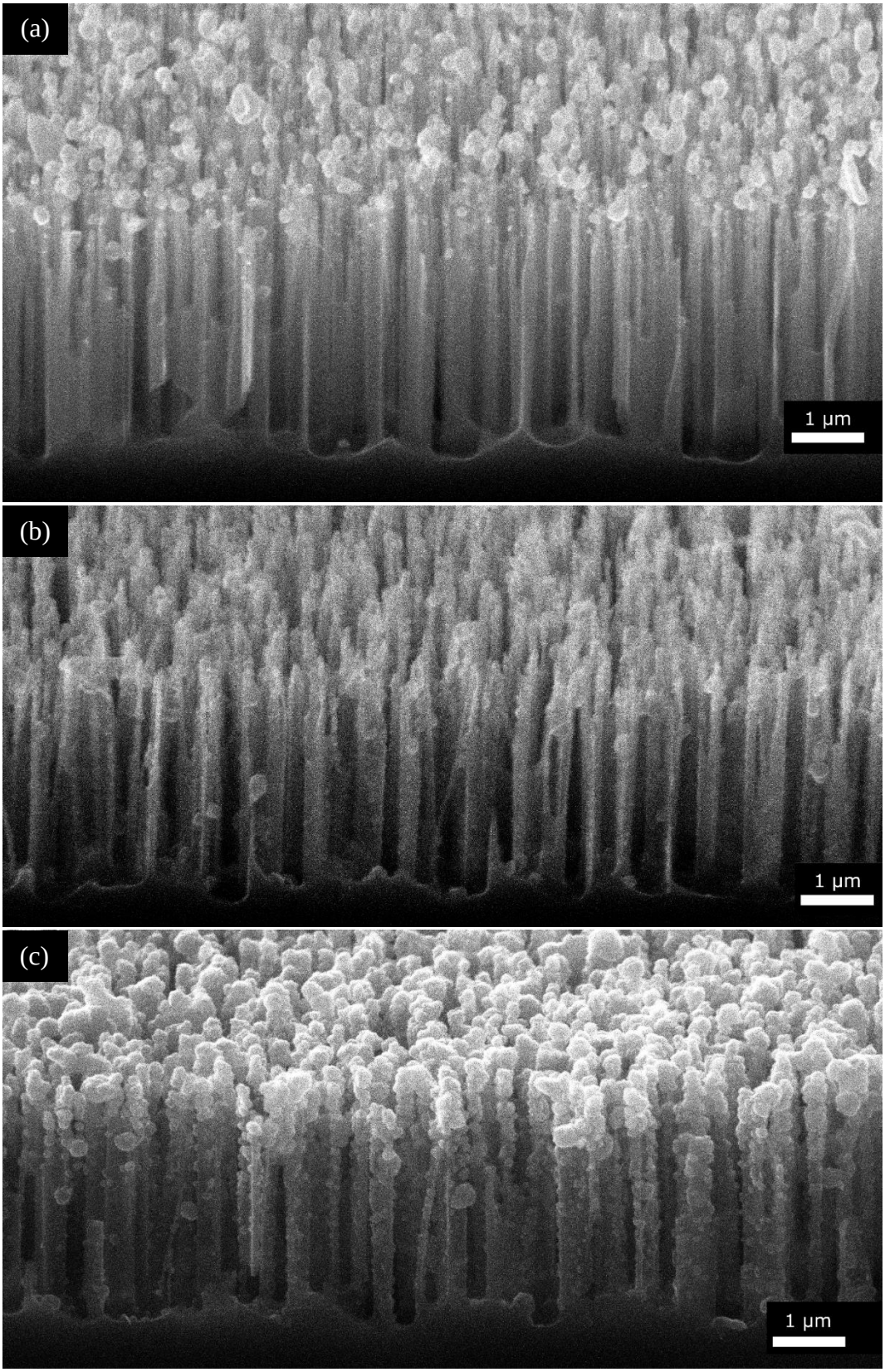

Figure 3.15: SEM images of 5 µm bSi following electrospray seeding and (a) 10, (b) 15, and (c) 20 min of growth.

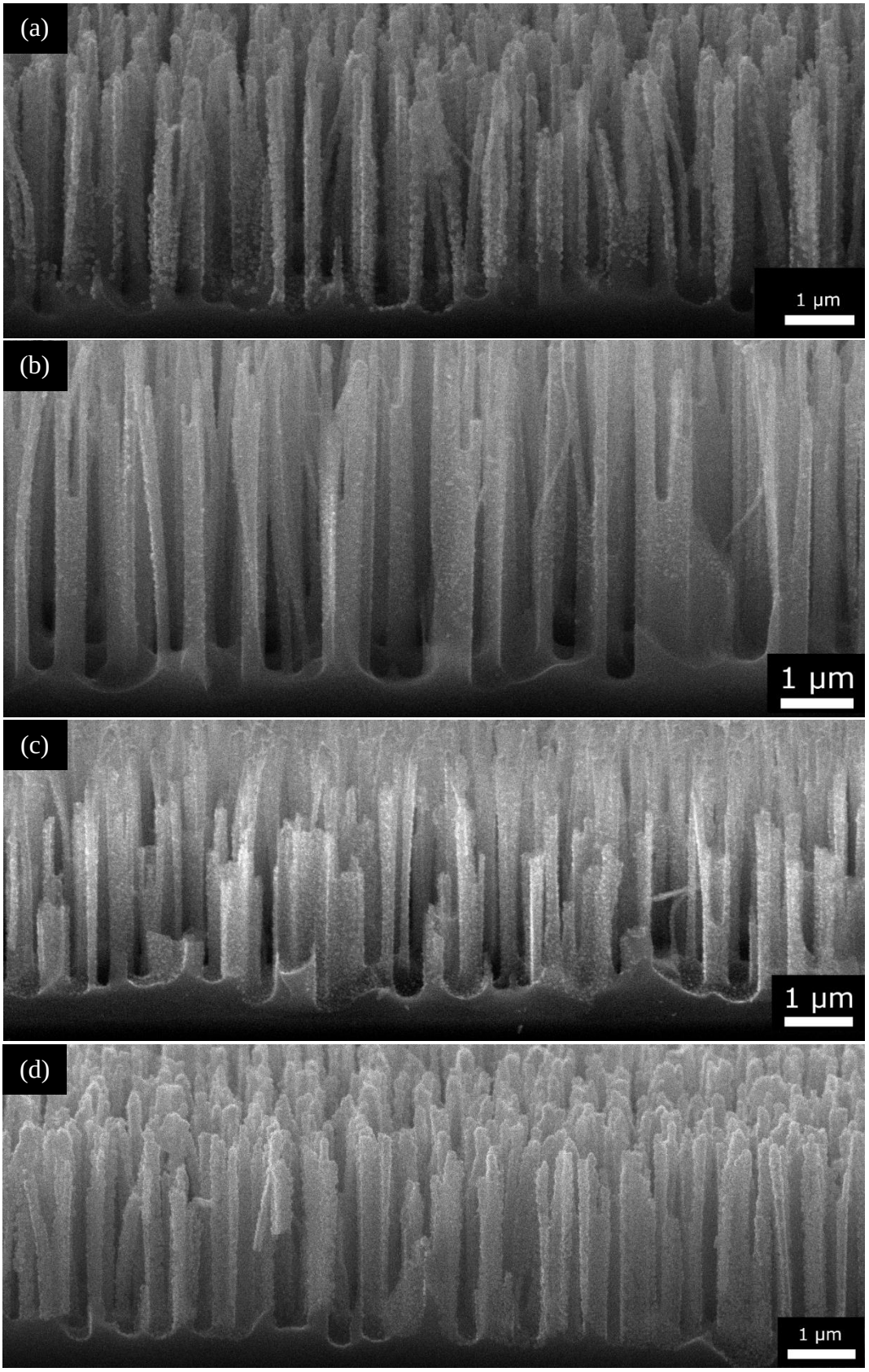

Figure 3.16: SEM images of 5 µm bSi with submersion seeding for (a) 10 s, (b) 1 min, (c) 15 min and (d) 60 min, all followed by 15 min of CVD diamond growth.

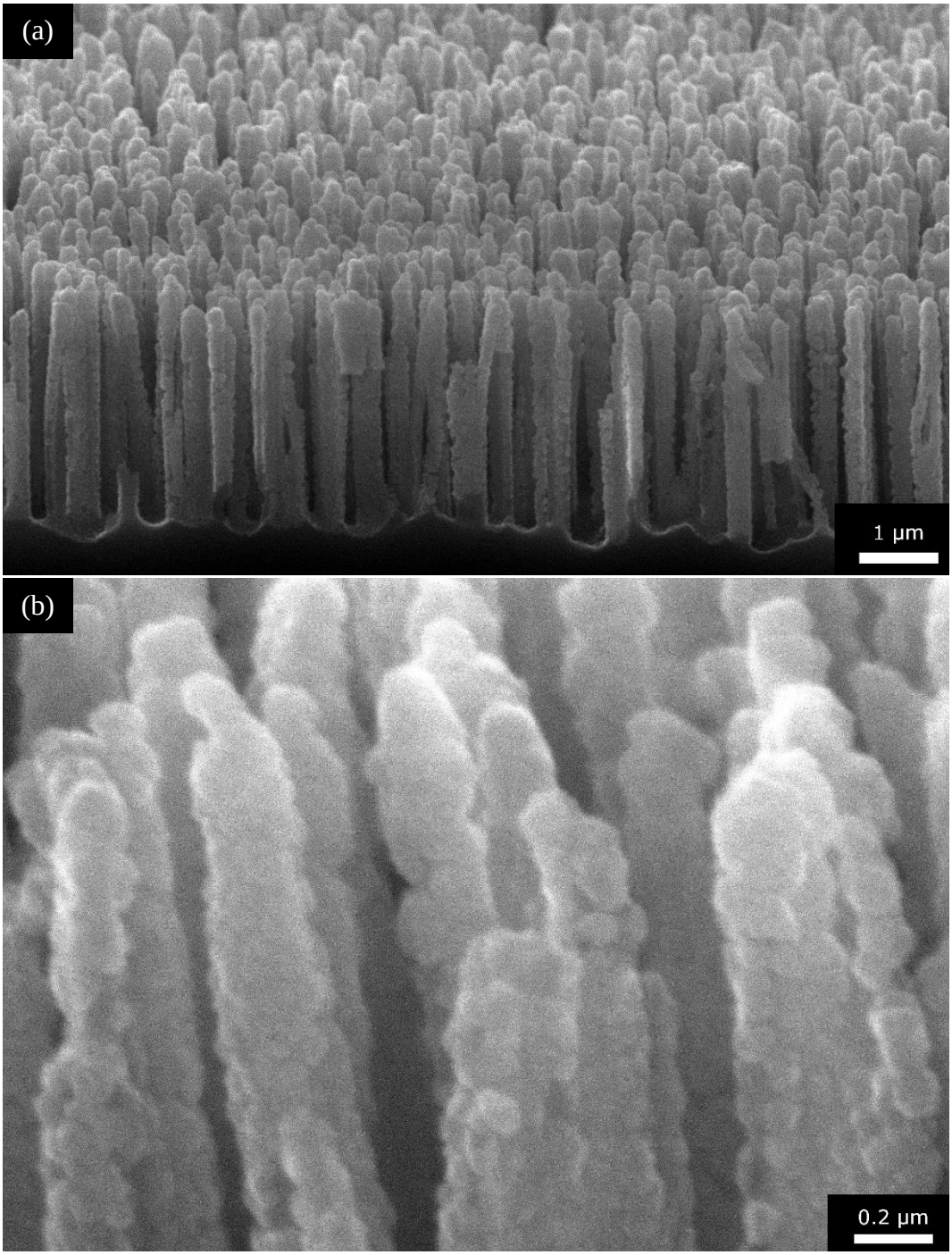

Figure 3.17: SEM images of 5 µm bSi with submersion seeding for 60 min, followed by 30 min of CVD diamond growth. (a) shows the uniform growth along the entire length of the needles. (b) is a higher magnification image of the D-bSi needles, showing the sharpness of the bSi has been retained, and that the D-bSi is without pinholes.

Table 3.2: Water contact angle results for the samples used for *S. aureus* and *S. epidermidis* experiments. Values from surfaces used for *E. coli* included for comparison. *Although the bSi needles were not deliberately terminated, they will likely have a native oxide layer of a few nm thickness.

Sample surface	Termination	Contact angle / °	*E. coli* samples / °
bSi	Not terminated*	84	84
Flat diamond	H	64	64
	F	69	104
D-bSi	H	74	85
	F	131	137

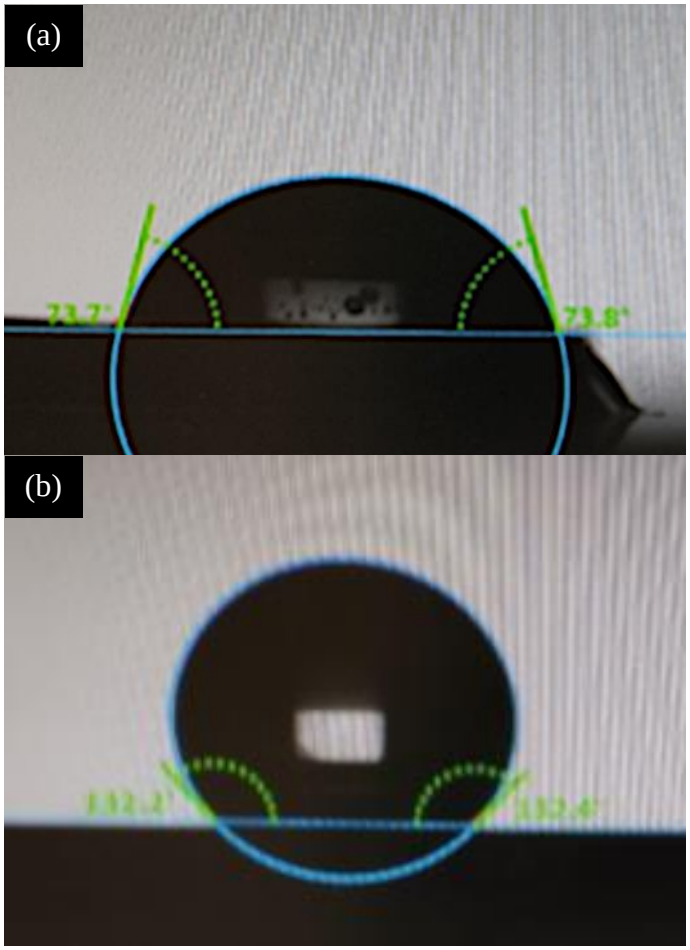

Figure 3.18: Images of the water droplet profiles used to determine contact angles for (a) H-terminated, and (b) F-terminated D-bSi. The angles shown are 73.7 and 73.8° for (a) and 132.2 and 132.4° for (b).

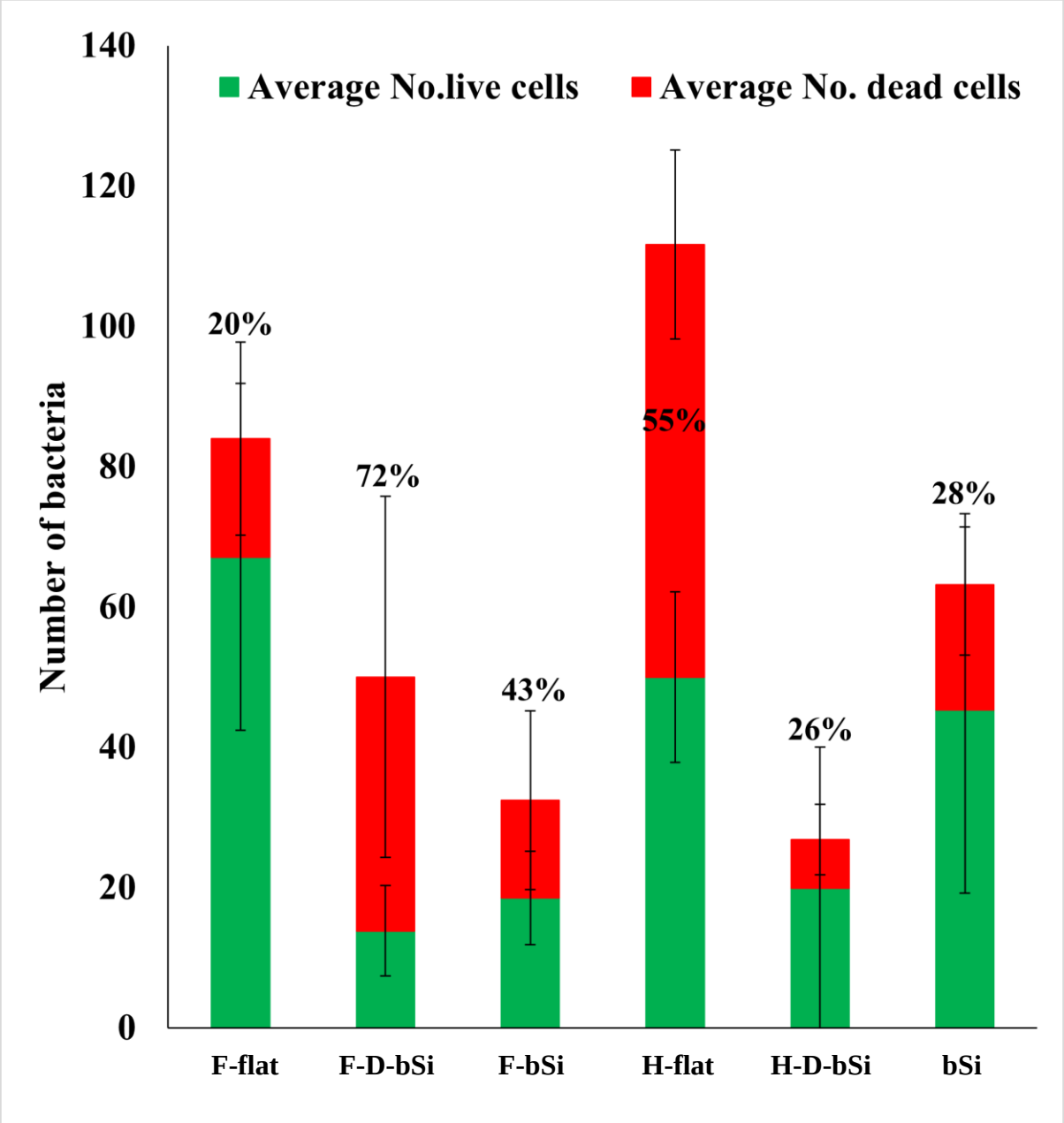

Figure 3.19: *S. aureus* bacterial viability as determined using Live/Dead staining for H- and F- terminations on D-bSi and flat diamond samples, with a bSi control. Total numbers of bacteria adhered to the samples, along with the numbers of living (green) and dead (red) cells indicated. The percentage of dead cells for each sample is indicated and error bars represent one standard deviation of the number of live and dead cells across 3 regions of the samples tested for each termination.

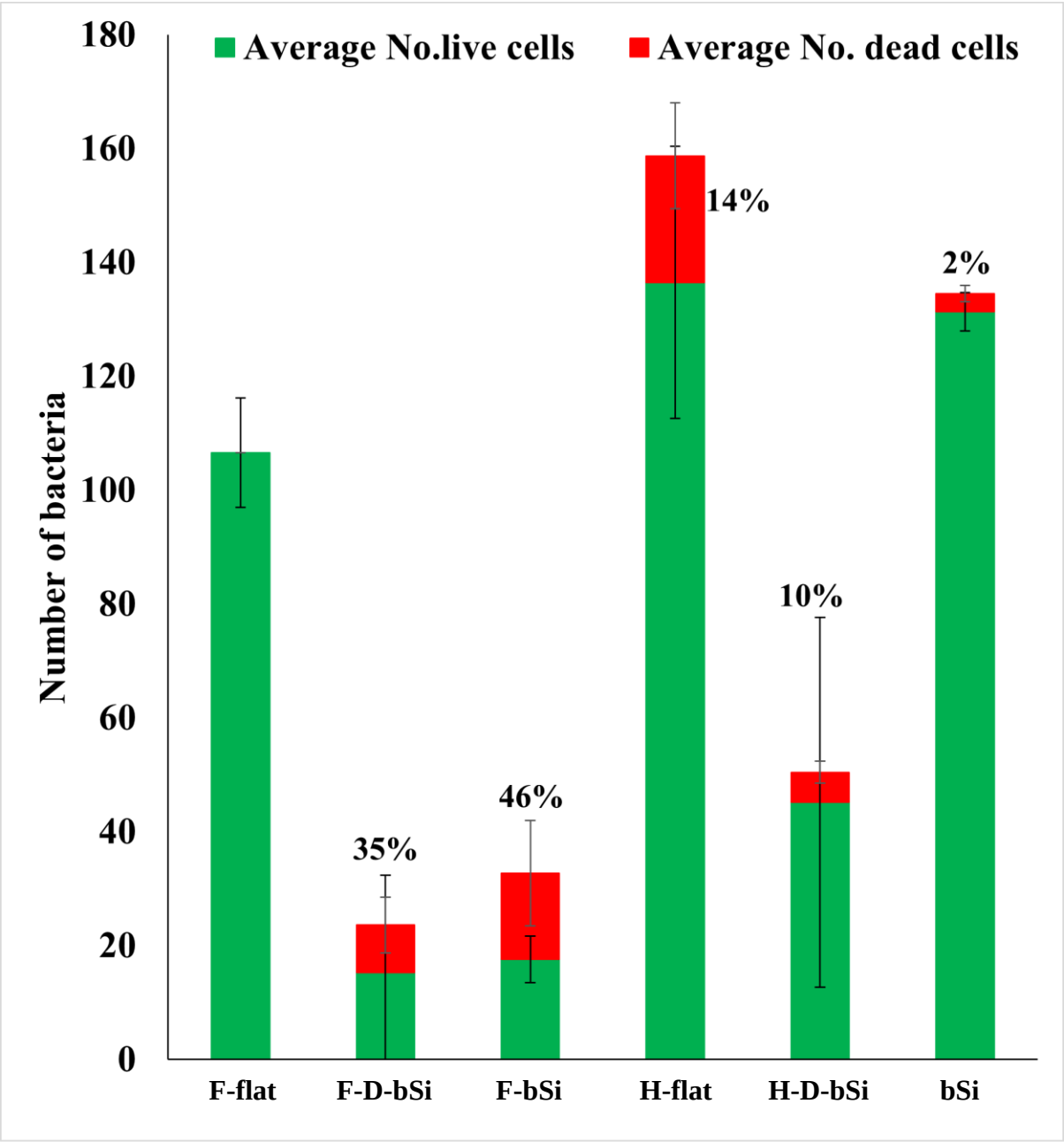

Figure 3.20: *S. epidermidis* bacterial viability as determined using Live/Dead staining for H- and F- terminations on D-bSi and flat diamond samples, with a bSi control. Total numbers of bacteria adhered to the samples, along with the numbers of living (green) and dead (red) cells indicated. The percentage of dead cells for each sample is indicated and error bars represent one standard deviation of the number of live and dead cells across 3 regions of the samples tested for each termination.

3.5 Discussion

3.5.1 Diamond-on-7 µm bSi for Gram-negative *E. coli*

In prior work using Gram-negative bacteria [28], it was found that needles ~2.5 and ~19 µm long were similarly effective at killing bacteria. However, the longer needles had a much lower needle density (1.5 μm^{-2}) compared to the shorter needles (8 μm^{-2}), and it was observed that many bacteria were able to sit between the longer needles. As such, it was determined that needles with an intermediate length would likely be effective, and that a higher needle density may provide increased bactericidal efficacy. Out of the assorted bSi wafers available for use, one wafer looked particularly suitable, shown in Figure 3.4. This wafer had needles up to ~7 µm long, and, although the needle density of the tallest needles was also ~1.5 μm^{-2}, the range in needle heights was analogous to the bimodal needle height distribution seen in dragonfly wings. Accounting for the range of needle heights, needle density was ~3 μm^{-2}.

A single batch of 6 samples was seeded using electrospray to determine if the seeding would be effective for these bSi needles. Initially a diamond growth duration of 60 min was chosen – the duration used in previous work using the same equipment [28] – with three samples grown simultaneously. As shown in Figure 3.5, this duration provided a good, uniform coating of diamond along the entire length of the needles, with all three samples showing the same uniformity, comparable to the coatings used for the previous work. As such this was chosen as the growth duration for the experimental set. Samples were seeded and grown using the conditions stated in Section 3.2 for 60 min. Additional SEM images were obtained from samples across the set to ensure consistency, also shown in Figure 3.5.

However, diamond coating the bSi had two major effects on the topology. Firstly, the diamond coated needles were much thicker, with transmission electron microscopy images showing the original bSi needles were ~30 nm wide, and the diamond-coated needles 10× thicker at ~320 nm. This meant that the needles themselves were much less sharp so any puncturing effects would be diminished – although, with the prevailing theory being that of stretching of the bacterial cell walls, this loss of sharpness was not expected to be a significant detriment to the bactericidal effect of the surface. Secondly, the needles appeared to be shorter than they were before, suggesting some etching of the needles occurred during the growth process. The tallest needles of D-bSi were ~5 µm, down from the ~7 µm of the starting bSi. This was also observed to occur in prior work [28], so again, was not considered to be an issue for the experiment.

Previous work had only explored the use of as-deposited hydrogen-terminated diamond, so the main area of interest for this experimental set was the use of a range of surface terminations. Using the technique and parameters outlined in Section 2.5.2, D-bSi samples were prepared with F-, O- and NH_2-terminations. These surfaces were then assessed using water contact angle – see Section 2.6.3 – which provided a measure of the hydrophobicity/hydrophilicity of the sample surfaces. These data are presented in Table 3.1, and as shown, these values show the same trends as those seen with literature values. Given the significance of surface roughness on water contact angle, the large difference between the flat and the nanostructured samples was expected.

The difference between the experimental values and the literature values can easily be attributed to the experimental "flat" diamond being microcrystalline, while the literature used nanocrystalline diamond. This impact of the surface roughness is clearly reflected in the difference between the flat diamond and D-bSi samples terminated simultaneously.

As expected, the hydrogen-terminated bSi and D-bSi had very similar water contact angles, as the surfaces had similar morphology. The contact angle for the flat samples were less impacted by the change in termination, which was also expected, as the surface roughness meant that the water effectively sat on the diamond film with a low interface area; this was the opposite for the bSi and D-bSi, where the water droplet would be "penetrated" by the needles, so any change in the hydrophilicity impacted a significantly larger interface area than for a flat sample.

For the D-bSi, this resulted in extreme results, with the F-termination causing the water droplet to sit above the surface due to the extremely hydrophobic nature of the termination, whereas the O-termination caused the water to completely spread over the surface. These changes were expected. Hydrogen terminated diamond is somewhat hydrophobic normally, due to the C-H bonds on the surface being poor H-donors and acceptors, and thus not allowing favourable interaction with water [31]. Oxygen termination is known to make diamond hydrophilic due to the significant dipole generated by the C-O bond, which results in dipole-dipole interactions with water, increasing the interaction between them and yielding a hydrophilic surface [32]. C-F bonds are polar, which normally would reduce the surface energy with water and encourage further wetting; however, the C-F bond is only a weak hydrogen-bond acceptor resulting in 'polar hydrophobicity', making fluorinated diamond surfaces very hydrophobic [33].

From the results shown for flat diamond, it was thought there may be limited value to doing further experiments using the ammonia-termination, given the main variable to be explored

was the impact of hydrophobic and hydrophilic terminations on the bactericidal nature of the surface. Due to time constraints, no data were collected for the water contact angle for NH_2-terminated D-bSi as the water droplet analyser was unavailable to do the measurements before the samples needed to be sent for the bacterial experiments.

Using the procedure outlined in 3.2.7, samples were exposed to the *E. coli* bacterial solution and then stained, with the results shown in Figure 3.6. For these data, hydrogen-terminated flat diamond was used as the control, with H-, F-, NH_2- and O-terminated D-bSi used to assess the effect of changing surface termination on the bactericidal efficiency of the surface. The other terminations of the flat diamond were expected to provide much a less significant bactericidal variation, so would only serve to dilute the relevant results and were thus left out of the experimental set.

As shown in Figure 3.6, the D-bSi samples consistently had significantly fewer bacterial cells adhered to them than the flat samples, with a reduction of 40-60% being observed. This alone is an important result, given that fewer adhered cells makes the D-bSi less suited to bacterial growth leading to biofilm formation. This was supported by SEM images which showed more aggregates on the flat samples, likely due to much easier mobility of the bacteria on the unstructured surface.

Increasing hydrophilicity resulted in a slight increase in bacterial adherence, which was expected as these would be more preferential to bacterial cells which commonly survive exposure to aqueous conditions. Similarly, *E. coli* remained viable more often on more hydrophilic surfaces, again expected for the same reasons.

Conversely, the very hydrophobic F-terminated D-bSi surfaces showed two interesting results. Firstly, the adherence of the bacterial cells was similar to that for the less-hydrophobic H-terminated D-bSi, suggesting that the ability of bacteria to adhere to the surface was more complex than simply hydrophobicity. However, given the similar values, no further conclusions regarding this were deemed appropriate. Secondly, the F-terminated D-bSi was much more effective at killing bacteria, with 50% of the cells no longer viable after 1 h of incubation. This is a significant difference, with the H-terminated D-bSi killing 33% and the hydrophilic O- and NH_2-terminations less than half that of the F-terminated, strongly showing that a hydrophobic termination enhanced the bactericidal efficiency of the D-bSi. This was thought to be due to the *fimbriae* being less able to adhere to the surface, reducing the ability of the bacterial cell to anchor to the material.

3.5.2 Diamond-on-1.3 µm bSi pyramids and 2.5 µm needles for Gram-positive *S. aureus*

Given that Gram-positive bacteria are usually smaller and have less rigid cell walls, different bSi batches were chosen for bacterial testing with *S. aureus*, both shown in Figure 3.7. The first batch, shown in Figure 3.7 (a), had shorter needles of ~2.5 µm but with a higher needle density of ~3 μm^{-2} of uniform height needles. The shorter needles were considered sufficient, especially as the cells were ~1 µm diameter spheres, *i.e.* much smaller than those of *E. coli*. From the results found for *E. coli*, the cells sat on the top of the needles, with comparatively little penetration of the needle required for the cell walls to rupture, so these ~2.5 µm needles were thought to be long enough, with a higher density to allow for a similar number of needles to be in contact with the smaller cells. The second batch was chosen due to its very different morphology, with the surface being more pyramidal than the previously used needles, shown in Figure 3.7 (b). These peaks were of a range of heights, on average 1.3 µm, so were smaller but provided a similar height variation as those used for *E. coli* These samples resemble the patterning observed on the natural bactericidal surfaces that the bSi needles were being used to emulate.

1.3 µm pyramidal samples were seeded by electrospray prior to diamond growth in the HF CVD reactor. A starting duration of 60 min was chosen as this is what was used in the prior work on the longer needles, but as overgrowth was expected to occur on the much smaller pyramidal structures, shorter durations of both 30 and 45 min were also carried out. The resultant growths are shown in Figures 3.8 and 3.9. The 60-min deposition led to overgrowth, with the surface losing all sharpness and resembling a film of larger diamond crystals scattered across a flat surface; whereas both the 30- and 45-min deposition provided a sufficient thickness to give a uniform coating while retaining some of the initial surface structures.

However, further assessment of the samples suggested the surfaces would be unsuitable for use with Gram-positive *S. aureus*, given that the cells of ~1 µm diameter would be able to find gaps in the lower-needle-density surface of this batch. With a bacterium only resting on a small number (1-3) of needles, there would be insufficient stretching of the cell wall to result in rupturing, so these would be unlikely to be effective as bactericidal surfaces. Additionally, the jagged peaks of the bSi lost all definition following the diamond growth, leaving just a broad peak which would be less effective than a sharper one according to the cell wall rupturing model.

Diamond growth was performed on the 2.5 µm needles following electrospray seeding. From the results found for the 1.3 µm pyramidal bSi, it was determined to do growth for 20, 40 and 60 min. This choice was made on the basis that 20 min deposition was expected to provide a sufficiently thin coating, but may have been too thin, and as such, not be a uniform coating. 40 min deposition was expected to be optimal. As shown in Figure 3.10, the 60 min deposition was completely overgrown as expected, with the SEM image showing no surface structuring at all beyond the surface roughness of a microcrystalline diamond film. Comparing this image to those in Figure 3.5 highlights the significant difference in the size of the bSi needles.

Figure 3.11 shows both the 40- and 20-min growth samples. The 40-min growth showed similar overgrowth to that after 60 min, with only slight surface deviations showing the gaps between "needles". However, the 20-min diamond growth provided a thin coating over the needles with clear spacing between the tips, and without the needles themselves having become completely rounded. As such, 20-min D-bSi was selected for bacterial testing.

Given the previous results, it was determined that samples of only H- and F-termination would be used for bactericidal testing. These terminations were chosen because F-termination produced the highest bactericidal effect for the Gram-negative bacteria, and H-termination is the natural termination at the end of diamond growth. Terminations were carried out as outlined in Section 2.5.2.

Rather than the noticeable differences observed for water contact angle observed for the previous experimental set, most of these samples completely wetted when the water droplet was added, meaning that no contact angles could be determined. This may have been due to the needle distribution and size in combination with the surface termination interfering with the water surface tension resulting in the droplet losing shape. Both H- and F-terminated bSi as well as the F-terminated D-bSi displayed this behaviour. Only the H-terminated D-bSi produced a water droplet which sat on the surface, giving a contact angle of 81°, which is similar to the angle observed for previous H-terminated D-bSi. Additionally given the much smaller needle tip size of the bSi compared to the D-bSi, this may account for why the bSi samples wetted, as the water droplet effectively sank into the nanostructured surface.

Yet both flat Si and diamond samples which were terminated simultaneously were also tested for water contact angle and produced similar values to those obtained previously. This suggested that there was no fault in the termination method, so unfortunately there was a lack of conclusive water contact angle data for these samples.

The samples were sent to our collaborators in UCMG for bactericidal testing. There, samples were exposed to *S. aureus* as described in Section 3.2.7 and the results for the Live/Dead assay are shown in Figure 3.12. From these results, the foremost conclusion is that the D-bSi was consistently less effective as a bactericidal surface than both flat diamond of the same termination and bSi. While this outcome was not anticipated given the efficacy of D-bSi against Gram-negative *E. coli*, Gram-positive *S. aureus* is much smaller and has a very different cell wall. With the bSi sample producing a higher proportion of dead cells than any of the other samples, the mechanism of cell wall rupturing may still be occurring, but only because of the much sharper bSi needles, with the D-bSi needles being too rounded for the cell walls to be penetrated. The previously observed trend of fluorine termination improving bactericidal efficacy was maintained for the D-bSi, with the F-terminated D-bSi sample being significantly more effective.

Also of note is that the D-bSi had higher cell adherence than their respective flat diamond samples, which is contrary to what was observed for the *E. coli*. This is likely due to the very different anchoring mechanism used by *S. aureus*, which produces a biofilm as a means of anchoring the bacterial colony; *E. coli* anchors using *fimbriae*, and as such prefers flatter surfaces. For both the flat diamond and D-bSi sets, the fluorine-terminated samples had a higher number of bacteria adhered than the equivalent hydrogen-terminated surface. This may be due to C-F bonds being more polar than C-H, which results in stronger interactions with the proteins at the surface of Gram-positive bacteria.

However, these results were considered to be inconclusive due to limitations in the testing. Due to some D-bSi and bSi samples being damaged in transit, the *S. aureus* being difficult to remove from the flat diamond samples, and time constraints on the collaborators doing the bacterial testing, bacteria were only cultured on one sample of each condition. As such, rather than the data being based on the intended 3-6 samples per condition (with the flat samples being cleaned between growths instead), the data sets were only based on 3 regions of one sample, greatly increasing the impact of any statistical error.

These samples were also tested to assess the viability of biofilms after incubation, along with a tissue culture plastic (TCP) control sample. The results are shown in Figure 3.13, and present similar results to those for the Live/Dead assay, with one notable exception: the bSi sample. The bSi sample has a high adherence in the live/dead assay, but with a high proportion of dead bacteria, significantly fewer CFUs were cultured over the longer duration than, for example the

H-D-bSi sample which had a similar number of living bacteria after the staining. As such, it is apparent that this bSi sample was effective as a bactericidal surface, both killing a large portion of bacteria on the surface and impeding the ability of bacteria to proliferate. Conversely, this D-bSi sample was shown to be an ineffective bactericidal surface in comparison to both the preceding bSi and to microcrystalline diamond. Unsurprisingly, all the surfaces cultured fewer colony-forming units than the TCP, which is a material designed to enable culturing. The TCP control ensured the bacteria were proliferating as expected when on non-bactericidal surfaces.

From these results, it was determined that this batch of bSi was not suitable for bactericidal D-bSi growth as the needles were too rounded, causing the smaller Gram-positive *S. aureus* to not rupture as occurred on the Gram-negative *E. coli*. As such, another batch of bSi was chosen for further experiments.

3.5.3 Diamond-on-5 µm bSi for Gram-positive *S. aureus* and *S. epidermidis*

Given the prior success of bSi but failure of D-bSi to act as an effective bactericidal surface for *S. aureus*, it was determined that a similar set of bSi should be used for further experimental work. The needle length and densities were clearly effective on the bSi, so the primary focus of this set of experiments would be to grow a thinner coating of diamond so the D-bSi could better retain the sharpness of the bSi, and hopefully be more effective at puncturing the cell walls as a result.

As such, it was determined to use a set of bSi wafers provided by LAM Technologies. This bSi had needles ~5 µm long, with needle tips 0.25-0.5 µm apart and tip radius of ~20 nm, shown in Figure 3.14.

Initial growth attempts followed on from previous work, utilising the electrospray seeding method. As thinner diamond growth layers were the goal, these first depositions were performed for 10, 15 and 20 min, producing the coatings shown in Figure 3.15. As can be seen, the diamond coating on these samples was not uniform over the length of the needles, with the 20 min showing clearly good coverage at the top of the needles but only a few crystals further down. This lack of crystal distribution suggested that the electrospray seeding method may not be compatible with this bSi batch, containing both high density *and* long needles.

As such, two options were explored. The first was to vary the parameters used for the electrospray technique, but these changes provided minimal impact to the coverage of the seeding.

The other option explored was to develop an alternative seeding technique based on submerging the bSi samples into the same detonation nanodiamond seeding solution used for the electrospray (~3 nm DND, 10 drops of 1 wt% in water, suspended in 30 mL of methanol).

In order to determine an optimal seeding time, 4 samples were made with seeding duration of 10 s, 1 min, 15 min and 60 min, followed by 15 min of diamond deposition in the HF CVD reactor. This range was chosen with the lower extreme of the minimum duration feasible to be carried out consistently and the upper as a duration considered to be possibly excessive. Similarly, the growth duration was chosen based on the previous results, where 15 min allowed for a thin coating, retaining as much of the structure of the bSi needles as possible.

Figure 3.16 shows the resultant diamond coatings of the bSi samples. The shorter seeding durations produce better coverage than the electrospray, but still are not quite able to give full coverage. Given the relative similarity in coverage between the 15- and 60-min samples, and the simplicity of the seeding technique, it was determined to use to the 60-min submersion seeding technique for the samples to be grown for bactericidal testing. However, upon repeating the 60-min seeding with 15 min growth, the thickness of the diamond coating was observed to be too thin, resulting in pinholes in the diamond films.

As such, the samples used for bactericidal tests were grown for 30 min, as this reliably produced a thin diamond film, retaining the underlying structure of the bSi well, as shown in Figure 3.17. The higher-magnification SEM image shows the quality of the diamond, with discrete crystals of diamond fully covering the needles without any gaps. The initial sharpness of the bSi of ~20 nm has been reduced, but by a much lesser extent than for previous D-bSi samples used for bacterial testing.

Fluorine termination was carried out as before and the results are shown in Table 3.2. The water contact angle increased from 74° for the H-D-bSi to 131° for the F-D-bSi, showing approximately the same change in hydrophobicity as was observed for the bSi used with *E. coli*. For the flat diamond samples, there was only a small increase in hydrophobicity from 64° to 69° following fluorination. Figure 3.18 shows the visible difference between the water contact angle between the H- and F-terminated D-bSi samples.

These samples were sent to our collaborators UMCG for bactericidal testing. Live/Dead assay was performed using *S. aureus* following 1 h of incubation, shown in Figure 3.19, and using *S. epidermidis* after 1 h of incubation, shown in Figure 3.20. Unlike with previous experiments with *S. aureus*, where the flat samples had less bacteria adhered to the surface than the nanostructured ones for a given termination, for this set of experiments, the flat samples had more bacteria adhered. This suggests that the D-bSi surface was significantly less suitable for bacterial growth than the previous D-bSi samples.

For both bacteria, the flat samples had a higher mortality rate when hydrogen terminated than when fluorine terminated. Conversely, for both bacteria, fluorination significantly increased the bactericidal efficacy of the D-bSi compared to hydrogen-termination. This is most prominent for *S. aureus*, where the fluorine terminated D-bSi was able to kill over 70% of the adhered bacteria. *S. epidermidis* generally adhered less to the nanostructured surfaces, particularly when the surface was F-terminated.

As previously mentioned, hydrophobic surfaces are often harder for bacteria which are used to more aqueous environments to adhere to, which these results support. Similarly, the conclusion of F-termination enhancing the bactericidal efficacy of previous work is also supported by these data.

3.6 Summary and conclusions

Utilising bSi with a varying height up to 7 μm and needle density of ~3 μm^{-2}, diamond films were grown to make a surface that was effective at killing *E. coli*. Notably, the cells were less able to aggregate, which in turn reduced their potential to form biofilms, on the D-bSi samples compared to the flat diamond control samples. While the mechanism of cell rupture was prevalent, there was an observed increase on biocidal activity with increased hydrophobicity of the surface. Being a Gram-negative bacterium, *E. coli* had a more flexible cell wall, and thus was more considered more prone to the cell wall rupture mechanism.

Subsequently, *S. aureus* was chosen to explore the biocidal ability of bSi and D-bSi on a Gram-positive bacterium with a harder cell wall. When using shorter (~2.5 μm) needles with a similar needle density as before, the nanostructured surfaces proved ineffective, with both higher adhesion and higher survival rates of the bacteria on the flat control samples compared to the bSi and D-bSi samples. However, when using more closely packed needles (~10 μm^{-2}), *S. aureus* was successfully killed by the D-bSi surfaces, with the hydrophobic fluorinated surfaces proving particularly effective. The benefits of the hydrophobic surface were also seen when using another Gram-positive bacterium – *S. epidermidis* – which had much lower adherence of the bacteria after incubation compared to the more hydrophilic surfaces.

Overall, D-bSi was successfully grown and proven for its bactericidal properties for a number of bacteria. Fluorination generally enhanced the ability of D-bSi to kill surface bacteria, although this required suitable D-bSi for the effect to be observed.

Gram-negative *E. coli* and both Gram-positive *S. aureus* and *S. epidermidis* showed significant mortality on D-bSi surfaces, although the length of the needles, the spacing of the needles and the sharpness were all variables that affected the efficacy of the D-bSi. As such, D-bSi which was suitable as a bactericidal surface for Gram-negative bacteria was not found to be effective for Gram-positive bacteria. As a result, any bactericidal surface may require a mixture of needle lengths and densities to be effective against all bacteria – and potentially this would be of interest to explore further.

However, D-bSi and bSi are both very fragile, potentially limiting use in some real-world setting where these surfaces could be damaged. These studies will hopefully provide a start for nanostructured and suitably terminated surfaces to be fabricated from more viable antibacterial materials, which could lead to commercial production.

3.7 Future work

One of the areas of future work would be a further investigation into the longer-term effect of the bSi and D-bSi surfaces. The samples in this work were mostly only incubated for a short duration, and one significant difference between flat and nanostructured surfaces is in how mobile dead bacteria are. Once ruptured, the dead bacteria are pierced by the bSi/D-bSi, which may make that area no longer able to kill bacteria effectively. A study of bacterial growth over longer duration to observe the growth of bacteria on these surfaces would enable greater understanding of whether these surfaces continue to function effectively over time, and what cleaning procedures would prove effective to maintain the biocidal activity of the surface.

Another would be a using the 5 µm bSi samples to compare the biocidal efficacy for Gram-negative bacteria, as it proved effective at killing Gram-positive bacteria. By doing this, it could be shown that these surfaces are not limited to being effective against only a small number of bacteria, which presently limits the scope of their application.

References

1 Dunseath, O., Smith, E. J. W., Al-Jeda, T. et al. *Sci. Rep.*, 9 (2019), 8815.

2 Dunseath, O. *The effect of CVD diamond growth and subsequent surface termination on the bactericidal activity of black silicon*. MSci. Thesis, University of Bristol, Bristol, UK, 2019.

3 McGrath, J. *Using nanostructured diamond surfaces to control bacterial adhesion and growth*. MSci. Thesis, University of Bristol, Bristol, UK, 2020.

4 Donnelly, V. M. and Kornbilt, A. *J. Vac. Sci. Technol. A*, 31 (2013), 050825.

5 Jansen, H. V., de Boer, M. J., Unnikrishnan, S., Louwerse, M. C., and Elwenspoek, M. C. *J. Micromech. Microeng.*, 19 (2009), 033001.

6 Rangelow, I. W. *J. Vac. Sci. Technol. A.*, 21 (2003), 1551.

7 Oh, J., Yuan, H. C., and Branz, H. M. *Nat. Nanotechnol.*, 7 (2012), 743.

8 Kim, W., Ng, J. K., Kunitake, M. E., Conklin, B. R., and Yang, J. *J. Am. Chem. Soc.*, 129 (2007), 7228.

9 Stephens, R. and Cody, G. *Thin Solid Films*, 45 (1977), 19.

10 May, P. W., Clegg, M., Silva, T. A. et al. *J. Mater. Chem. B*, 4 (2016), 5737.

11 Hasan, J., Webb, H. K., Truong, V. K. et al. *Appl. Microbiol. Biotechnol.*, 97 (2013), 9257.

12 Ivanova, E. P., Hasan, J., Webb, H. K. et al. *Nat. Commun.*, 4 (2013), 2838.

13 Stanton, T. B. *Trends Microbiol.*, 21 (2013), 111.

14 Williams, I., Venables, W. A., Lloyd, D., Paul, F., and Critchley, I. *Microbiology*, 143 (1997), 2407.

15 Veerachamy, S., Yarlagadda, T., Manivasagam, G., and Yarlagadda, P. K. D. V. *Proc. Inst. Mech. Eng., Part H*, 228 (2014), 1083.

16 Dunne, W. M. *Clin. Microbiol. Rev.*, 15 (2002), 155.

17 Baker, S., Griffiths, C., and Nicklin, J. *Microbiology*. Taylor & Francis, Oxford, UK, 2011.

18 Connell, I., Agace, W., Klemm, P., Schembri, M., Mărild, S., and Svanborg, C. *Proc. Natl. Acadm. Sci. USA*, 93 (1996), 9827.

19 Umeda, A., Ueki, Y., and Amako, K. *J. Bacteriol.*, 169 (1987), 2482.

20 Neopane, P., Nepal, H. P., Shrestha, R., Uehara, O., and Abiko, Y. *Int. J. Gen. Med.*, 11 (2018), 25.

21 Banerjee, I., Pangule, R. C., and Kane, R. S. *Adv. Mater.*, 23 (2011), 690.

22 Barthlott, W. and Neinhuis, C. *Planta*, 202 (1997), 1.

23 Marmur, A. *Biofouling*, 22 (2006), 107.

24 Maximous, N., Nakhla, G., and Wan, W. *J. Membrane Sci.*, 339 (2009), 93.

25 Green, D. W., Lee, K. K.-H., Watson, J. A. et al. *Sci. Rep.*, 7 (2017), 41023.

26 Bandara, C. D., Singh, S., Afara, I. O., Tesfamichael, T., Wolff, A., Ostrikov, K., and Oloyede, A. *ACS Appl. Mater. Interfaces*, 9 (2017), 6746.

27 Xue, F., Liu, J., Guo, L., Zhang, L., and Li, Q. *J. Theor. Biol.*, 385 (2015), 1.

28 Hazell, G., May, P. W., Taylor, P., Welch, C. C., and Su, B. *Biomater. Sci.*, 6 (2018), 1424.

29 Kelleher, S. M., Habimana, O., Lawler, J., O'Reilly, B., Daniels, S., Casey, E., and Cowley, A. *ACS Appl. Mater. Interfaces*, 8 (2016), 14966.

30 Salvadori, M. C., Araújo, W. W. R., Teixeira, F. S., Cattani, M., Pasquarelli, A., Oks, E. M., and Brown, I. G. *Diamond Relat. Mater.*, 19 (2010), 324.

31 Mertens, M., Mohr, M., and Brühne, K. *Appl. Surf. Sci.*, 390 (2016), 526.

32 Salvadori, M. C., Araújo, W. W. R., and Teixeira, F. S. *Diamond Relat. Mater.*, 19 (2010), 324.

33 Rietwyk, K. J., Wong, S. L., and Cao, L. *Appl. Phys. Lett.*, 102 (2013), 91604.

Chapter 4 – Using mixed-size seeding to grow diamond onto GaN and AlN surfaces for thermal applications

4.1 Chapter objectives

The semiconductor market is constantly growing, with gallium nitride (GaN) becoming a vital material for several technologies, especially for high-power, high-frequency devices in telecommunications [1]. However, with increasing power comes increasing heating of these devices, with GaN requiring cooling solutions that currently do not exist.

With the apparent need for improved thermal management for GaN-based HEMTs, the aim of this project was to grow diamond films onto GaN while maintaining a low thermal resistance. This was carried out as one-half of a work package within the much larger EPSRC programme grant on GaN-DaME, overseen by M. Kuball and part of a 5-university consortium.

For this, a novel seeding technique utilising a mixture of both micro- and nanodiamond was developed, with the goal of reducing the impact that the diamond nucleation region has on the overall thermal properties. Using this technique, diamond growth was performed on both GaN-on-Si and AlN-on-Si samples which were then characterised by a thermal testing method, permitting the thermal interface properties to be explored without requiring devices to be built.

Much of the content presented here was published in [2], with the GaN results also being used for [3]. The experimental work regarding seeding was carried out jointly with A. Piracha, with the author carrying out all growth used in the work reported herein. Thermal testing was performed by D. Field, Z. Abdallah and J. Pomeroy of the Center for Device Thermography and Reliability (CDTR) in the University of Bristol School of Physics. X-ray tomography data were collected by G. R. Mackenzie of the UoB Interface Analysis Centre, and F. Massabuau of the University of Cambridge Department of Materials Science and Metallurgy provided some of the SEM images, with the other images taken by the author. Wafers of GaN- and AlN-on-Si were provided by D. Hinz of University of Cambridge Department of Materials Science and Metallurgy.

4.2 Introduction

4.2.1 Note on terminology

In this chapter, the ability to conduct thermal energy both within the bulk of one material and across boundaries between multiple materials is discussed extensively. As such, specific terminology is used to determine between these.

Thermal conductivity is the rate of heat flow across a given thickness of material divided by the temperature difference between the two ends measured and has units of W m^{-1} K^{-1}. Thermal conductivity is an intrinsic material property, dependent on the material and its quality; *i.e.* single-crystal diamond has a thermal conductivity of 2.4 ×10^3 W m^{-1} K^{-1} [4], which is retained within each crystallite within a polycrystalline diamond layer. However, across the width of a high-quality microcrystalline diamond film, grain boundaries cause phonon scattering decreasing the thermal conductivity to ~2.0 ×10^3 W m^{-1} K^{-1} [5], and decreases further as the quality and grain size decrease.

Interfacial thermal boundary resistance (TBR) is the temperature difference across an interface of two materials divided by the heat flow across the interface area, with units of m^2 K W^{-1}. This resistance is dependent on the acoustic similarity of the two materials – how easily the phonons of one material can couple with the phonons of the other – and the quality of the interface itself. As such, stronger covalent bonding between the materials reduces the interfacial thermal resistance, while weak interactions, such as van der Waals forces, result in higher resistances. Delamination of one material from the other causes the interfacial thermal resistance to tend towards infinity.

Effective thermal boundary resistance (TBR_{eff}) is a combined thermal resistance term used to simplify the overall effect of thermal resistances across a multi-layered structure. This is affected by the boundary resistance of each interface, the thermal resistance (the inverse of the thermal conductivity) of any thin films used as adhesion layers, and any other properties which alter thermal transport, such as poor-quality regions of the material near the interface. TBR_{eff} has units of m^2 K GW^{-1} and is useful as a simple metric for how easily thermal energy can travel through the materials used in a structure, such as from the GaN to the diamond in a GaN HEMT with a diamond heat spreader, where a lower value represents better transport.

4.2.2 Gallium nitride and its use for HEMTs

Gallium nitride (GaN) has recently found popularity for its electrical properties, with applications in high-power, high-frequency devices [1,6]. One particularly significant area is in GaN high electron mobility transistors (HEMTs) for use in transmitter base-stations, especially with the push towards higher power requirements with the next generations of technology [7]. Often, these devices use a combination of GaN and AlGaN layers, with the AlGaN acting as a barrier between the gate and the GaN layer. The interface of the GaN and AlGaN layers causes the device to function as a field-effect transistor (FET) [8]. An example of a GaN HEMT is shown in Figure 4.1.

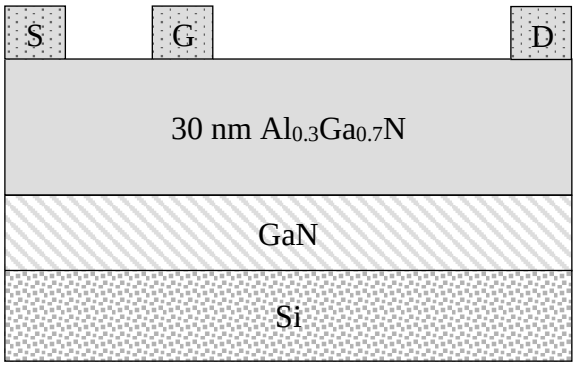

Figure 4.1: A schematic diagram of a typical AlGaN/GaN HEMT. S is the source where carriers enter the channel, G is the gate which varies the channel conductivity, and D is the drain where the carriers leave the channel. These devices commonly use AlGaN as the wide-band-gap layer to separate the GaN buffer layer from the gate. Si is used as a handle wafer. Adapted from [7].

However, these devices are limited in their usage to much lower powers than they are theoretically capable of due to poor thermal management. The channels are a source of highly localised heating, resulting in degradation and poor reliability [9,10]. If GaN-based HEMTs are to play a role in future technologies, a means of improving thermal management is critical to allow these devices to both obtain the required power densities and improve reliability to yield a viable lifetime.

Current commercial GaN devices utilise silicon carbide (SiC) as a handle wafer and heat spreader, with a ~2 µm-thick layer of GaN deposited onto it *via* a thin nucleation layer [11]. The SiC layer offers a much better thermal conductivity than the GaN (~450 vs 160 W m^{-1} K^{-1}),

but the nucleation layer and the microstructure of the GaN at the interface effectively act as a barrier to the generated heat travelling out of the GaN and into the SiC, where the heat is removed by an external cooling system. However, by replacing this SiC substrate with a higher-thermal-conductivity substrate, for example, diamond (2000 $W\ m^{-1}\ K^{-1}$ [5]), the RF output power density of the GaN device could be increased by up to 3 times [12], along with improved device reliability and performance [5,13].

4.2.3 Combining diamond and GaN

In order to make full advantage of the excellent thermal conductivity of diamond, the GaN layer would need to be in direct contact with bulk single-crystal diamond, which presents numerous challenges. Firstly, large-area (the minimum scale of commercially viable devices would use 100 mm diameter wafers) single-crystal diamond is not widely yet available. Alternatively, the use of a high-quality polycrystalline diamond with micron-scale grains would offer comparable thermal conductivity in the direction of the grains, so would be a viable substitute. However, the GaN hexagonal wurtzite structure is not compatible with the diamond cubic diamond structure, so device-quality GaN layers would be very difficult to deposit onto diamond [14]. The most successful attempt to do this thus far was *via* the growth of single-crystal AlN onto single-crystal (111) diamond, which acted as a buffer layer assisting in the subsequent deposition of AlGaN/GaN HEMTs [15,16]. These devices performed well and operated at lower temperatures, confirming the benefits of using a diamond wafer as a heat-spreader [17,18]. However, the fabrication steps used are too expensive to be commercially viable, serving a useful purpose in confirming the value in further investigation, but unlikely to ever be used on an industrial scale. However, even these efforts to grow GaN directly onto diamond have resulted in rather poor quality GaN [17,19] which degrades device performance. Because the function of GaN HEMTs is highly dependent on the quality of GaN, it is not worth sacrificing the device performance simply to gain the benefits from the diamond heat spreader. As such, depositing GaN onto diamond is probably not suitable for many applications.

Directly bonding preformed layers of diamond onto GaN wafers has also been attempted, both using adhesion layers [20] and spark plasma sintering [21], but both of these methods have drawbacks. Adhesion layers add another thermal interface, reducing the efficacy of the diamond heat spreader, while also introducing stresses to the wafers leading to warping and breakage. Spark plasma sintering often results in unfavourable interlayer configurations,

inducing etching and altering the crystal phases of both materials. As such, neither of these techniques is considered viable as a method to produce GaN-on-diamond.

Diamond growth onto GaN is challenging but remains the most feasible method, because the quality of the diamond is far less important than the quality of the GaN, and through CVD, diamond thin films are relatively easy to produce. However, there are several issues in growing diamond directly onto GaN that have been previously identified. First, diamond CVD usually uses substrate temperatures above 800°C and a H-atom-rich environment. In these conditions, the atomic hydrogen can etch GaN to form NH_3 and liquid Ga, both preventing diamond deposition and causing damage to the GaN which would reduce device performance [22]. However, with a sufficiently high seeding density, the lateral growth rate of the diamond film can exceed the etch rate and provide a protective layer of diamond before significant etching occurs [23]. Growth at lower temperatures (<750°C) would reduce the damage caused to the GaN wafer from thermal issues, but at the cost of exponentially decreasing growth rate – which means significantly more etching occurs during the initial growth stage – and thus the same issues arising.

Another issue is that gallium does not form a carbide with carbon [24], making the interface dependent on only weak van der Waals interactions rather than strong covalent bonds. Thermal expansion mismatch adds to this problem due to GaN having a much larger thermal expansion coefficient ($5.59 \times 10^{-6}\ K^{-1}$) than diamond ($4.38 \times 10^{-6}\ K^{-1}$) [25]. This results in the GaN contracting much more on post-growth cooling than the attached diamond layer, causing compressive stresses in the diamond layer and bowing of the wafer. This mismatch, combined with the weak bonding between the layers, makes diamond likely to have areas of very poor thermal contact and may even delaminate following growth [22].

One solution to these issues has been the use of thin layers of SiC or SiN as buffers to aid in the adhesion between the diamond and GaN [13]. Although their addition adds another thermal boundary, this may be manageable so long as the buffer layer is thin (<10 nm). Although SiN is a commonly used interlayer for commercial GaN devices, AlN has proven to be a more suitable interlayer; 100 µm diamond films deposited using nanodiamond seeding onto a 250 nm thick AlN layer were reported to have very low thermal barriers [26]. This is achievable because Al readily forms a carbide, aiding in diamond adhesion, and also because AlN has a higher thermal conductivity than SiN, as well as being a useful etch-stop layer for HEMT production [27].

As such, the addition of an AlN layer would not only help the diamond film to adhere, but also benefit the overall material produced for the desired applications. AlN also has a much higher thermal conductivity than SiN, although somewhat lower than SiC (~250 W m^{-1} K^{-1} [28], ~30 W m^{-1} K^{-1} [29] and ~450 W m^{-1} K^{-1} [30] respectively), so would present a much smaller increase to TBR_{eff} than SiN.

Contemporary to this project, a group of collaborators from Cardiff University had used an alternative seeding technique to grow thick, adherent diamond films on AlN with low thermal barrier resistance [26]. In this work, they quoted an "average barrier resistance" of 16 m^2 K GW^{-1}, showing the potential of AlN as a useful interlayer, given that this is comparable to the best reported SiN interlayers at 12 ± 2 m^2 K GW^{-1} [5] for diamond grown in a similar reactor. However, with an understanding of the limitations of TTR as a technique that were not addressed in their work, it was determined that their results may be unreliable, especially as they reported using TTR to probe diamond 100 µm thick, while TTR is usually limited to ~5 µm thick layers [31]. Additionally, with the mixed-seeding method developed during this project offering a significant potential improvement through having microdiamond in the nucleation region, it was expected that results could be improved, both in value and in certainty.

4.3 Methods

4.3.1 GaN and AlN preparation

For this experimental work, epitaxial deposition of either GaN or AlN onto single-crystal 1 mm thick Si wafers was performed using metal-organic CVD by collaborators from the University of Cambridge. The GaN samples had a layer of GaN ~1 µm on a 1.7 µm-thick AlGaN strain-control layer, acting as a buffer between the GaN and Si. The AlN samples did not need the buffer layer, so consisted of 130 nm of AlN deposited directly on the Si handle wafer. Both sets of layers were (0001)-oriented single-crystal with a surface RMS roughness of <1 nm over 5 × 5 µm scans. These wafers were laser-etched and then mechanically cleaved to provide uniform 10 × 10 mm squares to ensure consistency across all growth samples.

4.3.2 Seeding

Seeding was carried out using the electrospray apparatus outlined in Section 2.4.3, using two sizes of diamond particles: (a) 2.0 ± 1.0 µm microdiamond (DIADUST, PM 1-3, van Moppes, Switzerland), which were natural diamond offcuts from polishing and cutting gemstones, and (b) 3.3 ± 0.6 nm detonation nanodiamond (1 wt% in water, Amando, Japan). The process of optimizing the seeding technique is discussed in Section 4.5.1.

4.3.3 Diamond growth

Growth was performed using the MW CVD reactor, following the procedure in Section 2.3. All growth runs were carried out with a 4% CH_4 in H_2 gas mixture, with both microwave power and chamber pressure varied between 1100–1500 W and 110–150 Torr, respectively, which, in turn, allowed growth at 750–950°C, as determined by calibrated one-colour pyrometry. To allow for the requirements of some experiments, growth duration was used to vary the thickness of the diamond films.

4.3.4 Transient thermoreflectance

To measure the thermal barriers present, an analytical technique called transient thermoreflectance (TTR) was utilized, as described in Section 2.6.5 and [32]. As explained there, this method uses rapid laser pulses to probe the TBR_{eff} for grown structures, with the capacity to determine the value for individual layers after suitable calibration.

However, TTR has one major limitation for this experiment. Because the temperature detection is based on reflectivity, surfaces with high roughness can scatter the laser light, altering the measured results. As such, diamond samples could only be thin films in order to keep the surface of the polycrystalline diamond as smooth as possible. In order to mitigate this scattering problem to some extent, 3 samples were run for each data set, and TTR was performed on 3 regions per sample to provide a statistically large set of data to work with. For TTR, the thickness of the diamond films was required, so after TTR measurements had been taken, samples were laser-cut for cross-sectional SEM. Additionally, the fitting technique used to produce TBR_{eff} values from the data output from TTR required the use of material “constants”, such as the thermal conductivity of each material. Unfortunately, there was significant

uncertainty in each of these values due to the unknown nature of the interfaces. For example, all the diamond films were considered to have the same thermal conductivity, while in reality, there was a huge range of thermal conductivities, especially when comparing nanodiamond to microdiamond seeding.

All TTR data were gathered by D. Field, who also fitted the data to produce TBR_{eff} values with assistance from J. Pomeroy and Z. Abdallah, all members of the CDTR.

4.3.5 X-ray tomography

X-ray tomography (XRT) was utilized to generate 3D images of sample cross-sections non-destructively. These images were produced by taking 4500 sequential X-ray slices while rotating the sample over 360° at intervals of ~0.08°, using the settings stated in Section 2.6.6. The XRT data show the varying densities of the layers of the sample. All XRT data were gathered by G.R. Mackenzie.

4.4 Results

4.4.1 Mixed-size seeding

Prior to growth on GaN, a novel method of seeding was developed in order to yield a high thermal conductivity diamond film but with sufficient protection of the surface below to avoid significant etching. To this end, a mixture of microdiamond (MD) and nanodiamond (ND) were used to seed silicon substrates using the electrospray technique, using the range of parameters shown in Table 4.1, with corresponding SEM images of the films shown in Figure 4.2.

Table 4.1: Parameters used for mixed-seeding optimisation, with corresponding images for each shown in Figure 4.2. *m* is the mass of the microdiamond powder used and *n* is the number of drops of nanodiamond seeding solution used.

Image in Figure 4.2	*m* (mg)	x_{MD}	*n* (drops)	x_{ND}
(a)	5	1	50	2
(b)	7	1	50	2
(c)	10	1	50	2
(d)	10	1	50	5
(e)	10	2	50	2

From this optimisation, the following conditions were determined to be the most suitable for the subsequent work: MD seeding: m = 10 mg, x_{MD} = 2; ND seeding: n = 50 drops, x_{ND} = 1; MD+ND seeding: m = 10 mg, x_{MD} = 2, n = 50 drops, x_{ND} = 2.

The difference in the grain size and quality of the grown diamond when using the mixed seeding compared to the ND-only seeding can be seen in Figure 4.3.

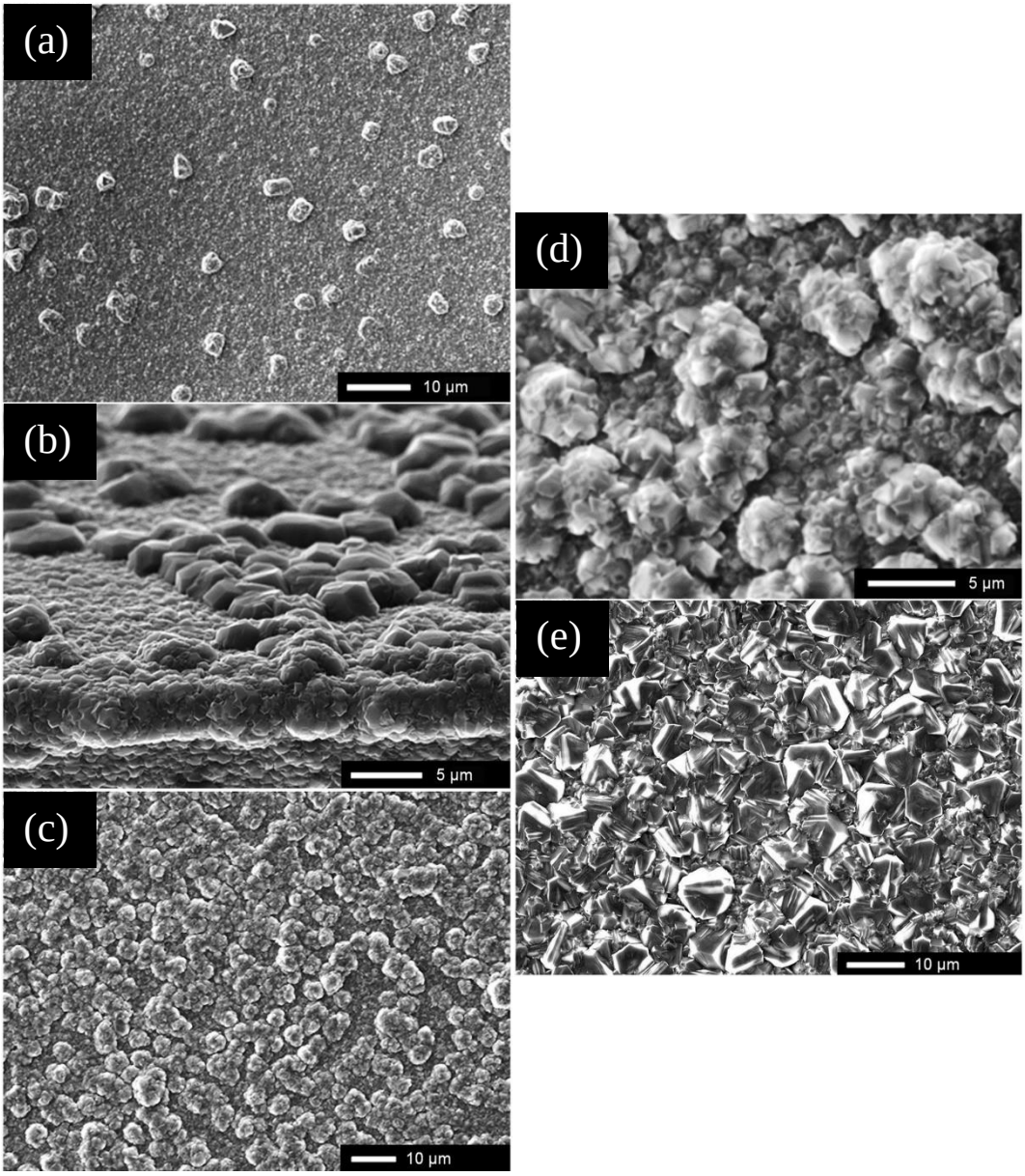

Figure 4.2: SEM images of thin (~4 µm) diamond films using the range of seedings listed in Table 4.1.
(a): very sparse distribution of MD seeds
(b): ~50% monolayer of MD seeds
(c): ~80% monolayer of MD seeds
(d): ~80% monolayer of MD seeds, but higher ND coverage resulted in a much rougher film, with the ND growing onto the MD.
(e): ~95% monolayer of MD seeds, with voids filled well by ND, producing a high-quality microdiamond film.
Images taken by A. Piracha.

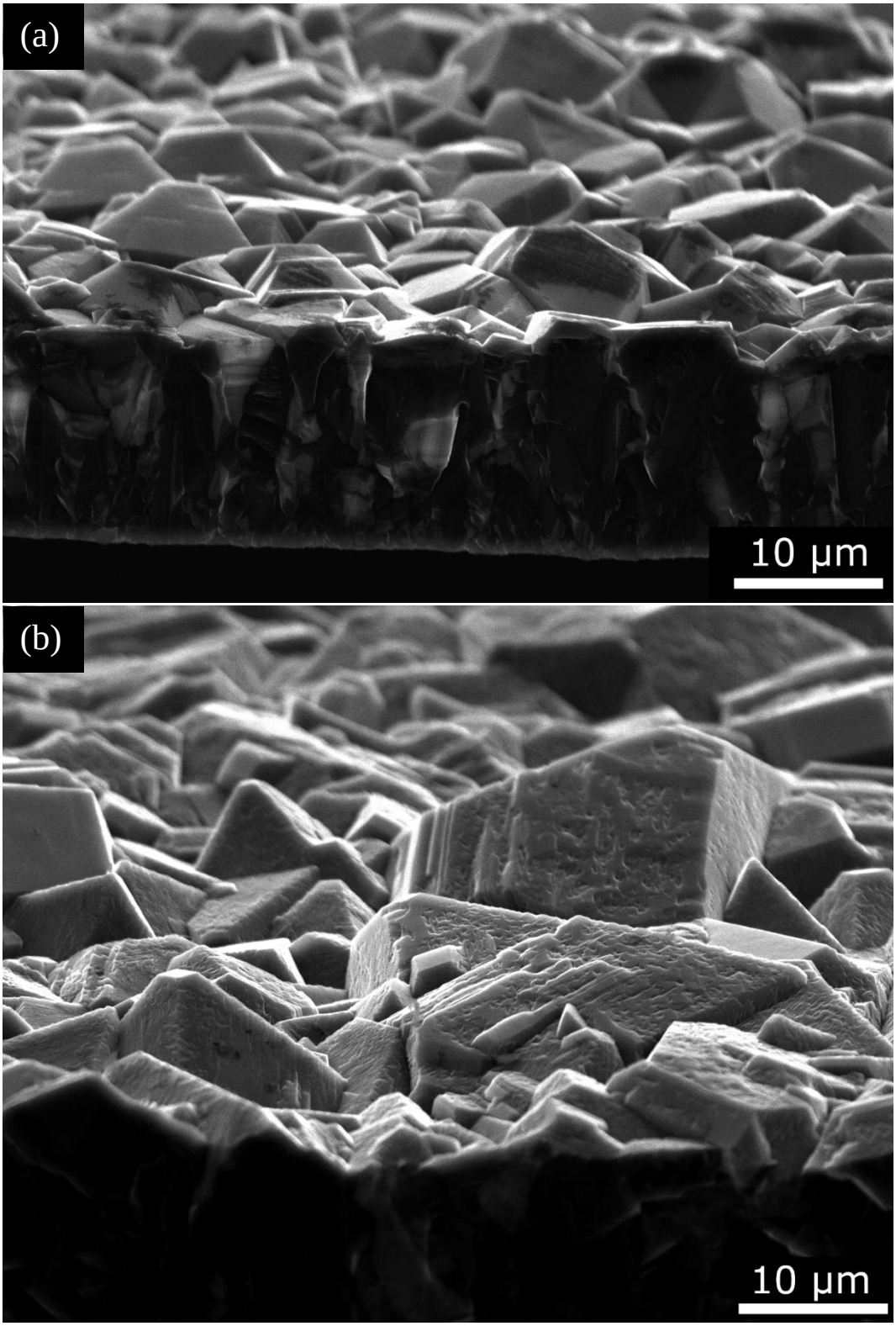

Figure 4.3: Cross-section SEM images of diamond films grown onto Si substrates using (a) MD+ND and (b) ND only seeding. The quality of the diamond is visibly higher for the mixed MD+ND seeding, with smoother faces to the crystals and sharper facets.

4.4.2 Diamond-on-GaN

100 µm thick diamond films were then grown using the mixed seeding technique, using GaN-on-Si wafer as the substrates, but these films delaminated following growth, as can be seen in both the SEM images in Figure 4.4 and the XRT images in Figure 4.5.

Transient thermoreflectance was then carried out on samples seeded the same, but only grown to ~2 µm thicknesses, which confirmed the lack of any covalent bonding between the diamond and GaN layers from the high TBR_{eff} determined, with the mean and lower limits for the TBR_{eff} shown in Figure 4.7.

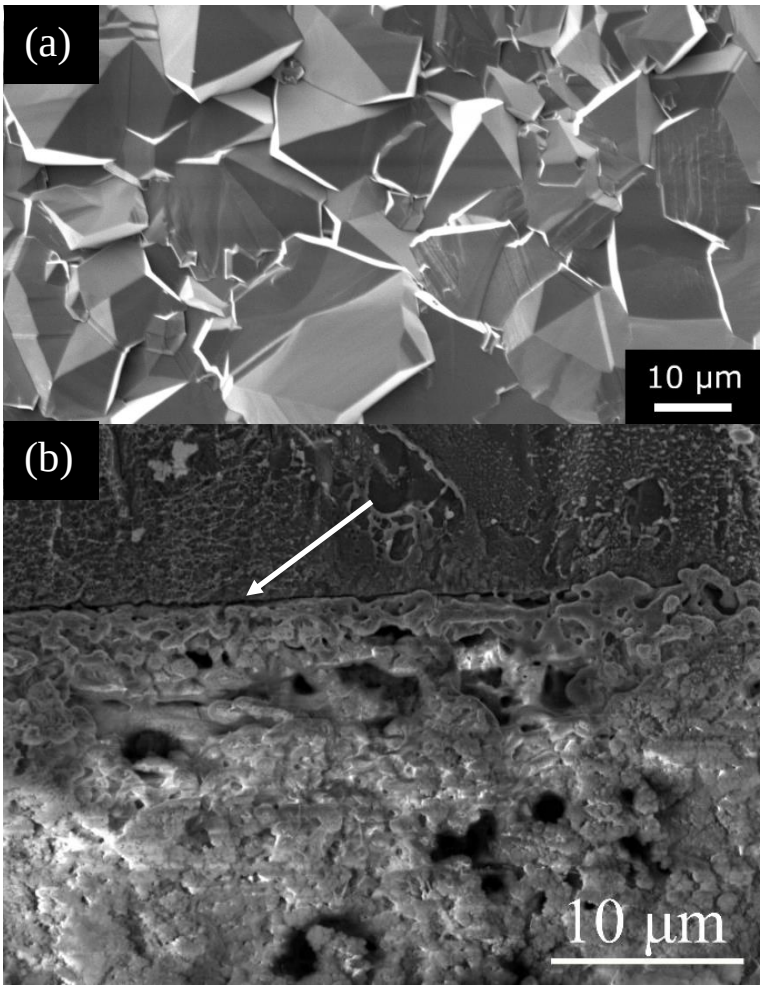

Figure 4.4: SEM images of a diamond film ~110 µm thick grown at 750°C on GaN-on-Si.
(a) Top-view image of the diamond film showing the large grain sizes and sharp facets, indicating high-quality microcrystalline diamond. Image by A. Pirahca.
(b) Cross-sectional image, with the arrow pointing to a significant crack/void along the interface between the diamond and GaN-on-Si indicated. Image by F. Massabuau.

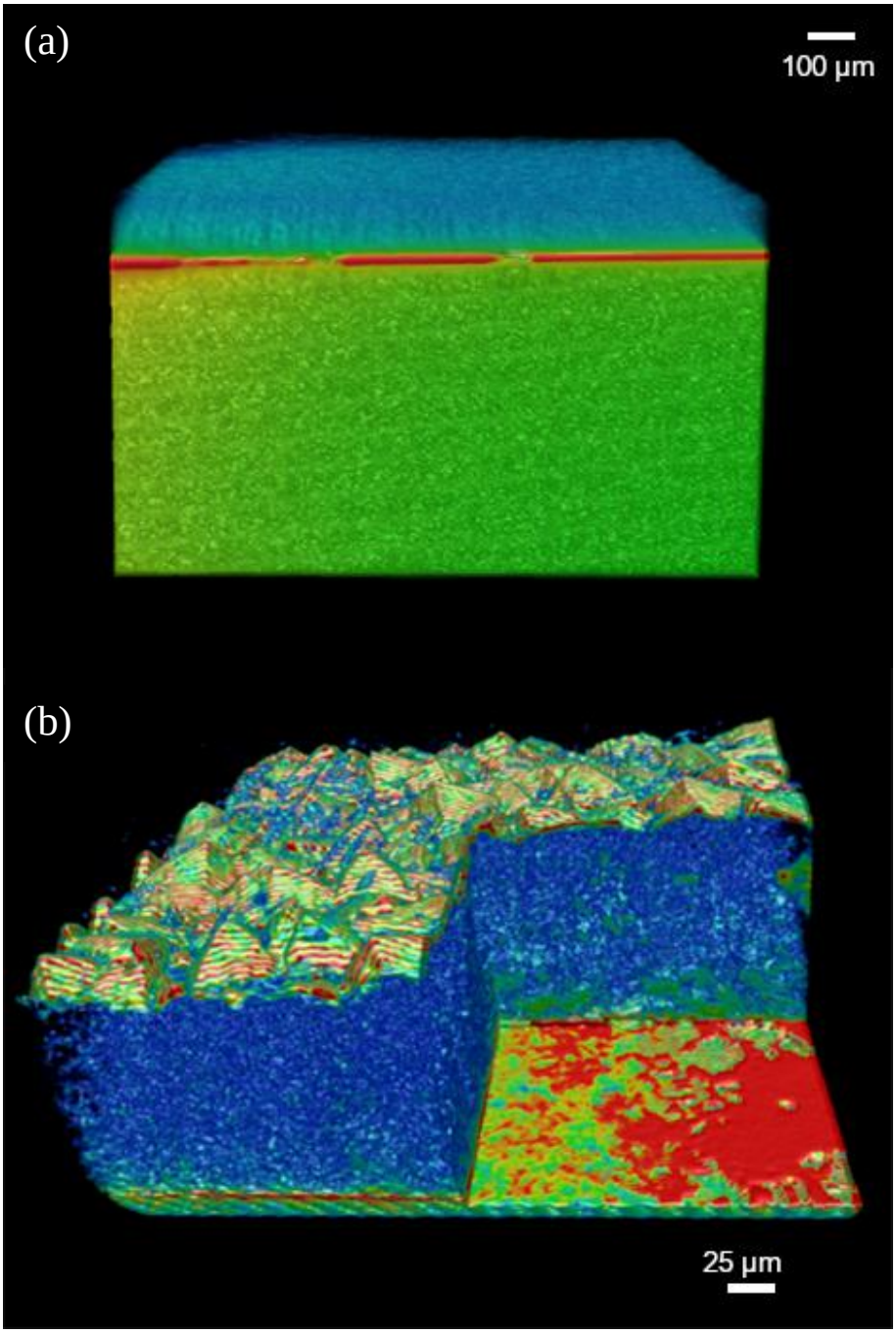

Figure 4.5: XRT images of a diamond film ~110 µm thick grown at 750°C on GaN-on-Si.
(a) False-colour image showing diamond in blue and Si in green. A region of much lower density is shown in red – thought to be a gap between the layers.
(b) 3D image with a section removed *via* software showing the interface. As can be seen, this area is non-uniform, with significant areas of little-to-no-interface shown in red.
Images taken by G. R. Mackenzie.

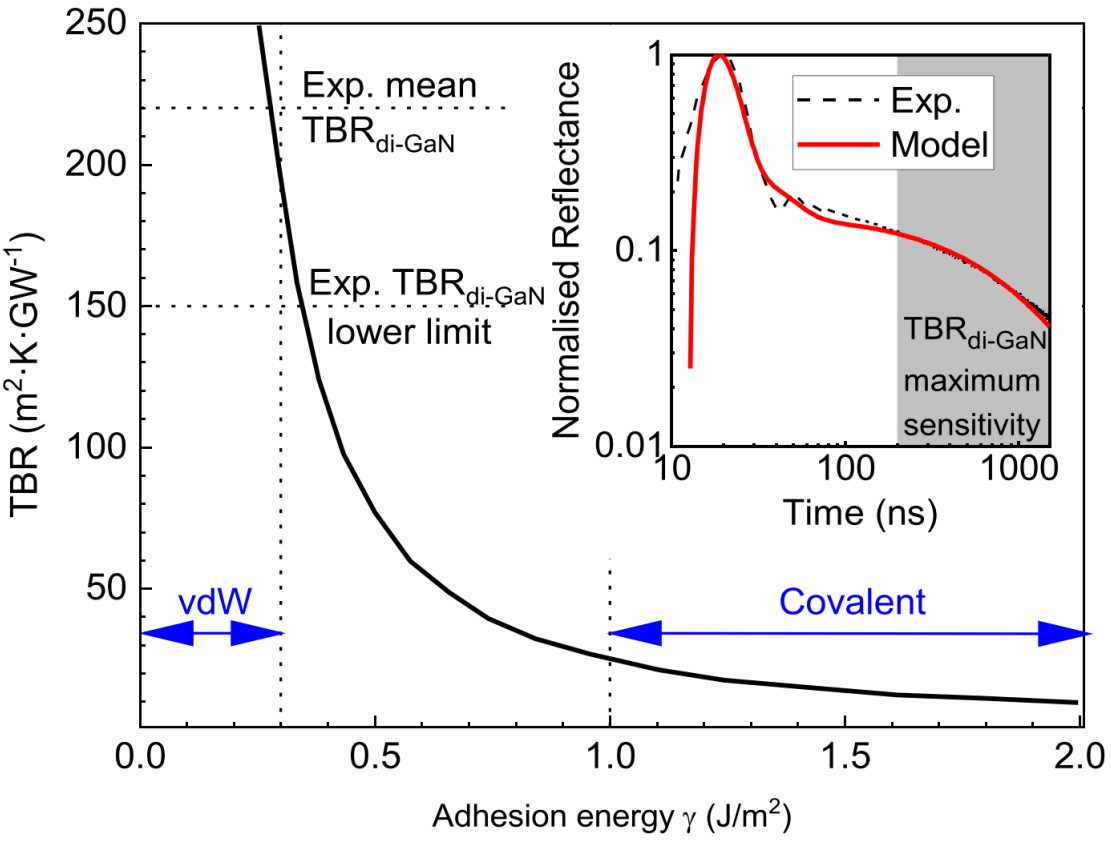

Figure 4.6: Theoretical model showing the dependence of TBR with respect to adhesion energy for a diamond/GaN interface. Typical ranges for both van der Waals (vdW) and covalent adhesion energies are indicated, as well as both the measured average and lower limit TBR values for the diamond-on-GaN samples shown in Figures 4.5 and 4.6. Inset shows a typical measured transient thermoreflectance trace and the model fitted to obtain TBR. Adapted from [3].

4.4.3 Diamond-on-AlN

With the lack of covalent bonding between the diamond and GaN layers confirmed, an interlayer of AlN was used, as this would allow for the diamond to covalently bond to it and offered a useful etch-stop for the proposed final GaN-based HEMTs. In order to reduce the impact of surface roughness on the TTR measurements, only thin layers (1-2 μm) of diamond were grown on the AlN-coated wafers. Substrates of AlN-on-Si were seeded with MD, ND or the mixed MD+ND, and growths were carried out at 750, 850 and 950°C for a duration of 1-2 hours.

All of the MD-seeded samples delaminated immediately following growth, so no SEM images or TTR data could be gathered for them. Cross-sectional SEM images for ND- and MD+ND-seeded samples grown at 950°C for 1 hour are shown in Figure 4.7.

TBR_{eff} values were calculated for the samples grown, shown in Table 4.2.

Table 4.2: CVD diamond grown on AlN-on-Si, along with thicknesses of the diamond films and TBR_{eff} values of the interfaces generated *via* TTR. MD+ND seeding consistently produced a lower TBR_{eff} than only ND seeding.

Growth Temperature / °C	Seeding	Duration / h	Thickness / μm (± 0.1 μm)	TBR_{eff} / (m^2 K GW^{-1})	Number of samples averaged for TBR_{eff}
750	ND	2.0	(delaminated)	-	-
750	MD+ND	2.0	0.8	5.5 ± 2.6	4
850	ND	1.0	0.6	67 ± 58	5
850	MD+ND	1.0	1.2	1.47 ± 0.35	5
950	ND	1.0	2.3	109 ± 54	6
950	MD+ND	1.0	2.0	3.36 ± 0.94	5

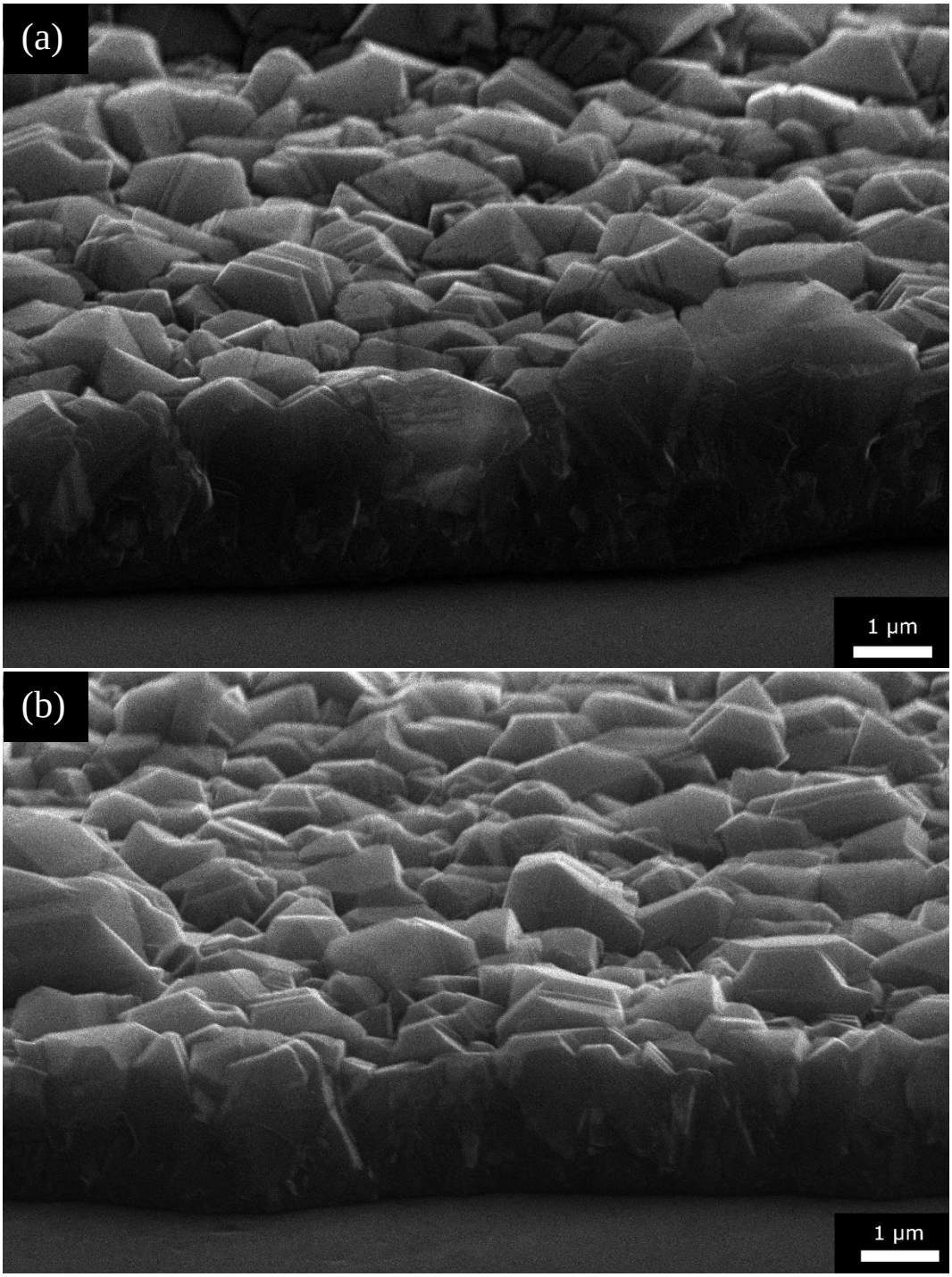

Figure 4.7: Cross-sectional SEM images of (a) ND- and (b) MD+ND-seeded samples, following growth for 1 h at ~950°C. The generated films appear similar, both ~2 µm thick and both featuring similar surface roughness. As such, these should introduce similar scattering for TTR measurements, affecting the measured TBR_{eff} by a similar systematic error, and thus making values comparable.

4.5 Discussion

4.5.1 Development and optimisation of mixed-size seeding

The concept behind the use of mixed seeding is shown in Figure 4.8. Microdiamond (MD) crystals have multiple large smooth facets such that they can have a good contact area with the surface, allowing for efficient thermal transport at the interface. This offsets the usually significant detrimental effect of the nucleation layer, by providing large grains with high thermal conductivity from the surface upwards. However, large seeds are unable to pack closely enough to cover the surface fully, meaning that areas of the GaN will be exposed to the CVD gas mixture and be etched during growth. The voids or pinholes in the seeding layer also reduce the overall contact area at the interface. To counter this, nanodiamond (ND) seeds are then dispersed over the surface to fill in the gaps between the MD seeds, eliminating voids and avoiding etching of the surface.

To implement this, a range of solutions of MD and ND were prepared. For MD, m = 5-10 mg of the MD powder was added to 25 mL of methanol, then sonicated for 2 h to break up any aggregates and form a suspension. 1 mL of this suspension was then dispersed onto the samples using the electrospray, x_{MD} = 1–3 times. The ND seeding solutions used a varied number of drops (n = 10–50) of the stock solution added to 25 mL of methanol, then sonicated for 2 h before electrospraying onto the already MD-seeded substrates, x_{ND} = 1–5 times.

From these parameters, a selection was chosen for growth. Initial results showed that for close-packed monolayer coverage of ND, 50 drops applied twice (x_{ND} = 2) was necessary. However, with this parameter determined, focus shifted to getting good coverage of the MD. This set of samples is shown in Table 4.1, with corresponding SEM images of the films grown shown in Figure 4.2.

This optimisation showed that higher quantities of the MD were needed than initially thought. Figure 4.3(e) is the only condition with an acceptable coverage, where the resultant film appears to be microcrystalline without any gaps.

The difference in the quality of the diamond grown when using the mixed seeding compared to the ND-only seeding was significant, with the facets being much sharper and the faces smoother for the mixed seeding technique. Figure 4.3 shows cross-section SEM images of both a MD+ND and a ND sample, showing this difference.

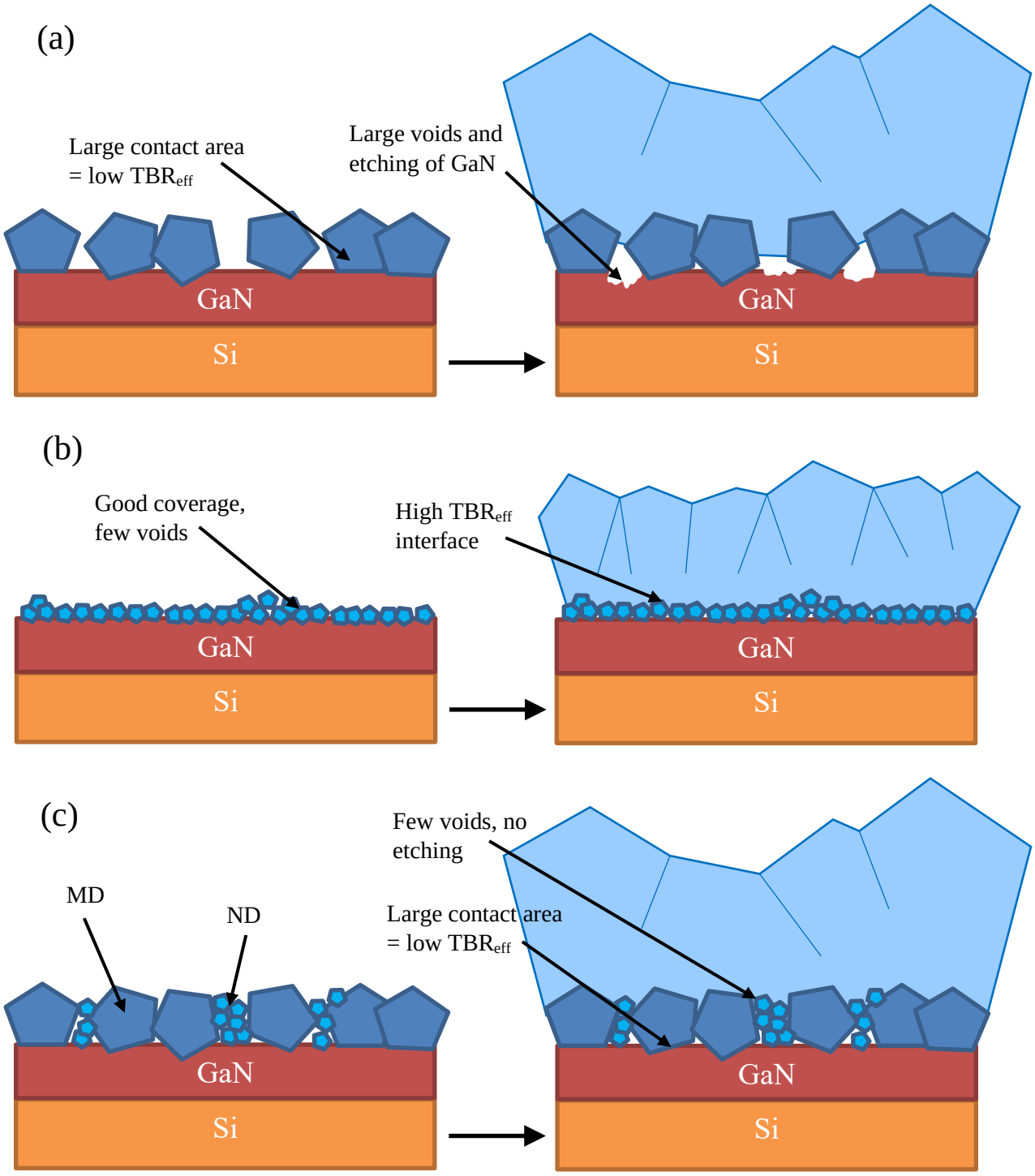

Figure 4.8: Schematic diagram showing the rationale behind two-step seeding. Left panels show seeding, while right panels are after CVD diamond growth. (a) Seeding with only MD gives a good thermal contact, but the exposed GaN between the grains, with etching causing damage and voids, reduce overall heat transfer ability. (b) Seeding with only ND gives good coverage so few voids and minimal etching occur during diamond growth, but the ND at the interface causes a high TBR_{eff}. (c) MD seeding followed by ND seeding provides the high contact area of MD, and subsequently lower TBR_{eff}, while ND fills the voids and protects against etching.

4.5.2 Diamond growth on GaN

As expected, with the large thermal mismatch between the diamond and the GaN, most of these thick diamond films delaminated, even with growth being carried out at 750°C. Figure 4.4 shows SEM data for a film which did not delaminate at the end of growth. While the diamond film is of a high quality, shown in Figure 4.4 (a), the interface between the diamond and GaN is non-uniform, with a significant crack visible for 10s of µm in Figure 4.4 (b). The XRT data in Figure 4.5 offer additional insight into the state of the interface showing both a region of significantly lower density – likely a void – in Figure 4.5 (a), and generally regions of limited-to-no contact as seen in the 3D cut-away in Figure 4.5 (b). As XRT was performed immediately following growth, any damage to the interface is only due to the stresses resulting from cool-down rather than the mechanical cleaving of the sample for SEM. However, due to the limited resolution of the XRT, this is not conclusive.

TTR was attempted on these samples but given the combination of high surface roughness and likely regions of delamination, values for TBR_{eff} could not be determined with any accuracy. However, TTR was able to produce data for 3 much thinner (~2 µm) diamond films, which were sufficiently smooth to not cause issues with laser scattering, and these data are the experimental values in Figure 4.6. These films, grown at 750°C for 4 h using MD+ND seeding were each measured by TTR three times in different regions of the sample, and the mean TBR_{eff} across all the measured values was 217 ± 66 m^2 K GW^{-1} – nearly an order of magnitude higher than the TBR_{eff} of SiC-on-GaN (~30 m^2 K GW^{-1}) that is used for standard devices. As such, it was concluded that diamond grown directly onto GaN, while technically possible, was not a suitable method of providing a GaN HEMT with a heat spreader. This was an expected result, given the poor adherence of the diamond to GaN seen in Figures 4.5 and 4.6, and is consistent with previous attempts [22].

From the thermal results, it was apparent that the diamond film had, at best, only limited regions of good contact, and this conclusion was supported by the gaps visible in the SEM and XRT images. However, this outcome was somewhat expected, given that Ga is unable to carburise, limiting the bonding between the diamond and GaN surfaces to only weak van der Waals interactions.

The thermal results that were used in modelling the interface, forming the experimental component of [3] shown in Figure 4.6, were useful in confirming that strong covalent bonds are, indeed, necessary for phonon transport to be effective across the interface between

materials. Van der Waals forces, being much weaker as they are from the interaction of temporary induced dipoles, cause phonon reflection at the surface, making for very poor thermal conductivity across the interface.

This problem combined with the thermal expansion mismatch for diamond-on-GaN, with cracks and voids readily opening between the layers following cooling. These cracks cause delamination – either localised to a small region, or of the whole layer – which further reduce the ability of phonons to propagate through the interface. As such, diamond grown directly on GaN is fundamentally hindered by both thermal and mechanical issues, so an interlayer of some form is required to both limit delamination and provide stronger bonding between the layers.

4.5.3 Diamond growth on AlN

For this set of experiments, several methods were used to try to improve the reliability of the TTR data. Because the probe laser could easily be scattered by rough surfaces, diamond films would be thin (1-2 μm), as this generally produced a much lower surface roughness. However, given the MD seed crystals were 2.0 ± 1.0 μm, these thin films would still have some significant roughness. Therefore, for each condition, 3 samples were prepared. Each of these samples then underwent TTR measurement in 3 different regions on the surface, then fitted to provide values for TBR_{eff}. Following this, careful data analysis was carried out, which is outlined in Section 4.5.4.

AlN-on-Si substrates were coated with CVD diamond as before, with seedings of MD, ND and MD+ND all used. Growths were carried out at 750, 850 and 950°C for a duration of 1-2 h, aimed at producing 1-2 μm-thick diamond films. Given that over this range, growth rate increases with temperature, it was expected that the 750°C sample would be the thinnest and 950°C the thickest, so the longer duration of 2 h was performed for the lowest temperature set only. Following growth, samples underwent TTR testing, and once these measurements had been made, one sample of each set was cleaved mechanically, allowing the thickness of the diamond film to be determined accurately by cross-sectional SEM.

One immediately apparent result was that every MD-seeded sample delaminated immediately following growth. As such, none of these samples could be used for TTR testing. The delamination was suspected to be a result of the limited contact area at the interface, with the

voids permitting significant etching of the AlN during growth and providing much less anchoring than samples with a coating of ND seeds.

The ND-seeded samples grown at 750°C also delaminated, but the higher temperature samples were able to stick to some extent, while none of the MD+ND samples appeared to delaminate.

Figure 4.7 shows a cross-section of both ND and MD+ND diamond films grown at 950°C. As can be seen, the surfaces were similarly rough, with both featuring a large number of facets, and the films were both ~2 µm thick. This was significant, as the similar roughness and thicknesses provided a basis for good comparison of the measured values of TBR_{eff}, as both would be similarly affected by laser scattering.

Table 4.2 shows the TBR_{eff} values obtained by D. Field, which underwent a multi-stage analytical process to provide the presented results. As stated in Section 4.3.4, given the huge potential for uncertainty in the TTR measurements, a careful approach to data analysis was required. The technique assumes efficient absorption of the pump laser and complete detection of the probe laser, both of which are severely affected by surface roughness scattering the lasers. Without the ability to polish the surface of the diamond layers to a suitably low roughness, a means to determine when the lasers had scattered was needed.

In consultation with the TTR experts in the CDTR based on their experience with analysing data from previous work with GaN/diamond samples, it was decided that a TBR_{eff} of > 200 m^2 K GW^{-1} represented either an area of delamination or where surface roughness had caused the measurement probe to scatter excessively to the point where the value was meaningless. These data points were therefore treated as outliers, and not included in any data analysis. In comparison, regions with no delamination and low surface roughness had typical TBR_{eff} values 10 or 100 times lower than this value (see Table 4.2), and within the same sample set gave reasonably consistent values (*i.e.* having a standard deviation around 50% that of the value). From this first criterion, 35 of the original 45 data points were used.

Resulting from this issue, a further experiment was designed to allow for the measurement of TBR_{eff} without significant roughness was devised and is presented in Section 4.7.

With the effect of these results removed, the significant improvement in TBR_{eff} for the mixed MD+ND seeding was already apparent. Averaging across each sample, five of the nine mixed seeding samples had a $TBR_{eff} < 10$ m^2 K GW^{-1}, which is better than the reported "state of the art" value for diamond on GaN of 12 ± 2 m^2 K GW^{-1} [5]. Meanwhile, only one of the nine ND-

only samples was below this threshold, with three of those nine not even being measured due to delamination.

However, averaging across these samples into sets for temperature and seeding resulted in uncertainties greater than the values for most samples, again, with a sizeable impact from the scattering. From here, outlying values were removed while trying to maintain a good quantity of data, and the values presented in Table 4.2 are the result of this.

The MD+ND 750°C set was reduced to only 4 values, but this was necessary as the data ranged so extensively – this was somewhat expected, given the huge range of thickness on these samples.

The ND-only 850°C set featured one notable outlier. Two of the three samples had relatively similar TBR_{eff} values (omitting one value over the 200 m^2 K GW^{-1} threshold) of 61 ± 58 and 77 ± 81 m^2 K GW^{-1} respectively, while the third had an average TBR_{eff} of only 2.2 ± 1.2 m^2 K GW^{-1}. This was the only sample of the nine ND-seeded samples to have a TBR_{eff} < 60 m^2 K GW^{-1}, so it was also considered an outlier and was omitted from the values presented in Table 4.2. If it were to be included, then the TBR_{eff} for that set would be reduced from 67 ± 58 to 43 ± 55 m^2 K GW^{-1} – overall making the value lower but leaving the results somewhat unclear with a higher uncertainty than the value. Doing so would not change the trends or conclusions from the data sets, and so for consistency, the original procedure, *i.e.* treating the unusually low data point as an outlier, was taken as the most justifiable procedure.

As shown by Table 4.2, AlN permitted a much better interface for diamond to act as an effective heat spreader compared to growing directly onto GaN: for the same conditions (MD+ND seeding, 750°C), the TBR_{eff} decreased from 217 ± 66 on GaN to 5.5 ± 2.6 m^2 K GW^{-1} on AlN. However, the results may have been affected by the fact that the diamond growth on the GaN samples was for twice as long as that for AlN.

While the ND-only values were significantly higher than some previously reported in the literature (16 m^2 K GW^{-1} [26]), this literature value was for 100 µm thick diamond and had no information on the number of samples averaged in TTR measurements, nor details about treatment of TTR data outliers, and therefore no uncertainty estimates. This made comparison with our data challenging, as with no information on reproducibility, a diamond thickness substantially higher than TTR is reliably capable of measuring, and a surface roughness likely leading to significant scattering of the probe laser, there was little confidence in their reported values.

Regardless, the results for MD+ND seeding showed a remarkable improvement in TBR_{eff} than for just ND seeding (done either here or in the literature) – a factor of ~44× at 850°C and ~32× at 950°C. These results indicated the MD seeds from the mixed seeding provided a more thermally conductive interface, while allowing a higher quality of diamond to be grown. Additionally, the MD+ND seeding method produced excellent results at 750°C while the ND seeding delaminated, suggesting that the mixed seeding is more adherent than the ND only.

With values of $TBR_{eff} < 6\ m^2\ K\ GW^{-1}$ for all three growth temperatures using MD+ND seeding, these results showed that the mixed seeding technique enabled diamond growth of a suitably high quality and low thermal boundary resistance to be viable for cooling HEMTs, especially when compared to current state-of-the-art values for SiN_x and crystalline AlN interlayers – some values of which are presented in Table 4.3. Note that some of these sources provide no seeding details, so nanodiamond seeding is assumed, given that this the standard seeding used for such experiments.

Comparing the results reported here to these values shows the huge improvement in TBR_{eff} that the mixed seeding method offers. The benefit that such an improvement offers in high-power, high-frequency devices using GaN cannot be understated – this seeding allows access to cooling potential which enables more efficient, more effective devices across a range of applications, especially in telecommunications.

Table 4.3: GaN-on-diamond TBR_{eff} values for a range of interlayers, showing the state-of-the-art. Measurements were TTR or time-domain thermoreflectance (TDTR), at ns, ps, or fs timescales.

Interlayer Material	Interlayer Thickness / nm	Seeding	TBR_{eff} / (m^2 K GW^{-1})	Measurement Technique	Ref
AlN Crystalline	130	ND	67 ± 58	ns TTR	This work
AlN Crystalline	130	Mixed	1.47 ± 0.35	ns TTR	This work
AlN Crystalline	250	ND	16	ns TTR	[26]
SiN_x	22	No details	17.4 ± 3.0	ps TDTR	[29]
SiN_x	31	No details	31.8 ± 5.3	ps TDTR	[28]
SiN_x	5	No details	9.5 +3.8/-1.7	fs TDTR	[33]

4.6 Summary and conclusions

A seeding technique utilising a mixture of micro- and nanodiamond has been developed, allowing for a near-monolayer coverage of microdiamond seeds, with voids being filled by nanodiamond. This technique allowed the high thermal conduction of the microdiamond to be combined with the substrate protection offered by nanodiamond. This seeding method was then used to grow diamond films onto Si, GaN-on-Si and AlN-on-Si wafers, with the goal of reducing the region of poor thermal conduction occurring at the interface between the diamond and the substrate.

Growth directly on GaN was mostly unsuccessful, with delamination of the diamond film often occurring and a high TBR_{eff} being measured by TTR. This was expected due to the necessity of covalent bonding to yield a good thermal transfer alongside the fact that Ga-C bonds are not viable. As such, with only weak van der Waals forces to contend with, plus the stresses induced by thermal expansion mismatching, the films often had substantial voids at the interface and were prone to cracking and delamination. These growths however provided the experimental data to support thermal modelling methods which have been integrated into the TTR technique, improving the quality of results produced by the fitting software for all materials analysed.

Furthermore, AlN has been shown to be viable as an interface layer, being compatible with GaN, diamond and Si, chemically and mechanically. The diamond films did not delaminate when grown on AlN unless the samples were cleaved, and the low TBR_{eff} values measured for the films indicate the presence of covalent Al-C bonding allowing for excellent thermal transport across the interface. Utilising the mixed-seeding method, TBR_{eff} values $< 6\ m^2\ K\ GW^{-1}$ were produced across a range of CVD growth temperatures, with the optimal TBR_{eff} value of $1.41 \pm 0.35\ m^2\ K\ GW^{-1}$ being produced from growth at 850°C. This was significantly lower than the values obtained using purely nanodiamond seeding by a factor of more than 30× and was substantially better than current state-of-the-art values.

As such, the use of a mixed micro- and nanodiamond seeding technique offers an unprecedented improvement to heat-spreading for higher power GaN HEMTs, with the better thermal transport allowing for more efficient cooling. This could allow for industry to unlock the potential offered by GaN with the cooling enabling higher power operation, longer lifetimes and better efficiency.

4.7 Future work

Future studies should be focussed on optimising the diamond growth itself, while also attempting to carry out these experiments on a complete stack of layers representative of an actual GaN HEMT: while the results on AlN are a huge improvement on previous results, growth of a diamond-on-AlN-on-GaN is vital to proving the viability of this in diamond heat-spreading of GaN HEMTs.

An experiment that was planned was to assess the thermal conductivity of the diamond films at the interface. To do this, growth using the different seedings and plasma conditions would be carried out on Si, holes cut into the back of the Si and then etched to expose the diamond surface. These would permit analysis of how the thermal conductivity changes with larger grains at the interface.

As an extension of the above, performing the same set of experiments but with the diamond grown on AlN-on-GaN with a Si handle wafer to replicate a device's layers would allow for a proper assessment of the effectiveness of such a device.

References

1 Mishra, U. K., Parikh, P., and Wu, Y.-F. *Proc. IEEE*, 90 (2002), 1022.

2 Smith, E. J. W., Piracha, A. H., Field, D. et al. *Carbon*, 167 (2020), 620.

3 Waller, W. M., Pomeroy, J. W., Field, D., Smith, E. J. W., May, P. W., and Kuball, M. *Semicond. Sci. Technol.*, 35 (2020), 095021.

4 Inyushkin, A. V., Taldenkov, A. N., Ralchenko, V. G., Bolshakov, A. P., Koliadin, A. V., and Katrusha, A. N. *Phys. Rev. B*, 97 (2018), 144305.

5 Sun, H. R., Simon, R. B., Pomeroy, J. W., Francis, D., Faili, F., Twitchen, D. J., and Kuball, M. *Appl. Phys. Lett.*, 106 (2015), 111906.

6 Pearton, S. J., Ren, F., Zhang, A. Z., and Lee, K. P. *Mater. Sci. Eng.*, R30 (2000), 55.

7 Mishra, Umesh K., Shen, Likun, Kazior, Thomas E., and Wu, Yi-Feng. GaN-Based RF Power Devices and Amplifiers. *Proceedings of the IEEE*, 96, 2 (2008), 287-305.

8 Asif Kahn, M., Kuznia, J. N., Van Hove, J. M., Pan, N., and Carter, J. *Appl. Phys. Lett.*, 60 (1992), 3027.

9 Pomeroy, J. W., Uren, M. J., Lambert, B., and Kuball, M. *Microelec. Reliability*, 55 (2015), 2505.

10 Bar-Cohen, A., Maurer, J. J., and Altman, D. H. *J. Electron. Packag.*, 141 (2019), 040803.

11 Pengelly, R. S., Wood, S. M., Milligan, J. W., Sheppard, S. T., and Pribble, W. L. *IEEE Trans. Microwave Theory Tech.*, 60 (2012), 1764.

12 Altman, D., Tyhach, M., McClymonds, J. et al. *14th IEEE ITHERM Conference* (2014), 1199.

13 Pomeroy, J. W., Bernardoni, M., Dumka, D. C., Fanning, D. M., and Kuball, M. *Appl. Phys. Lett.*, 104 (2014), 083513.

14 Hageman, P. R., Schermer, J. J., and Larsen, P. K. *Thin Solid Films*, 443 (2003), 9.

15 Taniyasu, Y. and Kasu, M. *J. Cryst. Growth*, 311 (2009), 2825.

16 Hirama, K., Taniyasu, Y., and Kasu, M. *J. Appl. Phys.*, 108 (2010), 013528.

17 Hirama, K., Kasu, M., and Taniyasu, Y. *IEEE Electron. Device Lett.*, 33 (2012), 513.

18 Hirama, K., Taniyasu, Y., and Kasu, M. *Jpn. J. Appl. Phys.*, 51 (2012), 090114.

19 Dussaigne, A., Malinverni, M., Martin, D., Castiglia, A., and Grandjean, N. *J. Cryst. Growth*, 311 (2009), 4539.

20 Francis, D., Faili, F., Babić, D., Ejeckam, F., Nurmikko, A., and Maris, H. *Diam. Relat. Mater.*, 19 (2010), 229.

21 Kim, J. C., Lee, J., Kim, J. et al. *Scr. Mater.*, 142 (2018), 138.

22 May, P. W., Tsai, H. Y., Wang, W. N., and Smith, J. A. *Diam. Relat. Mater.*, 15 (2006), 526.

23 Zhou, Y., Anaya, J., Pomeroy, J. et al. *ACS Appl. Mater. Interfaces*, 9 (2017), 34416.

24 Hájek, B., Kohout, B., and Flemr, V. *Monatsh. Chem.*, 117 (1986), 1157.

25 Oba, M. and Sugino, T. *Diamond Relat. Mater.*, 10 (2001), 1343.

26 Mandal, S., Yuan, C., Massabuau, F. et al. *ACS Appl. Mater. Interfaces*, 11 (2019), 40826.

27 Smith, M. D., Cuenca, J. A., Field, D. E. et al. *AIP Advances* , 10 (2020), 035306.

28 AlShaikhi, A. and Srivastava, G. P. *J. Appl. Phys.*, 103 (2008), 083554.

29 Cho, J., Francis, D., Altman, D. H., Ashedghi, M., and Goodson, K. E. *J. Appl. Phys.*, 121 (2017), 055105.

30 Manoi, A., Pomeroy, J. W., Killat, N., and Kuball, M. *IEEE Electron Device Lett.*, 31 (2010), 1395.

31 Touzelbaev, M. N. and Goodson, K. E. *Diamond Relat. Mater.*, 7 (1997), 1.

32 Pomeroy, J. W., Simon, R. B., Sun, H., Francis, D., Faili, F., Twitchen, D. J., and Kuball, M. *IEEE Electron Device Lett.*, 35 (2014), 1007.

33 Yates, L., Anderson, J., Gu, X. et al. *ACS Appl. Mater. Interfaces*, 10 (2018), 24302.

Chapter 5 – Growth of templated diamond using self-assembled polymer micelles

5.1 Chapter objectives

This chapter focusses on the use of self-assembled polymer micelles as a means to explore many of the parameters used in MW CVD diamond growth, as well as develop a novel method to create diamond microstructures with a high degree of control. These structures utilise a material that is well-understood as a precursor to diamond growth, and can be made in a wide range of shapes and sizes. Developing a good understanding of how to grow diamond from this versatile starting point offers an untapped potential of applications.

This chapter initially presents a brief summary of the preliminary work undertaken. From this, a "conversion step" was shown to be of importance, and the conditions for this step are determined. Many preliminary growths simply testing the viability of this technique were carried out but are not included here in depth, as they contributed little of value beyond suggesting further work could be successful.

From there, attempts to map out the rate of diamond growth as a function of temperature and growth duration were performed. An unusual finding in this experimental set led to further experiments investigating the microwave power instead of the temperature. Using one power setting, the growth over time on these micelles was then investigated. Much of these data form the basis of a publication currently being prepared. Along with these, this section also details some additional work on the "conversion step", attempting to minimise the duration to reduce the etching while still performing sufficient "conversion" for the growth step to be effective. Then much broader parameter explorations were performed, with both methane concentrations and thermally decoupling spacer wire thicknesses varied for a range of times.

All micelles for the experimental work were made by S. Pearce and M. Brumwell of the University of Bristol. All AFM imaging was performed by R. Harniman at the Chemical Imaging Facility at UoB, who also carried out much of the post-processing to generate numerical data. L. Yang performed the initial diamond growth in the HF reactors, but all subsequent growth runs in the MW reactor were carried out by the author.

The parameter exploration formed the foundations for a set of undergraduate projects, with students focussing on different parameter spaces. Diamond growth was performed by the author, imaged by R. Harniman, then numerical data obtained from the images by the students for their particular analyses. These data were re-combined and reassessed by the author. The students were P.-L. Cairns, M. Juszczak, S. Muthuganesan, S. Qiao, D. Smid, M. Standen and F. Xu, all from UoB as their work comprised a part of their BSc or MSci projects. Additionally, much of the diamond growth used for M. Brumwell's extended project was done by the author, with some elements of this work presented.

5.2 Introduction

5.2.1 Block copolymers

Block copolymers (BCPs) – sets of macromolecular building blocks bound either covalently or non-covalently – can be self-assembled in solution to produce "micelles" of soft-matter-based nanoparticles [1,2,3]. These micelles can be modified in shape and size by tuning the different polymer segments to alter their interactions with each other and with the solvent during self-assembly [4,5]. There are numerous polymerization techniques using an assortment of BCPs to create a whole range of structures – for an excellent review of these, see [6].

Research has been carried out with specific focus on crystallisation-driven self-assembly of organometallic-organic diblock copolymers containing polyferrocenylsilane (PFS). Using these, a range of shapes of micelle structures have been fabricated, both in the form of one-dimensional cylinders [7,8] and two-dimensional platelets [9,10], for example the 2D platelets shown in Figure 5.1.

5.2.2 Motivation to use self-assembled polymer micelles for diamond growth

These self-assembled micelles present a unique opportunity to grow diamond in a well-defined structure. Providing a method could be found to utilise the shape of the micelle – either by using the micelle as a "seeding template" or through converting the micelle itself – diamond could potentially be grown into structures with dimensions on the order of 1 µm. Previously, micelles have been used to produce hard, inorganic structures; 1D nanotubes of materials such as TiO_2 and SiO_2 have been made this way [11].

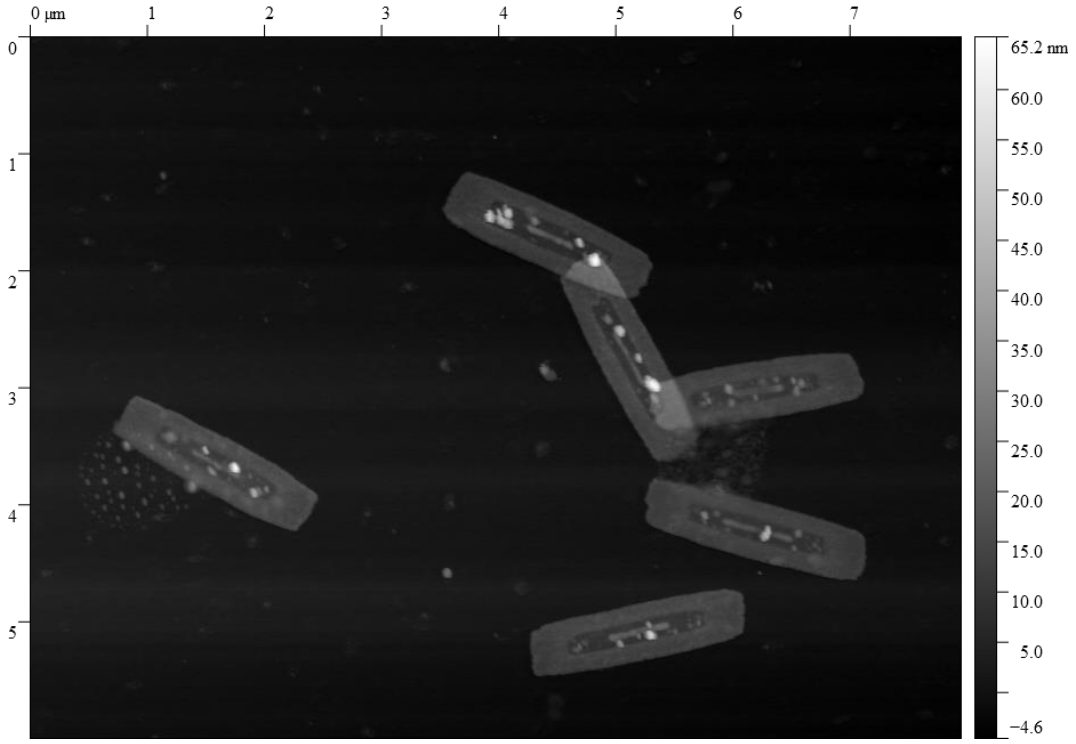

Figure 5.1: AFM image of rectangular self-assembled micelles.

Diamond growth using these micelles could allow for many of the parameters used in diamond growth to be probed in a new way, effectively using the micelles as highly localised seeding with excellent uniformity within the patterned regions with no seeding outside of them. Because of this, growth rate could be mapped far more precisely than with a normal film, and the effects of the parameters of growth – such as temperature, pressure, methane proportion *etc.* – on both the rate and the morphology of the diamond assessed with this novel approach.

Beyond the capacity to explore parameters in a nanoscale, the ability of make nano- to micro-scale structures of high-purity diamond with significant control of the shape, size and morphology could have applications in a broad range of fields, for example electrochemical [12], water treatment [13], antibacterial [14] and cell-growth [15] applications.

5.3 Methods

5.3.1 Micelle sample production

The self-assembled micelles were made in two steps. Initially, using monodisperse poly(ferrocenyldimethylsilane-b-2-vinylpyridine) (PFDMS-*b*-P2VP) as 1D cylindrical seeds, core platelets were produced by adding PFDMS[PPh_2Me]I unimer. These core platelets were ~1 µm long, ~400 nm wide and ~10 nm thick. From these, an outer block to the micelle was grown using additional PFDMS-*b*-P2VP. The methods used are presented in further detail in [16,17]. Transmission electron microscopy (TEM) images for each of these steps are shown in Figure 5.2.

Due to the polymeric nature of these micelles, their structure and chemical composition varies extensively depending on the specific shape and thickness produced. However, the micelles consist almost wholly of carbon and hydrogen, with small quantities of Si and Fe, so offer an excellent carbon source for diamond growth.

These micellar solutions were then dispersed onto a handle wafer so diamond growth could be performed. For this, single-crystal Si wafers were laser cut and then mechanically cleaved into 10 × 10 mm squares, providing a sufficiently polished surface for better AFM imaging that was also compatible with diamond CVD conditions. Rectangular platelet micelles (0.05 mg mL^{-1} in MeOH) with lengths of ~2.5 µm and widths of ~500 µm were drop-cast (5 µL), then dried *via* evaporation in N_2 prior to use.

Where possible, one batch of micelles were used for a set of experiments in order to minimise the impact of any batch-to-batch variability on results. However, given the number of samples used for this project and the volume of micellar suspension produced per batch, it was not possible to do all the experimental work with one single set of micelles. However, all micelle batches were produced following the same method.

Micelles used for the initial work in Section 5.4.1 and most of 5.4.2 were prepared by S. Pearce across several batches. The micelles used for the constant-power time-varied set in Section 5.4.3 was another batch, made by M. Brumwell under the author's supervision, who also produced the micelles for the broader parameter exploration in Section 5.4.4.

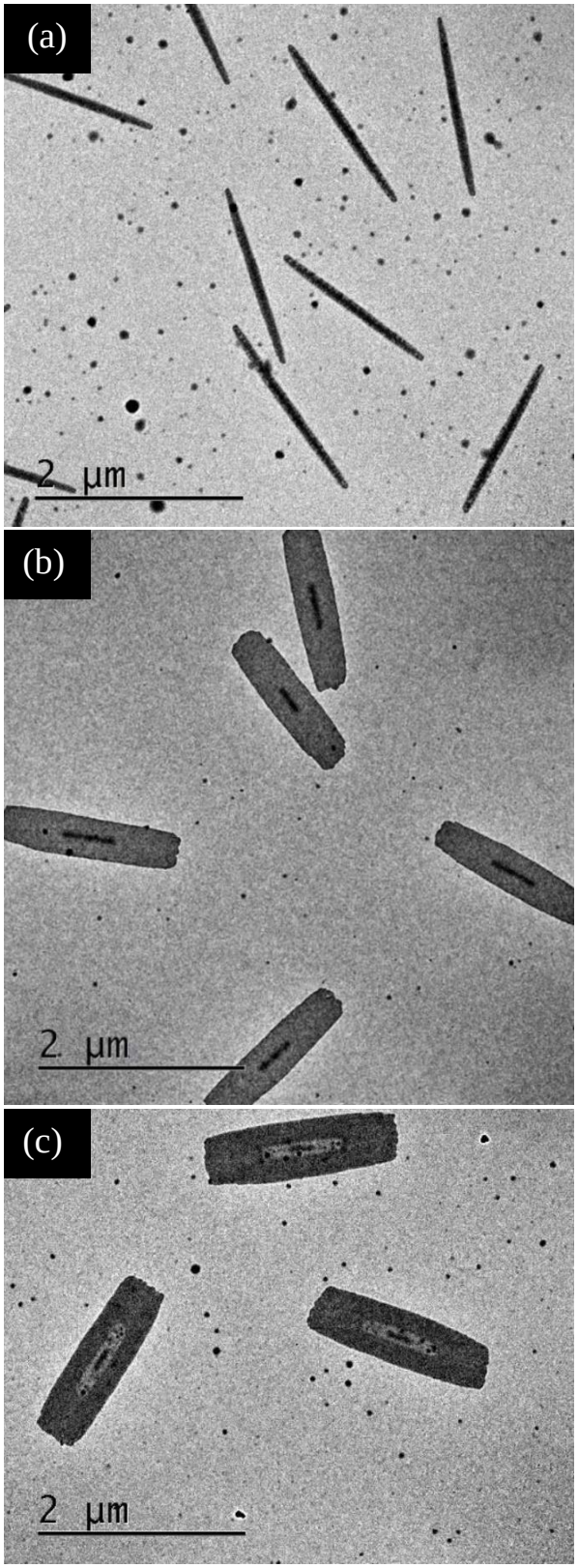

Figure 5.2: TEM images of (a) PFDMS-*b*-P2VP 1D cylinders, (b) "core" platelets, with PFDMS[PPh_2Me]I unimer forming a layer around the PFDMS-*b*-P2VP seed, and (c) rectangular platelets from the addition of blended PFDMS-*b*-P2VP/PFDMS[PPh_2Me]I unimer. Adapted from [17].

5.3.2 Diamond growth

While a few of the preliminary growths were carried out in HF reactors, it was quickly realised that these provided much less fine-control than was possible in the MW reactor. As such, all the diamond growth reported herein was performed in the MW reactor, the operation of which is outlined in Section 2.2.

As discussed in Section 5.3, it was found that a lower temperature "conversion" step enabled better diamond growth. For this, a lower power run was carried out which was able to provide a better nucleation source for diamond growth by converting the BCPs of the micelle into a material better suited for growth. This step would be carried out immediately prior to growth of a sample, with the reactor chamber being kept under vacuum between the conversion and growth steps. This step was further tuned to improve AFM data, discussed in Section 5.5.

Growth was carried out without the use of a thermally decoupling spacer wire between the water-cooled baseplate and the disk onto which samples were placed. Instead, a 10 mm-thick 25 mm-diameter disk was used throughout this work (rather than the standard for the reactor: 6.4 mm thick and 32 mm diameter). This disk without a spacer was found to provide better temperature control for the temperatures being used than using the typical thinner disk with a wire spacer.

Given the short durations of most growth runs, timings were standardised, with growth itself following the procedure stated in Section 2.3. The "growth time" was defined as the duration between when the pressure stabilised at the desired set-point and when the CH_4 flow was stopped. Due to the addition of CH_4 into the gas mixture before this time and the short period of time where significant CH_4 remained in the chamber after the flow was stopped (~30 s), these times do not fully represent the actual time when growth could occur but enabled a consistent basis for "growth duration" to be presented. To aid reproducibility, the plasma would be maintained for exactly 2 min after the CH_4 flow was stopped. This allowed time for the CH_4 to be pumped out and the surface to have graphitic residues etched away by the atomic H in the plasma.

Additionally, as it was found early on that slightly variations in the MW chamber conditions could alter results, where possible, growth for each sample set was done consecutively to allow consistency within each set. Herein, diamond grown on micelles is referred to as "templated diamond" to differentiate it from more typical growth of diamond films over the entire surface of a substrate.

5.4 Results

5.4.1 Preliminary growth

Initially, Si substrates were seeded with nanodiamond to aid in nucleation. Following fluorination, 2D circular platelets (~1.5 µm diameter, 15 nm thick) followed by a nanodiamond solution was performed *via* drop-casting, with the sample washed in MeOH to remove any nanodiamond that had not adhered to the micelles. Diamond growth was then performed in the hot-filament CVD reactor for 20 min with standard growth conditions, resulting in the structure shown in Figure 5.3.

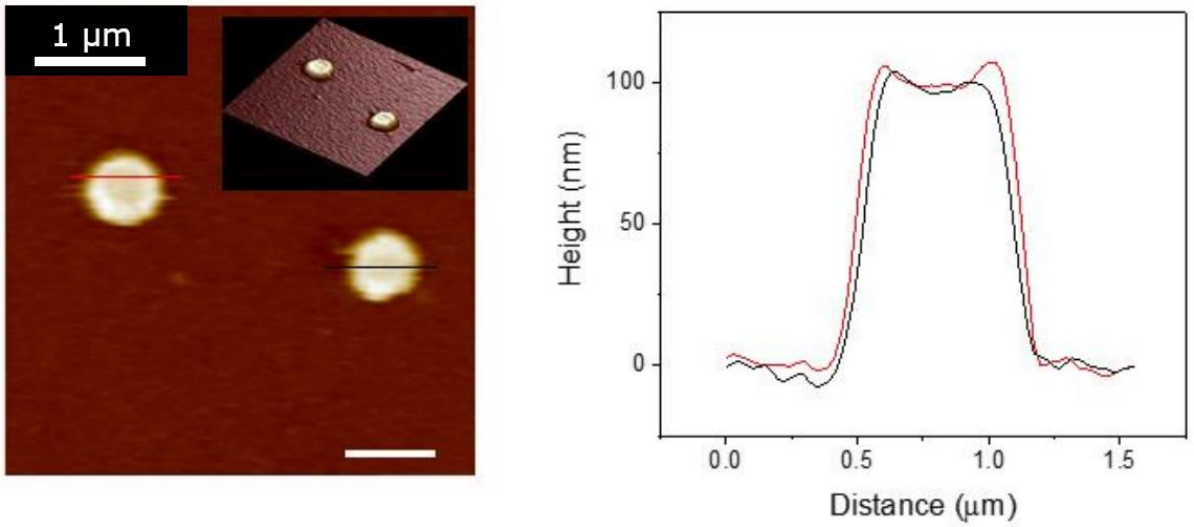

Figure 5.3: AFM image and corresponding height trace of a 2D circular platelet, seeded with colloidal nanodiamond, then grown for 20 min in a HF CVD reactor.

For subsequent samples, growth was carried out in the MW reactor for 5 minutes, and without nanodiamond seeding nor the fluorine termination on the Si, a lower temperature (~500°C) growth run was performed producing diamond in an array of tiny crystals – referred to as "conversion" herein. This was followed by a higher temperature (~600°C) run to grow the converted micelle into a larger diamond structure. These stages of micelle pre-growth, converted and then grown are shown in Figure 5.4.

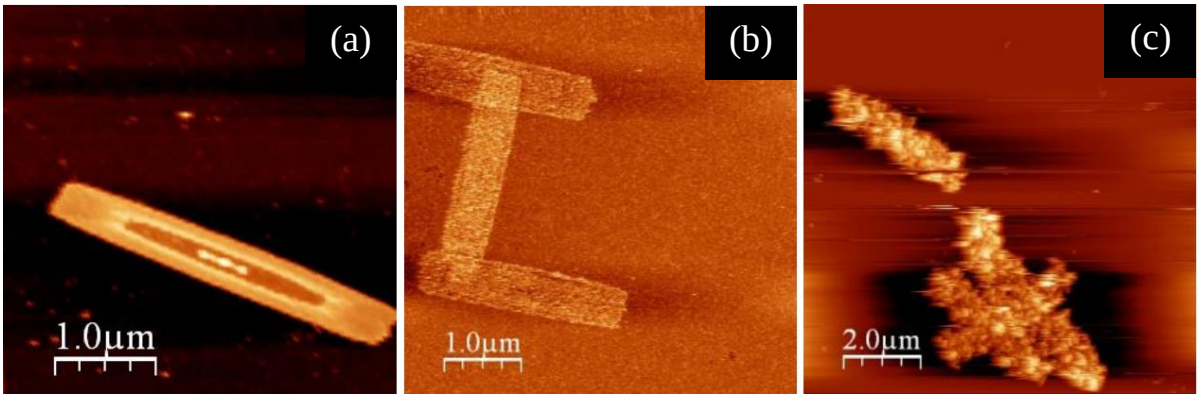

Figure 5.4: AFM images of (a) rectangular platelet prior to any growth, (b) "converted" micelles, grown in a 950 W, 110 Torr plasma for 5 min, and (c) grown micelles, grown in a 1250 W, 130 Torr plasma for 3 min after conversion. Heights of structures are (a) ~15 nm, (b) ~10 nm, (c) 800 nm.

5.4.2 Effect of temperature on micelle growth

A series of growths were carried out over a 520-640°C range in the MW reactor, with every sample being "converted" prior to growth. The conversion step used was 5 minutes in 4% CH_4 at 950 W, 110 Torr, followed by an additional 2 minutes after the CH_4 flow was turned off. Growth was carried out at 130 Torr for 3 minutes, and the results are shown in Figure 5.5.

This was followed by another series of growth runs keeping temperature constant and varying the growth duration between 3 and 120 minutes, shown in Figure 5.6. The temperature chosen was 605°C. An example of the grown structures is shown in Figure 5.7.

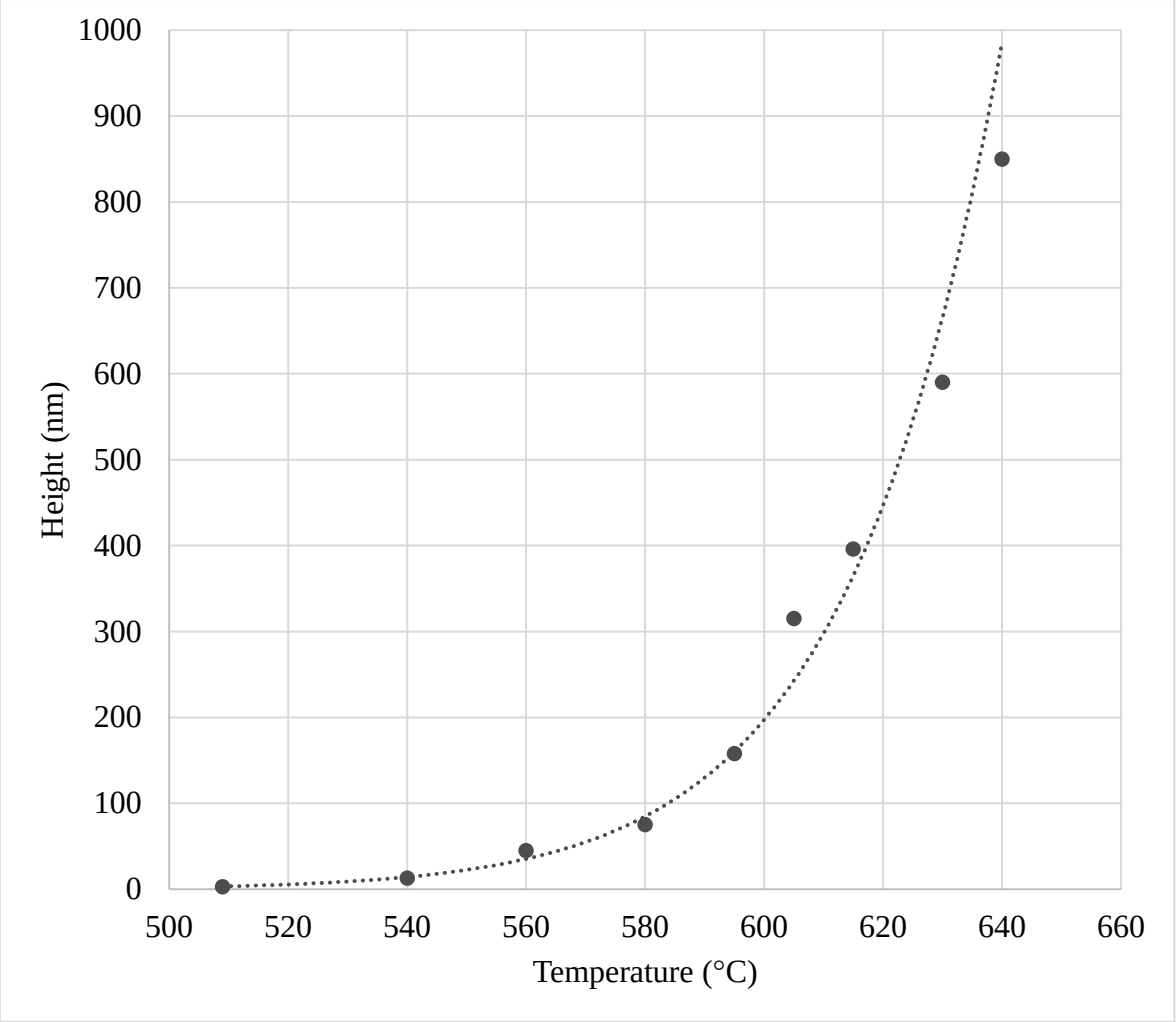

Figure 5.5: Height of templated diamond grown after 3 min at ~130 Torr for a range of temperatures, measured by AFM.

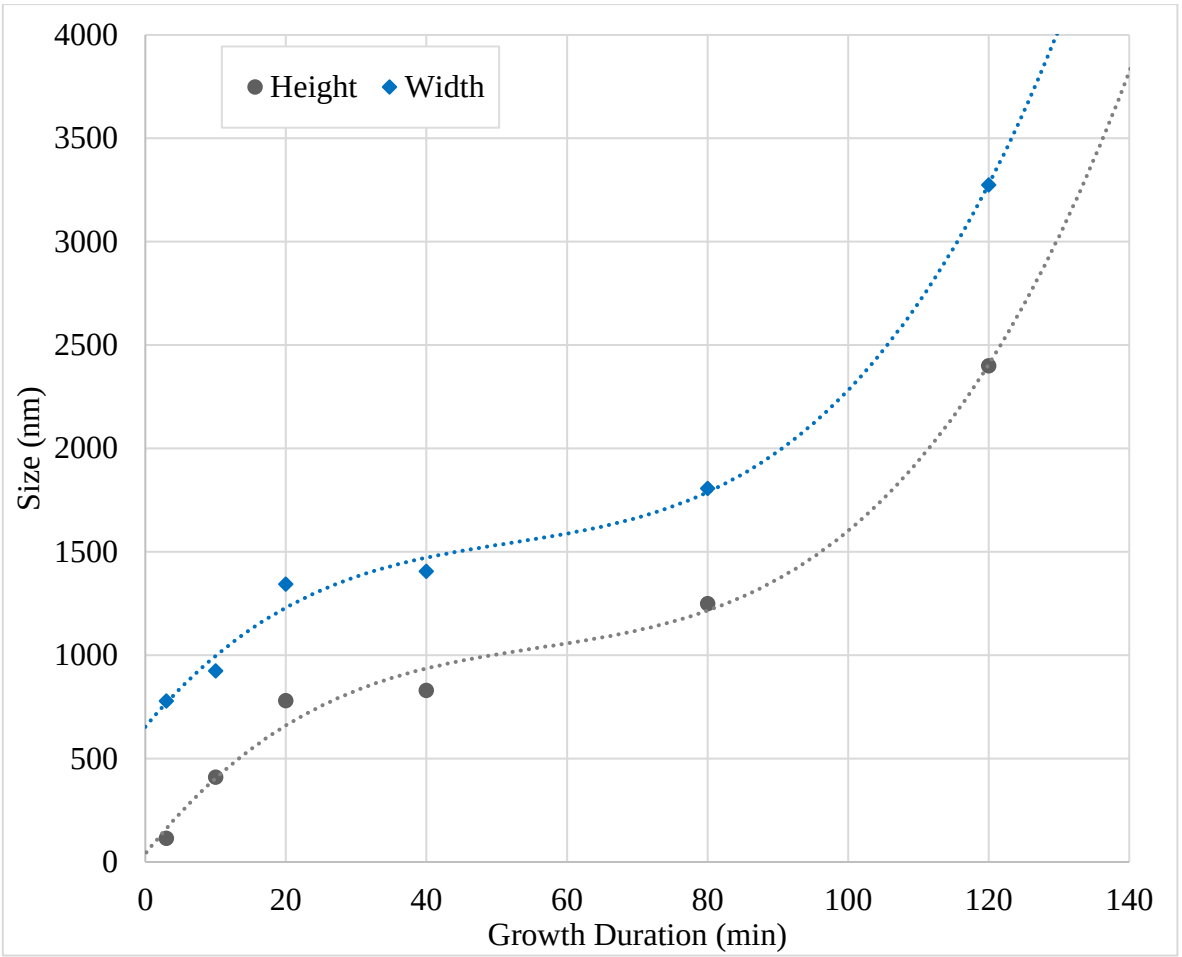

Figure 5.6: Height and width of templated diamond grown at 605°C, ~1200 W, 130 Torr for a range of durations, measured by AFM.

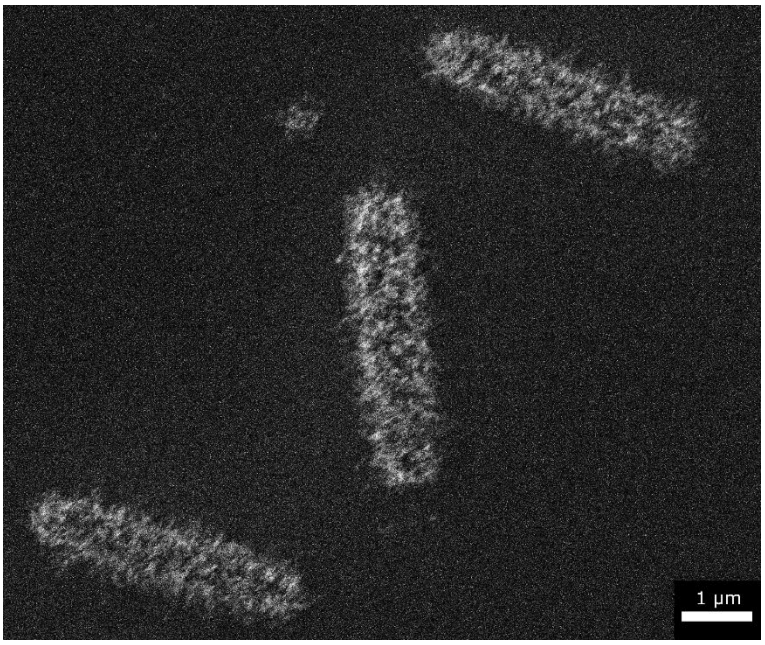

Figure 5.7: SEM image of templated diamonds ~800 nm high, grown at 605°C, 1330 W, 130 Torr for 20 min.

5.4.3 Effect of MW power on micelle growth

Figure 5.8 shows the results for a series of 3 minute growths on micelles with varying microwave power. In order to improve consistency in the methodology, after the 3 min growth duration had elapsed, the MW power and pressure would be immediately set to 1000 W and 100 Torr, respectively.

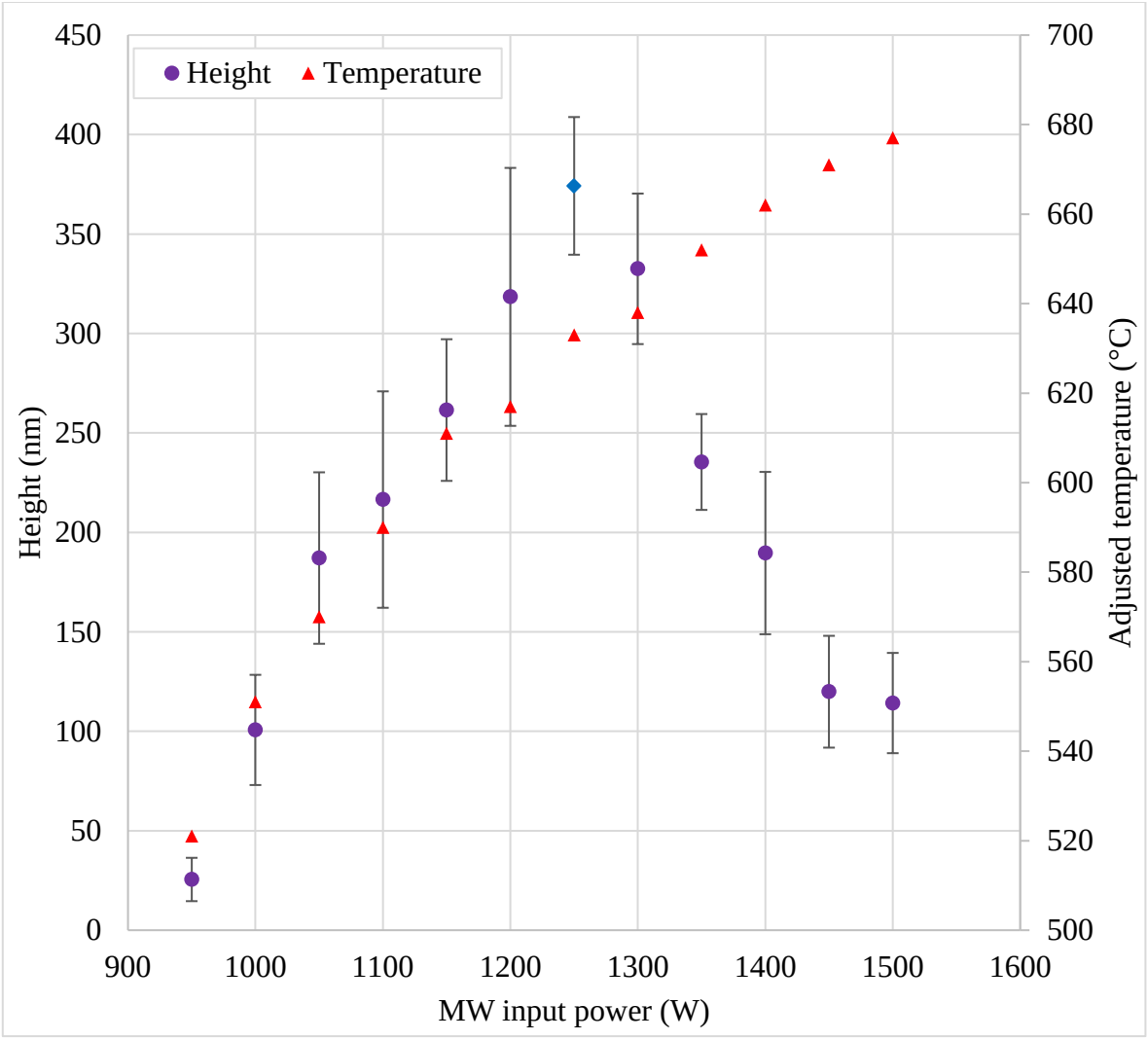

Figure 5.8: Height of templated diamond grown at a range of MW powers, at 130 Torr for 3 min. 1250 W is highlighted as this is the power used for future work. Error bars represent one standard deviation on sample heights measured. Secondary axis shows the temperatures after adjustment. These measurements were made by AFM.

5.4.4 Optimisation of the conversion step

Subsequently, the conversion step was re-assessed, in order to minimise the etching on the Si wafers which would allow for improved AFM. 0, 1, 3, and 5 minute conversions were performed, then followed by a 3 minute growth at 1250 W and 130 Torr, to ensure the growth would not be impacted significantly by reducing the conversion time, with the measured heights shown in Figure 5.9. The 3 minute conversion was not analysed by AFM, as the results from the 1 and 5 minute runs were sufficient to determine that a 1 min conversion was suitable.

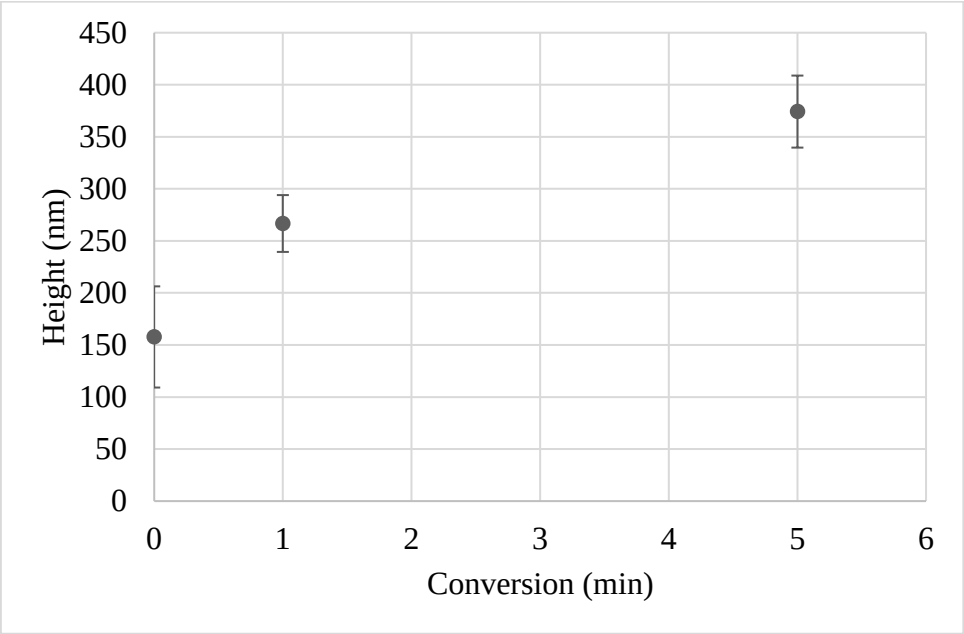

Figure 5.9: Height of templated diamond grown in the same conditions following varied conversion time, measured by AFM. The sample at 0 min conversion duration was a control that was not converted prior to growth.

5.4.5 Growth over varying duration with constant power and pressure

Growth was then performed over a wide range of durations, from 3 to 270 minutes, keeping the pressure constant at 130 Torr and the power at 1250 W for the all the growth periods.

Figure 5.10 shows an example AFM image of the 120 minute growth, and Figure 5.11 presents the heights as measured by AFM for the set of samples.

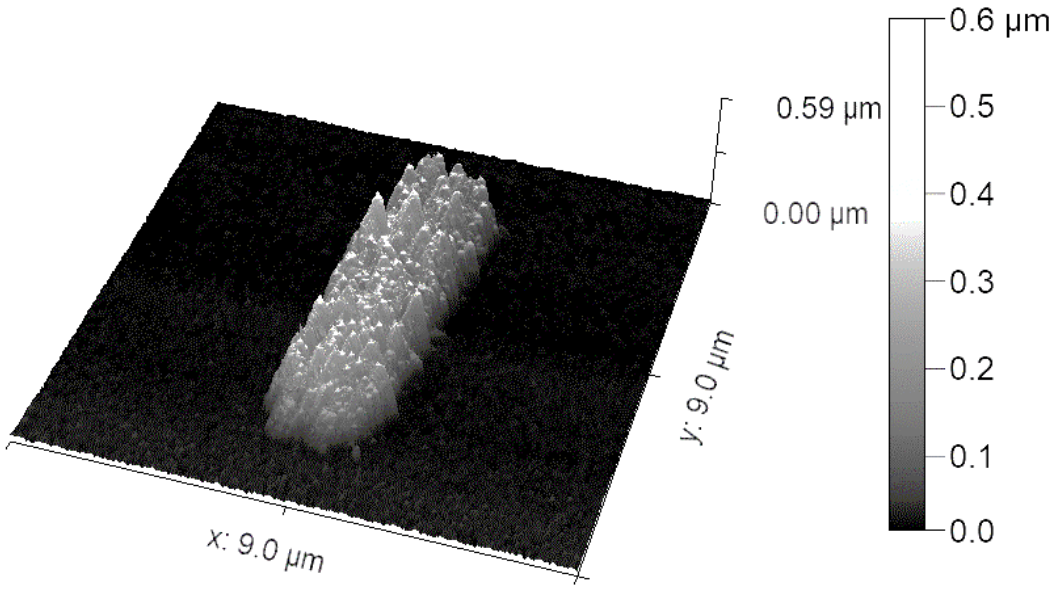

Figure 5.10: AFM image of a larger rectangular micellar structure following 120 min CVD diamond growth at 1250 W and 130 Torr. Average height of the templated diamond is 350 nm.

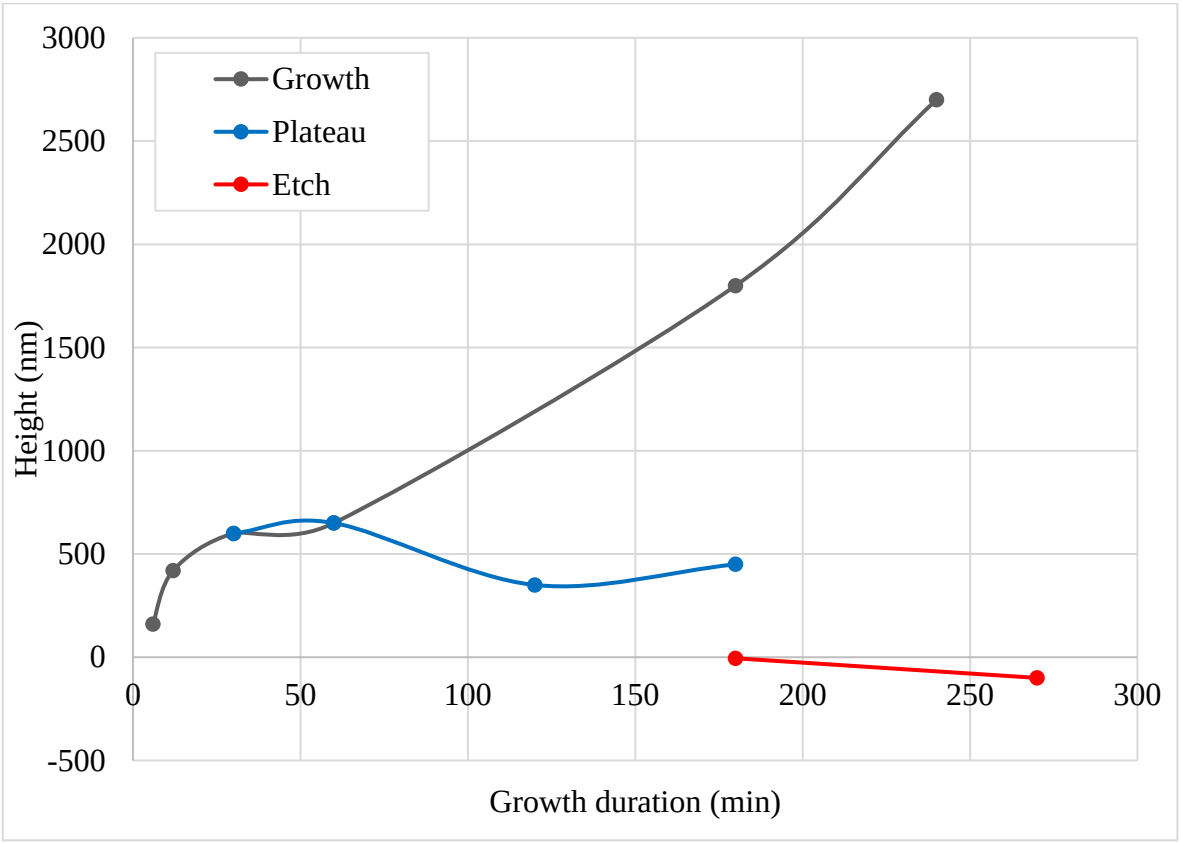

Figure 5.11: Height of templated diamond for a range of durations at 1250 W, 130 Torr, measured by AFM. Across samples, three distinct behaviours were observed as growth duration increased, separated here into three data series; the lines added are for clarity of the groupings that are discussed further in 5.5.5.

5.4.6 Effect of CH_4 concentration and substrate temperature on micelle growth

A larger experimental set was carried out to explore the effect of CH_4 concentration and the temperature of the substrates while keeping the MW power and pressure constant. The temperature was varied using spacer wires of 25-200 µm in diameter, as well as no spacer wire, which allowed for the temperature to be changed without causing significant change to the growth plasma itself. The methane concentration was varied from 1-10% of the total gas flow. Durations of 3-60 minutes were performed for each of these variables.

Table 5.1 presents all the parameters used for this set of growths; Figures 5.12 and 5.13 show the effect of the methane variation set – presented as both duration against height and CH_4 concentration against height – and Figure 5.14 shows the effect of temperature on growth.

Table 5.1: Values used for the various parameters in both the conversion and growth steps for diamond CVD performed for Section 5.5. The range of growth durations is in bold.

Conversion	
MW power (W)	950
Gas pressure (Torr)	110
Duration with CH_4 (min)	1
Duration after CH_4 stopped (min)	2
CH_4 in H_2 (%)	4
Spacer wire (µm)	0
Growth	
MW power (W)	1250
Gas pressure (Torr)	130
Duration with CH_4 (min)	**3, 10, 20, 40, 60**
Duration after CH_4 stopped (min)	2
CH_4 in H_2 (%)	4
Spacer wire (µm)	0
Parameters when varied	
CH_4 in H_2 (%)	1, 2, 4, 6, 8, 10
Spacer wire (µm)	0, 25, 50, 100, 150, 200

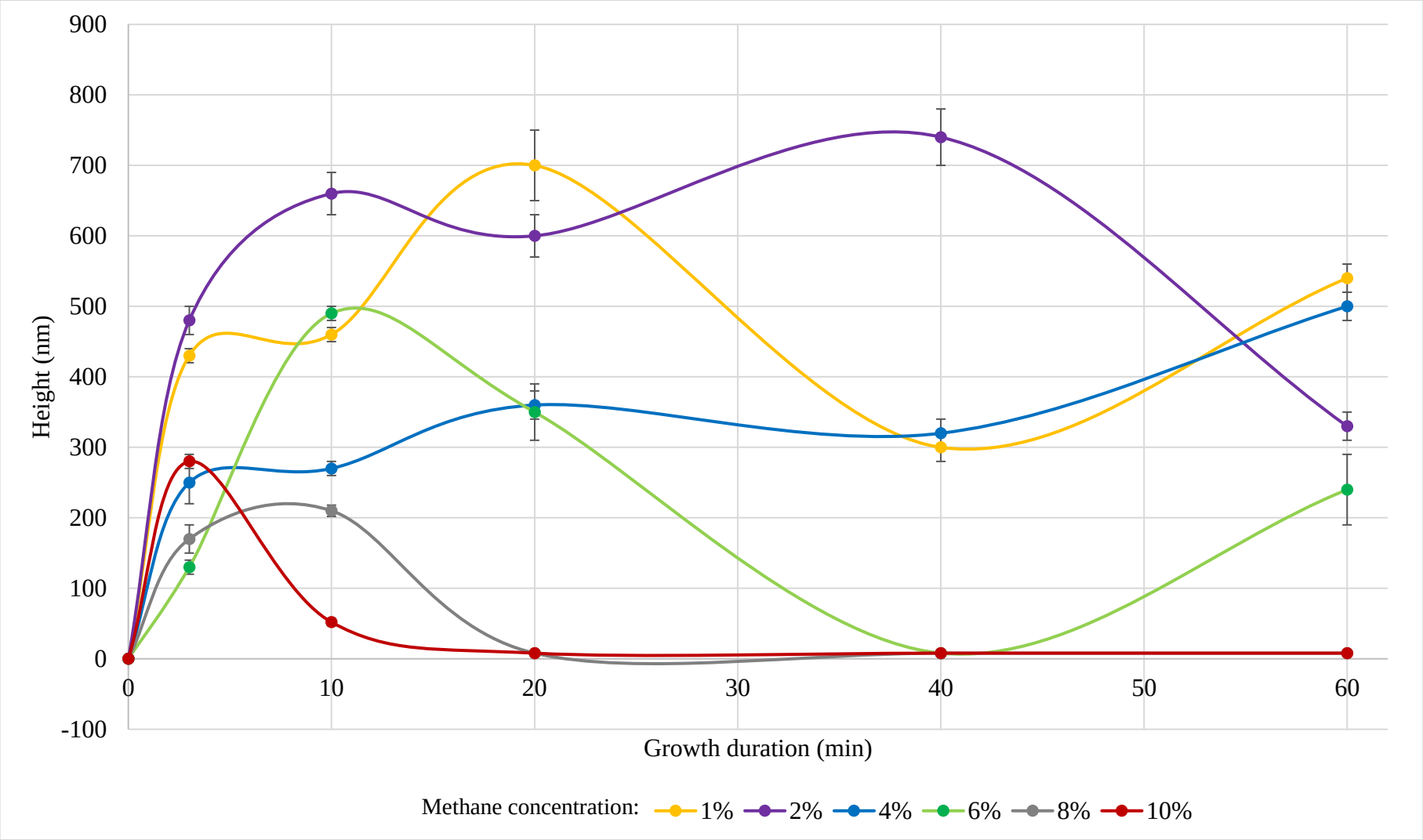

Figure 5.12: Heights of templated diamond for different growth durations, with each series showing a different CH_4 concentration. Growth was carried out at 1250 W and 130 Torr. Heights measured by AFM.

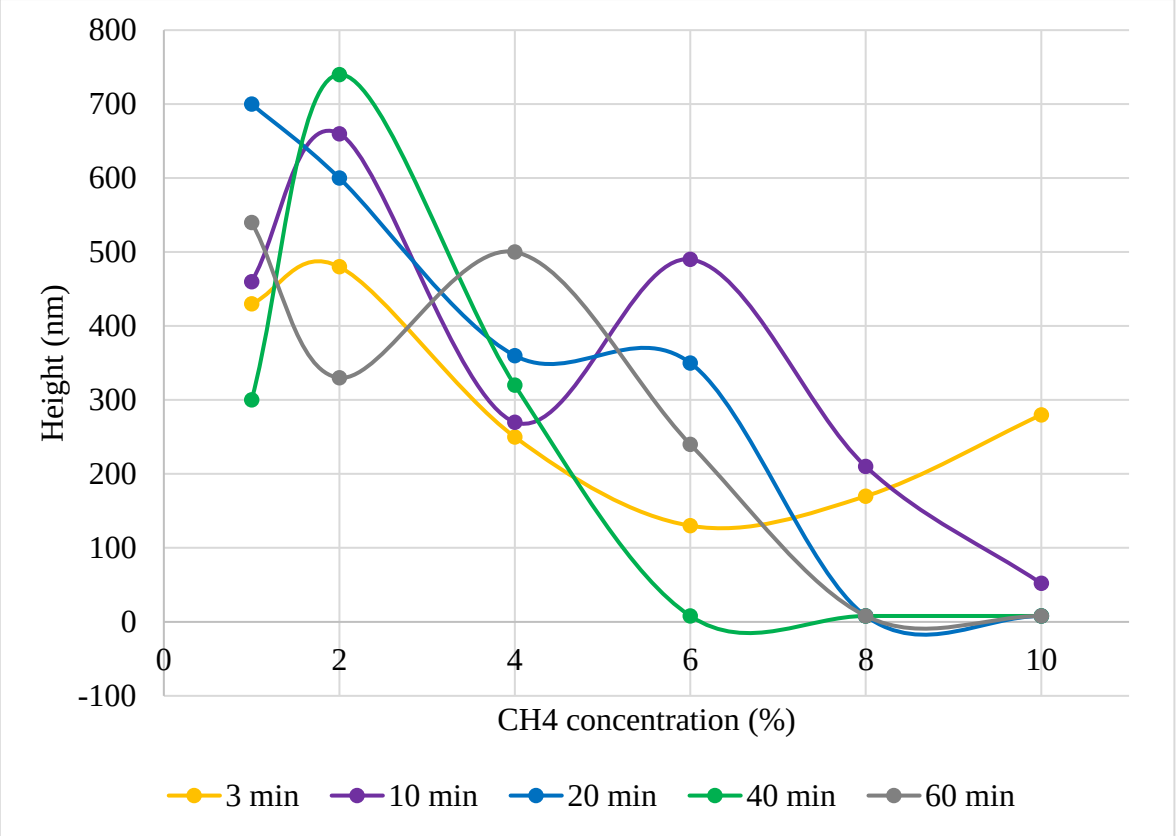

Figure 5.13: Heights of templated diamond for different CH_4 concentrations, with each series showing a different duration. Growth carried out at 1250 W and 130 Torr. Heights measured by AFM.

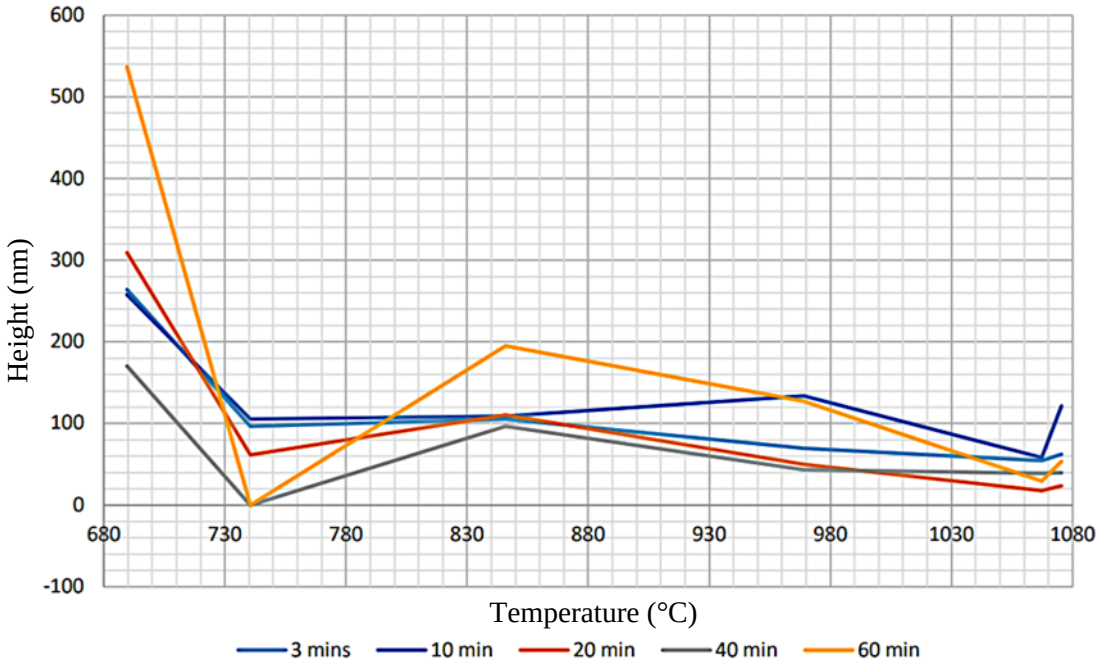

Figure 5.14: Heights of templated diamond for different temperatures, with each series showing a different duration. Growth carried out at 1250 W and 130 Torr. Heights measured by AFM.

5.5 Discussion

5.5.1 Preliminary growth

In order to aid diamond nucleation, initially nanodiamond was thought to be necessary. For this, Si was fluorinated using the method in Section 2.5.2, to allow any nanodiamond not adhered to micelles to be washed off easily. Using the fluorine-terminated Si, deposition of 2D circular platelets (~1.5 μm diameter, 15 nm thick) followed by a nanodiamond solution was performed *via* drop-casting, with the sample washed in MeOH to remove any nanodiamond that had not adhered to the micelles. Following diamond growth in a hot-filament reactor for 20 min, the micelles were observed to have grown into pillars of diamond ~100 nm tall (and been converted to diamond or diamond-like carbon), while retaining approximately the same diameter as the initial micelles, as shown in Figure 5.3. These results were promising enough to warrant further investigation.

Subsequently, due to Ta residues being dispersed over samples when the filaments snapped making AFM difficult to perform combined with the relative lack of control over the HF reactor conditions, it was decided that future growth would be attempted with the MW reactor instead. The Ta residues had been a persistent issue when doing AFM, as they would damage the tip of the cantilever, reducing the resolution of the images. Upon repeating the experiment and obtaining comparable results – albeit with a much shorter growth duration of 5 min due to the much higher growth rate in the MW reactor – it was decided to attempt to grow on the micelles without the nanodiamond "seeding", and without the need for fluorine-terminated Si.

Initial growth runs on 2D rectangular micelles found that they would etch away before any significant diamond growth could occur, so lower temperatures (~500°C) were tried. These produced no growth, but the micelle template did not etch, but had visibly changed form from the BCP micelle into an array of tiny crystals. Using these templates, growth was then attempted at higher temperature conditions (600°C) and significant growth of templated diamond was observed to occur. These three stages are shown in Figure 5.4, and with the low-power step found to be effective at "converting" the micelle into a suitable diamond nucleation site, this conversion step was added to future growth procedure.

Some further investigation into the conversion step was then performed. A range of MW input powers (700-1100 W) and gas pressures (70-110 Torr) were used, with 5 min duration being used. To maintain a substrate temperature of ~500°C (as determined by one-colour pyrometry),

as MW power was decreased, pressure was increased – *i.e.* 700 W, 110 Torr and 1100 W, 70 Torr made up the extremes of this scale. From these, it was seen that the higher pressure resulted in less etching of the sample (which otherwise causes issues with AFM measurement), and that higher power gave better coverage of the substrate.

Hence, the "standard conversion conditions" used for future experimental work was 950 W, 110 Torr for 5 min with a gas mixture of 4% CH_4 in H_2.

Using these conditions consistently produced a well-defined template of the initial micelle as nano-scale grains of a nanocrystalline carbon-containing material well suited for diamond nucleation. Given their size, it was not possible to determine the exact composition of these crystallites, but energy-dispersive X-ray spectroscopy (EDX) was able to show that no significant quantity of Fe (from the PFS) remained; prior to conversion, 0.6% of the structures were identified as Fe, which dropped to 0% after growth. These EDX spectra are included as Appendix B. This suggested that the material had indeed chemically converted from the original micellar materials, as if it was simply pyrolysis, the relatively abundant initial quantity of Fe would have been maintained. Raman spectroscopy was also unable to observe anything other than the Si handle wafer, as any signals from the converted micelles were lost within the noise. At the temperatures measured (~500°C) for these conditions, it is likely that these grains were highly graphitic, probably diamond-like carbon, or possibly nanocrystalline diamond (NCD) or ultrananocrystalline diamond (UNCD).

5.5.2 Effect of temperature on micelle growth

Having established that growth could be performed with good reproducibility, the first area to be developed further was to vary the temperature in order to see the impact on the growth rate. For this, it was decided to continue to explore the lower-temperature region (500-650°C) for growth, as this would allow the reactor chamber to remain sealed between the conversion and growth runs; otherwise, the chamber would need to be opened to add a spacer wire between the W disk and the reactor baseplate, adding potential for contamination. While this known to be below the standard temperatures used for diamond growth (800-1000°C), it was anticipated that some growth would still be observed albeit at a much lower rate, limited by the comparatively high activation energy involved in the diamond growth mechanism [18]. This was actually considered advantageous, as too much growth would result in the height of the

structures reaching (and possibly) exceeding the templated width, which could impact growth rates.

Figure 5.5 shows the results that were obtained for the heights of the templated diamond, measured by AFM, at a range of growth temperatures. These samples were grown at ~130 Torr for 3 min, with the MW power varied to yield the desired temperatures.

These results were quickly seen to be in implausible and thus possibly erroneous – the trend presented suggested that increasing temperature resulted in an exponentially increasing growth rate. For the highest temperature (640°C), the growth rate was determined to be 280 nm min^{-1} over the growth duration, which would equate to a growth rate of 16.8 μm^{-1} – approximately 3× the growth rate usually observed for growth at 800°C and far higher than expected for this temperature. This indicated that the grown material was likely to be highly graphitic or that such a growth rate was not sustained for any period of time more than the first few minutes of nano-crystalline growth, given that this did not agree with previously observed growth rates on other materials at higher temperatures.

Having observed an unexpected exponential growth rate trend of the templated diamond, the next experiment was chosen to test this. A series of increasing duration growths was carried out, this time retaining a constant temperature of 605°C, the results of which are shown in Figure 5.6. The grown diamond structures retained the templated shape well, with a SEM image of one sample (20 min growth) shown in Figure 5.7.

Initially, growth was rapid, with substantial templated diamond produced within the first 20 min. However, this rate then decreased to a near-plateau before increasing again after a significant duration of growth.

As soon after this trend was observed, an important realisation was made: the power used for each run varied considerably between samples, being adjusted to get the substrate temperature to the desired 605°C. For the time-variation set, all growths aimed to be at 605°C, and in doing so, the MW power varied from 1125 to 1320 W – a 15% variation.

At this point, it became apparent how flawed one-colour pyrometry was in this situation. The temperatures being used were at the lower limit of the operational range of the apparatus, and the means of detection – the amount of 2.2 μm-wavelength light emitted from the surface of the substrate – would likely be affected by even small variations in surface coverage, especially when the detector was at the limit of its range.

These flaws effectively negated any useful information from the experimental sets themselves, as the temperature values were fundamentally unreliable, but one very useful trend was observed. Figure 5.6 shows both the height and the width of the templated diamond, where the structure grows outwards at a very similar rate to the vertical growth, the width maintaining ~0.5 µm more than the height, reflecting the initial micelle being ~0.5 µm wider than it was thick. Over longer durations, the width increases slightly faster than the height, but not significantly so.

While not unexpected, it was useful to gain firm evidence showing that the growth rate was similar in both the horizontal and vertical directions, establishing some control over the templated diamond in 3-dimensions, rather than just being able to grow vertically. By modifying the initial micelle dimensions to accommodate for the growth, a huge range of shapes and sizes could be achievable.

5.5.3 Effect of MW power on micelle growth

With a new appreciation of the necessity of reliable parameters, a repeat of the first data set was performed, this time using MW input power as the independent variable as this was controllable to a high reliability, shown in Figure 5.8. To further reduce parameter variation, the growth pressure was set at 130 Torr for all runs. Temperatures were still measured *via* pyrometry, but now only used as a more qualitative guide. Additionally, after the 3 min growth duration had elapsed, the MW power and pressure would be immediately set to 1000 W and 100 Torr, respectively. This was done to provide an additional reduction in variability, with the 2 min of "cleaning" occurring in as near to possible identical conditions for all samples, regardless of the growth conditions used. This also gave a reference temperature for a set condition, which allowed for an adjustment to be made for each sample, yielding a somewhat more reliable temperature estimate for each growth.

Figure 5.8 shows the results for the power-variation experiment, showing a much more expected trend than the previous temperature-variation plot. At low powers, as anticipated, little growth occurred, with the substrate temperature (~500°C) still well below standard temperatures. The quality of diamond was generally poor, with the sp^2 graphitic carbon not being fully etched away by the plasma, causing smaller diamond grains to form with a larger portion of sp^2 grain boundaries. As power increased, the substrate temperature increased, leading to increased deposition rates, while still being too low power to fully etch the graphitic

carbon, hence the peak at 1250 W. At powers above 1250 W, the temperature (> 630°C) was beginning to be sufficient to etch the sp^2 carbon more effectively, causing the templated diamond growth height to reduce but actually resulting in higher quality diamond.

From this, the highlighted input power of 1250 W was chosen for use in future work, due to it providing the highest growth rate. This was mostly beneficial for subsequent AFM analysis, where having a larger structure made the details much easier to resolve, even though the diamond was not of high quality. The main impact of the poorer quality was in the diamond grains being smaller, but this also had the benefit of helping the templated diamond to retain the template shape.

Additionally, the temperatures shown follow a more expected trend, suggesting that the reference condition of 1000 W and 100 Torr allowed for much better estimates of the substrate temperature than before.

5.5.4 Optimisation of the conversion step

The conversion step caused, along with the conversion of the micelles, large amounts of minor etching to the exposed surface of the Si. While this etching was not detrimental to diamond grow, it would cause substantial damage to the tips when undergoing AFM as well as noise on the measured profiles. As such, the conversion step was re-assessed to see if similar growth could be achieved using micelles converted for a shorter duration, as this would reduce the etching of the Si wafer, and hence improve AFM data quality. In order to test this, it was decided that conversion should be followed by growth, to ensure the growth was not significantly affected. Figure 5.9 shows the results of this, with samples being converted for 1, 3 and 5 min, then growth performed for 3 min at 1250 W and 130 Torr, along with one sample that had not been converted prior to growth. The 3 min conversion sample was not measured *via* AFM, as the 1 min conversion showed much less surface etching while not reducing the growth significantly, and thus had achieved the aim.

Subsequent conversion for both the time and broader parameter experiments used 1 min conversion duration.

5.5.5 Growth over varying duration with constant power and pressure

With far more control over growth parameters established, the effect of growth duration was reassessed. This time, the parameters were all maintained at 1250 W and 1300 Torr, with durations ranging up to 270 min. The micelle samples used for the previous experiments had run out, so for this set, given the longer durations planned, templated micellar structures composed of larger rectangular platelets were used instead. These structures were ~6 μm long, ~2 μm wide and ~15 nm thick. An example AFM image of one of these larger micelles after 120 min diamond growth is shown in Figure 5.10. The heights for the set, as can be seen in Figure 5.11, show some unexpected trends.

When analysing the AFM images for these samples, three distinct trends became apparent: some of the micelles grew in a relatively unsurprising way, continuing to grow steadily as duration increased; others seemed to plateau at ~500 nm height; and in the outline of the micelle template, etch pits were observed on the longer growth runs. These three trends were observed over a sizeable number of templated diamond structures across the sample set, with all three visible on the sample grown for 180 min.

The trends can be explained. For the steady growth – as diamond CVD conditions were constant, the templated diamond continued to grow, in much the same way as a diamond film would. The other two trends were thought to be related to the way in which MW diamond growth occurs. The plateaus were observed near to either a larger structure or an etch pit. This suggested that during growth, once one templated diamond had outgrown those near to it, it protruded slightly higher into the plasma, both drawing more of the plasma towards it due to slightly increased electric field strength at the edges and corners of the features, and slightly increasing the temperature it experienced, causing it to grow even more rapidly. This led to a preferential growth loop, with the taller templated diamond structures growing faster and faster, while those around them experienced less exposure to the reactive radicals in the plasma, and lower temperatures, effectively slowing their growth.

Eventually the templated diamond would reach a large enough size that it would delaminate, releasing from the surface and suddenly leaving a hot-spot below it with the same dimensions. This zone would rapidly be etched by the plasma, causing the etch pit. Additionally, with the larger structure now removed from that location, the next tallest templated diamond would then undergo the same cycle. This model was supported by the reduction in the distribution of larger structures on the longer-duration samples coinciding with increasing numbers of etch pits.

5.5.6 Effect of CH_4 concentration and substrate temperature on micelle growth

With significant investigation of the effect of MW power on the growth of the templated diamond, two other significant parameters were selected to be explored in depth. These sets were chosen partly to produce substantial quantities of data for undergraduate student projects, with such a broad scope allowing each to look at a different set of parameters independently. For both sets, conversion and growth parameters remained constant except for the single variable being tested. As such, the conditions were as shown in Table 5.1. The parameters chosen were CH_4 concentration in the gas mixture and substrate temperature controlled by spacer wires.

CH_4 concentration is known to impact both growth rate and morphology, with lower concentrations usually resulting in slower growth, but of higher quality and larger grain size. For simplicity, CH_4 concentrations are presented as % CH_4 in H_2, but experimentally the concentration was varied by increasing or decreasing the flow rate of the CH_4 and keeping the H_2 constant at 300 sccm. While this did result in a slight change in the overall flow rate of gases into the reactor between runs, the variation in total flow from the lowest (1%, 3 sccm) to the highest CH_4 concentration (10%, 33 sccm) was 10%, this was deemed sufficiently minor to be acceptable.

Following previous work finding issues with reliance on temperature measurements, this parameter allowed for another angle on this issue. By using a spacer wire between the cooled reactor baseplate and the disk holding the substrate, the samples could be thermally decoupled, with the ability of the disk to conduct heat to the baseplate reduced. The extent of this decoupling related to the thickness of the wire: the thicker the wire, the more decoupled the system and hence the higher substrate temperature. This technique of controlling the substrate temperature required no adjustments of the plasma itself, allowing for conditions within the plasma to remain as near to constant as possible across the entire experimental set. However, the addition of the spacer wire between the conversion and growth steps necessitated opening the reactor, which had previously been avoided. To ensure any impact of doing this remained consistent across the set, both experimental sets had this step added, even when no spacer wire needed to be put into the reactor.

Additionally, to minimise variations in the reactor conditions resulting from other users, both experimental sets were grown consecutively with no others usage of the reactor occurring between runs. “Chamber conditioning” runs were performed at the start of each day to ensure

the starting conditions were consistent for all samples done that. These efforts were made so that samples from anywhere in the experimental set could be compared with each other, reducing the likelihood of run-to-run variation.

Figure 5.12 shows the data collected from AFM images by M. Standen for the CH_4 set [19]. The lack of data available for most of the samples grown in 8 and 10% CH_4 in H_2 is notable, where no templated diamond structures were found after 10 min of growth for either condition. In lieu of these, the height of the converted micelle (8 ± 2 nm) was used for the plot. This indicated that these structures could have etched completely without growth, which seemed likely as the observable structures were smaller after 10 min than they were at 3 min. However, this could also indicate some release mechanism.

The initial growth for all samples was consistently rapid, with a general trend of lower CH_4 concentrations giving a higher growth rate, counter to expectations. However, by 20 min of growth, the lower concentrations (1, 2 and 4%) had plateaued, although they continued to fluctuate. Meanwhile, those at higher concentrations (6, 8 and 10%) began to decrease in height, with all three sets having at least one sample that had no observable templated diamond structures on it. This could have been due to etching, but with no significant etch-pits, the cause of this remains uncertain.

Additionally, there appeared to be a moving peak corresponding to the plateau height for each concentration, starting at 20 min on the 1%, and slowly moving to lower heights at shorter durations, ending between the 3- and 10-min data for 8% and approximately at the 3 min datum for the 10%. The cause for this is also uncertain, and worth additional research.

Figure 5.13 presents the data in an alternative way, with CH_4 concentration presented as the independent variable. This showed a sustained decrease in growth height as CH_4 concentration increased, counter to expectations and previously published work [20,21]. However, given the growth temperature (~700°C) being below standard growth temperatures, this may have accounted for the change. With growth and etching normally in a careful balance, being outside of the normal growth window could have meant that diamond growth was occurring slower than the rate of diamond etching, with the initial growth being rapid highly graphitic growth from the converted micelles.

The fluctuations seen in both may be due to localised overgrowth resulting in etching, with this effectively cycling over time. However, this effect could be due to cycles of graphitic carbon etching, causing the plasma to become more carbon-rich, and subsequently contain more C and

CH species, in turn, causing graphitic growth to speed up again, with the samples effectively capturing snapshots of this effect occurring over the course of minutes.

These results suggest that these templated diamonds do not behave the same as a large area diamond film, with some fundamental mechanisms behaving counter to behaviour for films. The absence of the structures at the longer durations for higher concentrations suggest the rate of etching is much higher here than for films, which could be due to the much greater exposed surface area compared to a diamond film.

This experimental set would benefit from additional testing at a higher temperature (800-1000°C), to see if the same behaviour is exhibited at more standard growth temperatures.

Due to the analysis of these samples being performed by a number of different undergraduate students, the generated data were of a limited reliability, having been determined in a range of ways [22,23,24]. However, the combined plot of their data shown in Figure 5.14 presents averaged values, and hence conclusions can be drawn with some certainty.

Low temperature (~700°C) growth conditions have the highest amount of growth of all, likely due to rapid graphite deposition without being etched. As substrate temperature increased with increasing spacer thickness, growth decreased with the increasing etching occurring removing the graphitic carbon, while the diamond growth rate remained low. However, as temperature increased further, the substrate reaches standard diamond growth conditions, providing surface conditions well suited to diamond growth; adsorbed particles are more mobile, and with increased surface migration, atoms are more able fit into the lattice and propagate growth.

Reaching the maximum temperature (~1050°C) with a 200 µm diameter wire, the growth rate drops again, with thermal desorption reducing the number of carbon atoms able to migrate. This results in further graphite production as the reactive species in the plasma shift towards smaller C and CH.

These trends are similar to those observed for normal CVD diamond films using nanodiamond seeding, but in an accentuated form. The lowest temperature is too low for diamond growth to occur optimally, with large amounts of graphitic sp^2 carbon being deposited instead. Once the temperature is high enough, there is sufficient energy for the sp^2 carbon to be etched.

Lateral growth rate is also significant. For a film, this has little impact, because the seeding very quickly grows up enough to fill in any spaces, making one continuous film and protecting the sides of the diamond from etching. However, unlike films, the discrete templated structures

remain exposed at the sides, meaning that at higher temperatures (>880°C) the etch rate increases to being above the lateral growth rate. This limits the size of the structures and causes the vertical growth rate to slow, as significant amounts of the material deposited etches away too quickly.

The AFM images also reflect the changes in the quality of the diamond. At both the lower temperatures and the highest temperature, there are more artefacts in the images, resulting from the graphitic material breaking off on contact with the AFM tip.

5.6 Summary and conclusions

Diamond has been grown using BCP self-assembled micelles as templates, representing a novel method to create diamond nanostructures with control over the shape and size. While the majority of samples grown were at lower-than-standard temperatures – resulting in significant graphitic content – high quality diamond has been achieved as confirmed by Raman spectroscopy.

From the preliminary work developing the conversion step, to assorted experiments exploring various parameters and their impact on the growth, the foundations for a promising technique have been laid out.

These templated diamonds have also allowed many of the parameters of diamond thin film growth to be examined from a different perspective, often producing trends that are unexpected, and some counter to established theory. This is likely due to the differences between growth on a film and over the tiny area of the micelles, but with further experimentation, templated diamond could offer invaluable insight into diamond growth mechanism.

5.7 Future work

As suggested within the work, there is ample scope for further experiments to analyse the parameter space of diamond growth.

Repeating the CH_4 concentration experiment at a higher temperature would offer insight into whether the observed trend is simply due to the temperatures used, or if this is representing an unexpected deviation from theory.

Additional parameters should be explored, with pressure and N_2 concentration both seeming to be ideal opportunities to further progress this research. Inclusion of B-doping to produce electrically-conductive diamond structures would present a huge range of applications, so would also be worth investigating, especially using longer thinner micelles.

A study of the same micelle over numerous growths would be an excellent development too. This could be performed by adding markers to the substrate, allowing the AFM to return to the same area for sequential scans, which would reduce the possible variation that would result from scanning different structures each time.

References

1 Blanazs, A., Armes, S. P., and Ryan, A. J. *Macromol. Rapid Commun.*, 30 (2009), 267.

2 Hamley, I. *Block Copolmers in Solution: Fundamentals and Applications*. Wiley, Chichester, 2005.

3 Hamley, I. W. *Angew. Chem., Int. Ed.*, 42 (2003), 1692.

4 Schacher, F. H., Rupar, P. A., and Manners, I. *Angew. Chem., Int. Ed.*, 51 (2012), 7898.

5 Mai, Y. and Eisenberg, A. *Chem. Soc. Rev.*, 41 (2012), 5969.

6 Tritschler, U., Pearce, S., Gwyther, J., Whittell, G. R., and Manners, I. *Macromolecules*, 50 (2017), 3439.

7 Boott, C. E., Gwyther, J., Harniman, R. L., Hayward, D. W., and Manners, I. *Nat. Chem.*, 9 (2017), 785.

8 Oliver, A. M., Gwyther, J., Boott, C. E., Davis, S., Pearce, S., and Manners, I. *J. Am. Chem. Soc.*, 140 (2018), 18104.

9 Qui, H., Gao, Y., Boott, C. E. et al. *Science*, 352 (2016), 697.

10 He, X., Hsiao, M.-S., Boott, C. E. et al. *Nat. Mater.*, 16 (2017), 481.

11 Wang, H., Patil, A. J., Liu, K., Petrov, S., Mann, S., WInnik, M. A., and Manners, I. *Adv. Mater.*, 21 (2009), 1805.

12 Zanin, H., May, P. W., Harniman, R. L., Risbridger, T., Corat, E. J., and Fermin, D. J. *Carbon*, 82 (2015), 288.

13 Rivera-Utrilla, J., Sánchez-Polo, M., Ferro-García, M. Á, Prados-Joya, G., and Ocampo-Pèrez, R. *Chemosphere*, 93 (2013), 1268.

14 Hazell, G., May, P. W., Taylor, P., Welch, C. C., and Su, B. *Biomater. Sci.*, 6 (2018), 1424.

15 Nistor, P. A., May, P. W., Tamagnini, F., Randall, A. D., and Caldwell, M. A. *Biomaterials*, 61 (2015), 139-149.

16 Pearce, S. T. *Investigations into the Seeded Heteroepitaxial Crystallisation of Polyferrocenylgermane- and Polyferrocenylsilane-based Polymers in One and Two Dimensions*. Ph.D Thesis, University of Bristol, Bristol, UK, 2019.

17 Brumwell, M. *"Programmable diamond" Utilising Block Copolymer Micelles of a well-defined shape to create 3D diamond constructs with nanoscale resolution*. Extended Project, University of Bristol, Bristol, UK, 2019.

18 McCauley, T. G., Gruen, D. M., and Krauss, A. R. *Appl. Phys. Lett.*, 73 (1998), 1646.

19 Standen, M. *The effect of methane concentration and growth time on the height of individually templated, CVD-grown diamond nanoparticles*. MSci. thesis, Univeristy of Bristol, Bristol, UK, 2021.

20 Li, X., Perkins, J., Collazo, R., Nemanich, R. J., and Sitar, Z. *Diamond Relat. Mater.*, 15 (2006), 1784.

21 Reshi, B. A., Kumar, S., Misra, A., and Varma, R. *Mater. Res. Express*, 6 (2019), 046407.

22 Juszczak, M. *Temperature Dependence of Templated CVD Diamond Growth*. BSc. thesis, University of Bristol, Bristol, UK, 2021.

23 Muthuganesan, S. *Analysis of CVD diamond growth at varying temperatures*. BSc. thesis, University of Bristol, Bristol, UK, 2021.

24 Qiao, S. *An investigation into the effect of substrate temperature and growth time on the height of polmer/micelle-templated diamond using chemical vapour deposition (CVD) method*. BSc. thesis, University of Bristol, Bristol, 2021.

Chapter 6 – Conclusions and future work

6.1 Diamond-on-black silicon as a bactericidal surface

Using a range of sizes and distributions of bSi, D-bSi was successfully grown and proven for its bactericidal properties. Fluorination generally enhanced the ability of D-bSi to kill surface bacteria, although this required suitable D-bSi for the effect to be observed.

Gram-negative *E. coli* and both Gram-positive *S. aureus* and *S. epidermidis* were able to be killed effectively using D-bSi, with the bSi's physical properties being important to allow for suitable D-bSi to be grown. Consequently, D-bSi which was suitable as a bactericidal surface for Gram-negative bacteria was not found to be effective for Gram-positive bacteria. As a result, any bactericidal surface would require a mixture of needle lengths and densities to be effective against all bacteria.

Further research should focus on two main areas: doing additional experiments to determine the significance of the surface patterning on long-term growth; and attempting to find a D-bSi surface that is both effective for Gram-negative and Gram-positive bacteria, potentially using a bSi surface of multiple heights and dispersals of the needles.

6.2 Mixed-size seeding for diamond growth onto GaN and AlN

The seeding method developed was used effectively to produce diamond films with excellent thermal properties. However, due to gallium's inability to form a carbide, these diamond films could not be grown onto a GaN and produce an effective thermal spreading layer.

AlN proved to be a much better growth surface, with low thermal barriers between AlN and diamond films, offering an incredible scope for improvements in modern GaN HEMTs, using a thin AlN interlayer to provide both adhesion and thermal transport between the devices and the diamond.

The next steps would be focused on optimising the diamond growth in order to maximise the thermal transport. Additionally, using an etching method to remove areas of the Si handle wafer

should be explored as this would allow for the AlN-diamond interface's thermal resistance to be measured from the smoother AlN side, which would greatly enhance the reliability of the results. With this, thicker diamond films could be grown, more representative of the films required for industrial devices, without impeding the quality of data available, and would allow for the thermal characteristics of the diamond to be assessed more thoroughly too.

6.3 Using self-assembled polymer micelles as a template for diamond growth

A completely novel method for growing diamond nanostructures using self-assembled polymer micelles was developed and explored. Using this technique, the templates can be made to allow diamond of various shapes and sizes to be made on a scale from 100s of nm to 10s of μm in each dimension.

These structures were then used to explore the parameters of diamond growth. Investigations into the effects of changing MW power, temperature and CH_4 concentration were all carried out, providing insight into CVD diamond growth on a previously unseen scale.

Further work should be pursued in a range of ways. Other growth parameters should be explored, and those which have already been investigated should be explored further with differing sizes and shapes of micelles.

The effect of doping should also be explored. Boron incorporation could enable these structures to form electrically conductive diamond, which would offer unprecedented scope for producing high-surface area electrodes by using a high density of micelles.

Appendix A: Development of a large-area hot filament diamond CVD reactor

A.1 Introduction

A.1.1 Motivation

While the reactors available for use in the University of Bristol Diamond Group are excellent, permitting a wide range of parameters to be varied, they were all very limited in deposition area. The hot filament (HF) reactors can accommodate ~30 × 20 mm on their sample stages for uniform growth, with little ability to use a substrate any larger than this. The microwave (MW) reactor has much more room for samples, with circular substrates of 30 mm diameter easily accommodated, but the actual area for uniform growth was far more limited, with circular samples exceeding 15 mm diameter and square samples over 10 × 10 mm having noticeably poorer diamond growth at the edges and corners.

With the work being done regarding diamond growth onto GaN (see Chapter 4) ultimately aiming to show an industry-viable technique, an important question was presented: could we develop and build a larger-area reactor in-house in order to do CVD diamond growth on an "industry relevant" scale? From speaking to collaborators in the EPSRC GaN-DaME programme, it was determined that a 100 mm-diameter wafer would be the minimum size that is viable for industry to consider, with 150 mm-diameter preferred.

Hot filament CVD is a suitable technique for performing larger-area growth of diamond, given the simple scaling of the method: by using more and longer wires than for a smaller system, growth can cover a larger area. While industrial companies growing large areas of synthetic diamond (such as Element Six [1]) usually utilise microwave plasma-assisted CVD, large-area (200 × 200 mm or more) hot filament systems are available to purchase [2]. However, these systems are sufficiently expensive to be unaffordable without a dedicated equipment grant. Therefore, it was decided to develop a reactor in house, using HF instead of MW CVD due to the comparative simplicity and significantly lower equipment costs.

A.1.2 Thomas Swan reactor and its suitability for modification

At the start of the project, the University of Bristol Diamond Group had a reactor designed by the company Thomas Swan which could deposit diamond on up to 20 wires or fibres simultaneously [4], pictured in Figure A.1. While this reactor had been used for various research projects in the past 25 years, it is no longer needed because research in the group has moved away from working on diamond coated wires made in this way.

This appendix is focussed on the conversion of the Thomas Swan reactor into a large-area HF CVD reactor, while ensuring that the reactor could easily be restored to the old set-up if desired. This apparatus was also chosen due to its large size, which would allow for the potential of up to a 6" (150 mm) diameter wafer to be diamond-coated.

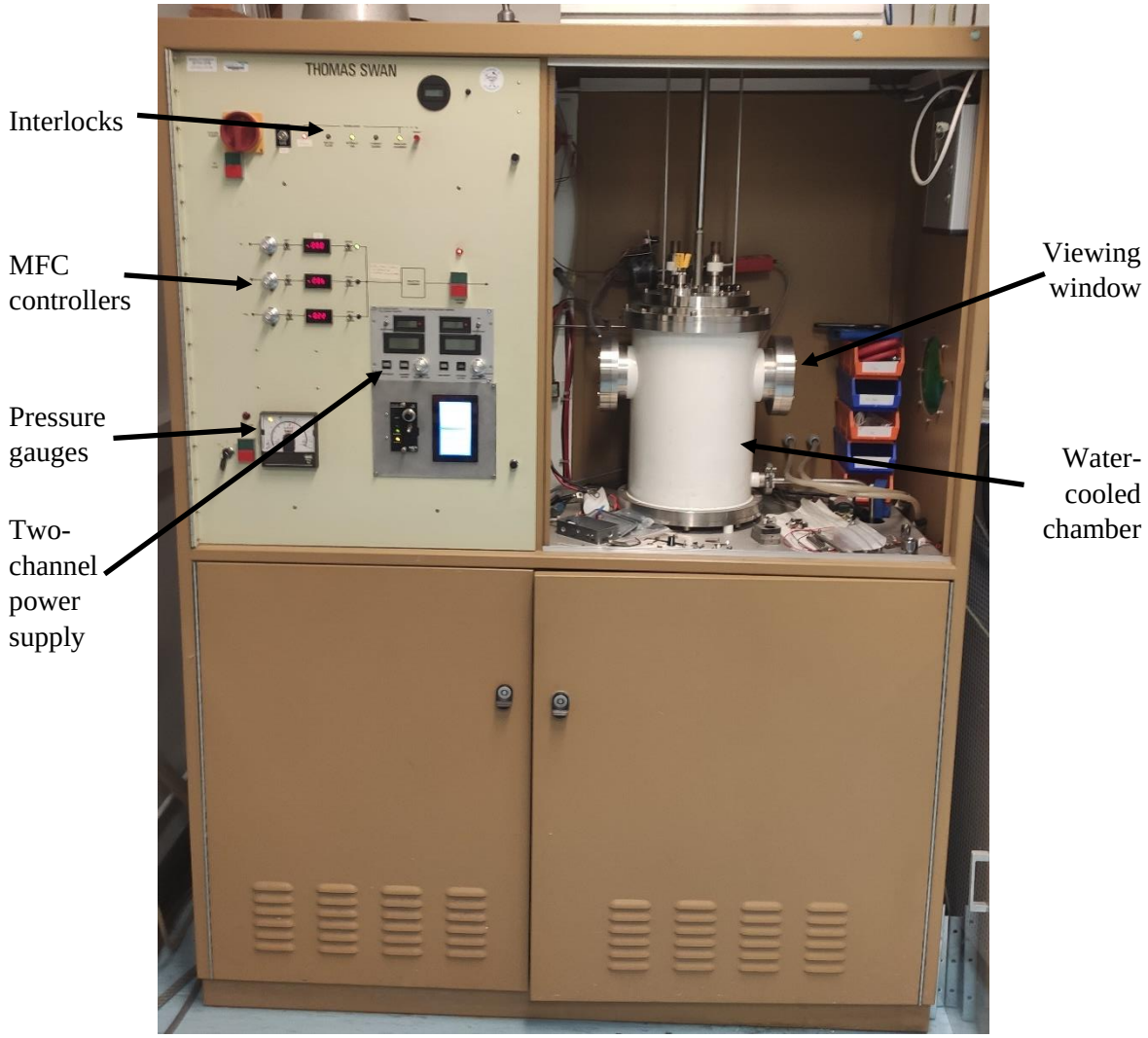

Figure A.1: Photograph of the Thomas Swan reactor after a few modifications had been made. Features from the original Thomas Swan apparatus are identified.

As such, it was considered feasible to carry out this conversion on the limited budget available. One important proviso to this work was ensuring that the pre-existing apparatus could be restored to its original purpose for deposition into wires with minimal difficulty, should this be required for any experimental work in the future. As such, designs could not alter several components of the reactor function. The "lid" of the Thomas Swan could be removed easily, which allowed a replacement lid to be designed to carry an assembly for large-area hot filament growth. With ample space in the cabinet, additional equipment could be fitted where necessary, with the most notable piece of equipment being a much higher power direct-current power supply than was already installed.

A.1.3 Chapter summary

This chapter details the design, construction and testing of a large-area hot filament diamond CVD reactor (LA HF). Herein, "large-area" refers to the area of up to a 150 mm-diameter wafer, ~175 cm^2, although the testing uses smaller wafers for ease. This substrate area is considerably larger than the standard growth areas of on the order of 1 cm^2 that is usable in the other reactors in the Diamond Group.

The design section, Section A.2, outlines the spatial, thermal and material considerations that were made in the design of the new reactor lid. The required conditions to produce a suitable environment for CVD diamond growth are considered, and then suitable materials are determined. This section then makes use of computer-aided design (CAD) to develop the components that would be manufactured to build the new reactor apparatus, and also discusses some of the redesigns and modifications made during testing.

Section A.3 details the modifications to the pre-existing equipment, and decisions made to improve both safety and ease of use.

From there, the reactor was tested, presented in Section A.4. At the end of the experimental work, the reactor was successfully able to grow diamond onto 50 × 50 mm Si wafers, with the further modifications planned to allow for the full-scale growths unable to be completed in time.

Significant assistance was provided throughout by J. Smith, who contributed to the design ideas and helped with construction. The components for the lid that were not readily available commercially were produced by the University of Bristol Mechanical Workshops, and assistance with the electrics was provided by P. Dinham of the UoB Electronics Workshop.

A.2 Designing an assembly for large-area hot filament growth

A.2.1 CVD conditions

Using the smaller HF reactors as a model, parameters for scaling up were determined. Some of these parameters required no changes – it was decided to use the same growth pressure (20 Torr) and the same gas flow rates (2.0 sccm CH_4, 200 sccm H_2). The growth pressure did not need to vary, as this would scale with the size of the chamber to present the same quantity of feedstock gases to the activation, overall producing a similar growth condition. While the gas flow rates may have needed some variation to account for a much larger residence time in the much larger chamber, HF diamond growth can be carried out with a wide range of flow rates and relative reactive species mixtures. As such, this was considered a parameter worth further investigation once testing had progressed, but ultimately was never explored.

For HF, the temperature of the filaments is very important, both providing the activation of the feedstock gases and heating the substrate to ideal growth temperatures. Based on the smaller reactors with 3 filaments made of 0.25 mm diameter Ta, the combined filament length was ~250 mm. These wires were resistively heated by 25 A at ~10 V, as such, with a power of ~250 W. Scaling this up to cover a 150 mm wafer, 16 filaments spaced 10 mm apart and 200 mm long (with 25 mm either end to improve uniformity over the sample itself) equates to 3200 W.

However, the smaller-scale reactors are limited in the duration they can run for due to the carburisation of the filaments. One means to reduce this limitation is by using thicker wires – as such, the wires take longer to fully carburise. However, by increasing wire diameter, the resistance of the wire decreases, so to maintain the same overall power, the current must be increased. Thicker Ta wire was too expensive to be viable, so 0.5 mm-diameter W wire was chosen instead. With the increased wire diameter, combined with W being less resistive – hence requiring a higher current than an equivalent size Ta wire – it was determined that a power supply capable of producing 10 kW at 500 A would be suitable.

The last important condition for HF CVD is substrate temperature. With the heat provided solely by the filaments – which have to hot enough to provide suitable reactive species for diamond CVD to occur – a means of controlling substrate temperature without altering the filament conditions was required. To resolve this, a design featuring some form of variable substrate holder was required.

A.2.2 Practical considerations

Given the very limited budget for this modification, material choices for the bulk of the build were limited to only relatively cheap metals. Stainless steel (316) was chosen for most of the components as it remains structurally strong when at 100s of °C and was a compromise between thermal/electrical conductivity and cost. For the main power input to the chamber, copper feedthroughs were to be used. For the hottest regions of the apparatus – the surfaces facing the filaments and their intense radiated heat – tungsten plates would be used to protect the stainless steel.

In order for the equipment to be both safe and easy to use, other considerations had to be made. While 150 mm wafers were the desired maximum size, the reactor design needed to be adjustable, so less wire could be used when performing growth on smaller substrates. This variability needed to be in both the length of the wires and in the number of wires needed. Additionally, an improved means of loading the filaments was desired, as the technique used for the smaller HF reactors was highly time consuming and would not be practicable on the thicker – and thus less flexible – W wires.

To resolve this, a framework was designed using two stainless steel rods which could be adjusted to move the filament-holding blocks closer together as required.

This method would need some means to tension the wires, as otherwise the filaments would bend with thermal expansion. At ~2000°C, W expands by 5% of its initial length. The simplest remedy for this was to mount the entire array of wires vertically, so any sagging of the wires would be "in plane" and not alter the growth conditions of the substrate. Initially, it was intended for the filaments to be spring loaded, but due to manufacturing limitations, an alternative method using weights to tension the wires was implemented.

A.2.3 Reactor design

Figure A.2 shows a schematic diagram of the entire initial design. The overall design constituted three main sections: the filament assembly, the substrate mounting, and the power coupling through the lid.

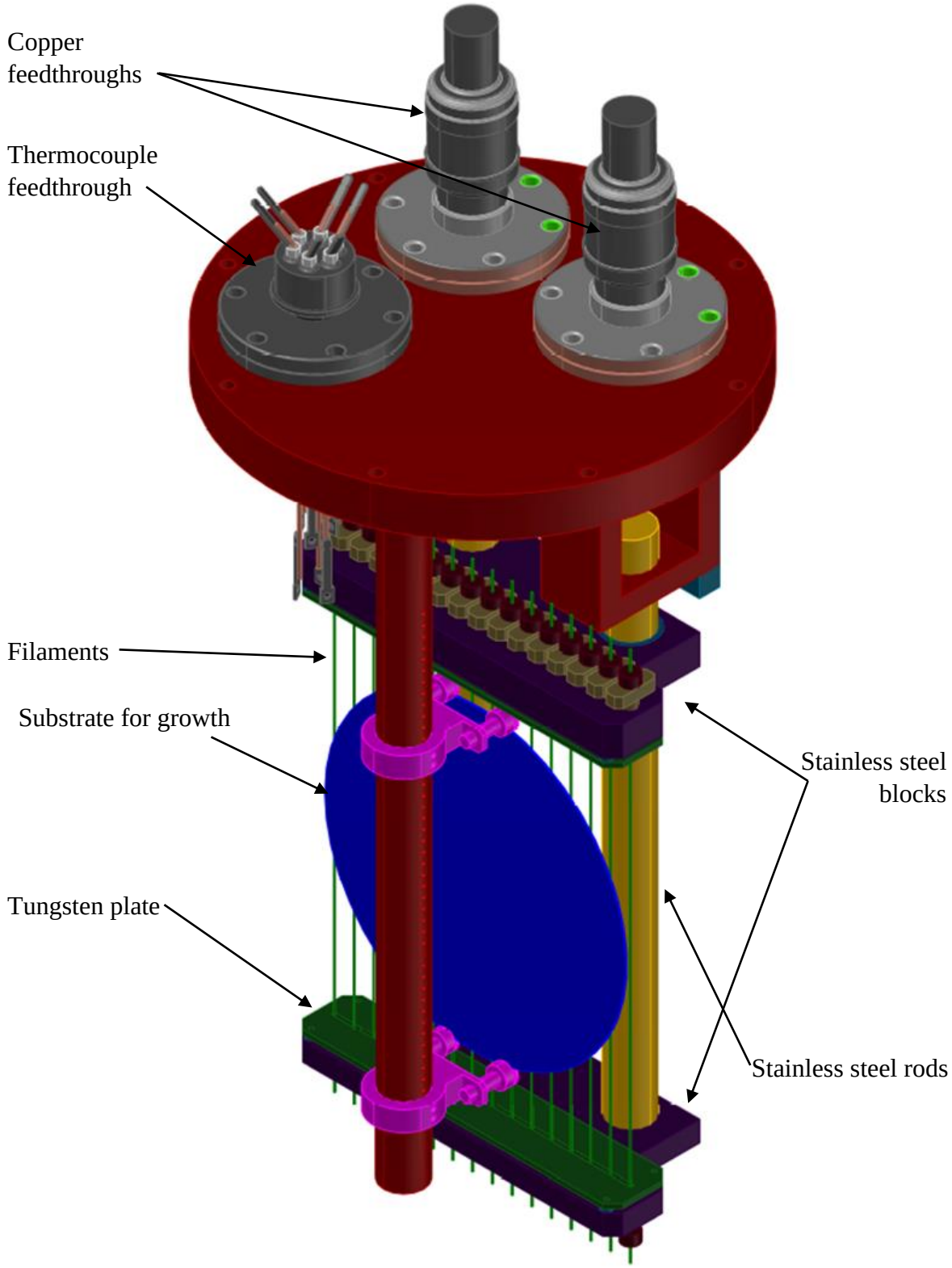

Figure A.2: Complete large-area hot filament CVD reactor design. The Si wafer substrate is mounted vertically facing the filaments, which are held in place by a stainless steel frame. A circuit is formed by the current flowing through the top of the left-hand rod, through the filaments and then out of the bottom of the right-hand rod.

The filament assembly, shown in Figure A.3, was the most complicated component to design, with the need for sufficient electrical insulation provided by ceramic spacers, but the design being adjustable. As such, the filament assembly frame was two 20 mm-diameter stainless steel threaded rods. These provided both structural support and formed most of the electrical circuit.

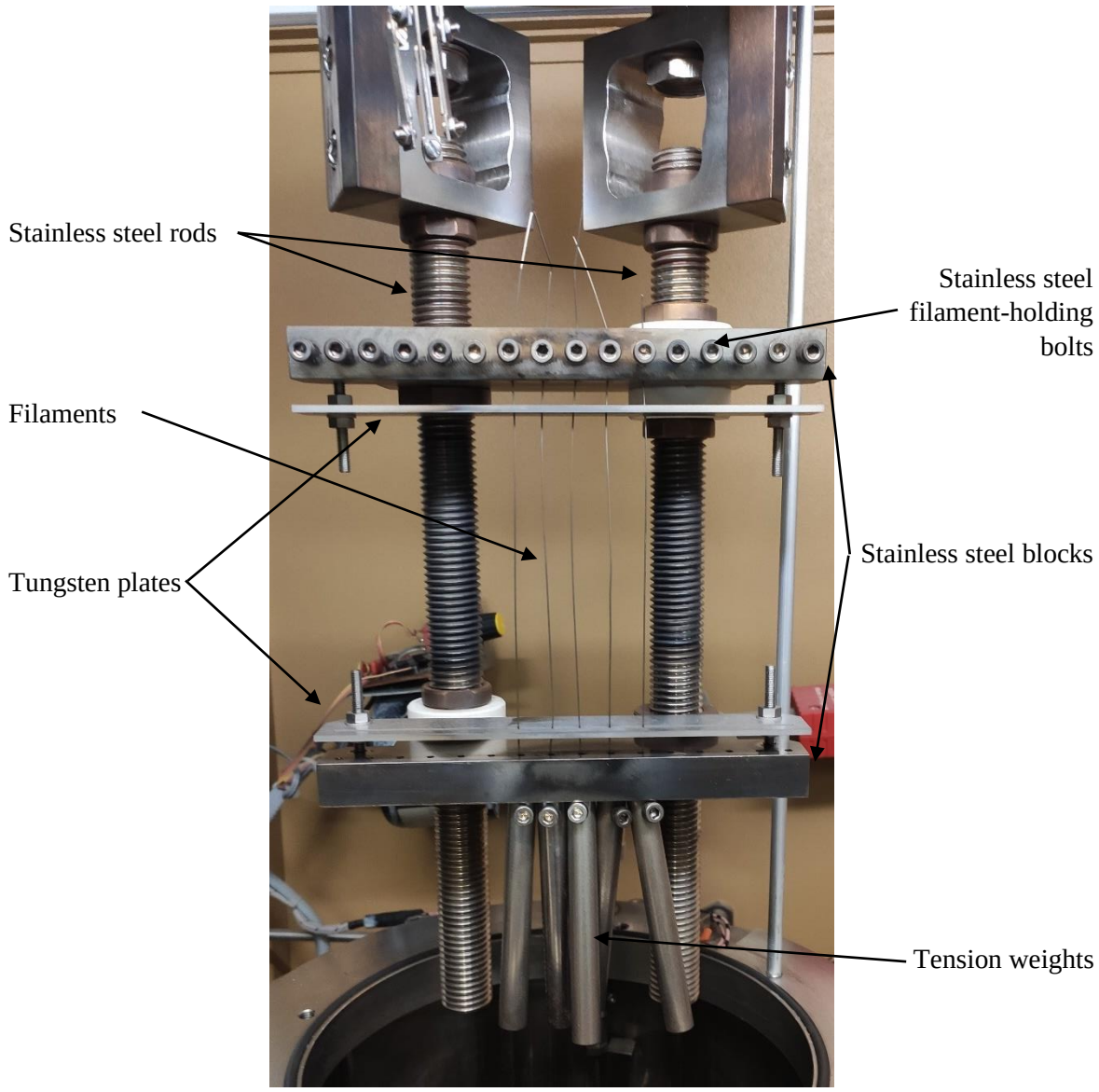

Figure A.3: Photograph of the filament assembly in its final form.

Each of the two stainless steel blocks connected to one of the rods, using copper nuts to provide a good electrical contact, while the other side had a ceramic spacer to ensure that it was insulated. The faces of the stainless steel blocks had a W plate, which were distanced from the plates 10 mm by a pair of titanium-zirconium-molybdenum (TZM) bolts. TZM was chosen for its high melting point (~2600°C) and much easier machinability than W or Mo, making it well

suited for the nuts and bolts; W has a higher melting point (~3400°C), but is very brittle, making it much harder to finely machine and handle without shattering.

In the original design (Figure A.2), the filaments were held in place with a pair of spring-loaded hollow bolts, which would compress to hold the filaments tight. However, these were too difficult to manufacture without specialist equipment, so an alternative design was made. Instead, at the top, the wires would be held in place by a bolt tightening into them – as the bolt was made of stainless steel, as the reactor got hot, the bolt would tighten with thermal expansion. To tension the filaments, a set of tensioning weights were made, designed to be as large as they could without contacting the bottom of the chamber (and shorting out the power supply). These weights would keep the filaments taught as they expand. However, at the bottom there was no tightened connection between the block and filaments; instead, the holes the wires went through are off-set diagonally, so the filaments were pulled against the edges to provide a reliable electrical contact – a schematic diagram of this is shown in Figure 6.4. With filaments fitted between the blocks, the circuit was complete, with the current resistively heating the wires to ~2500°C, while the remainder of the parts remained cool enough to maintain structural integrity.

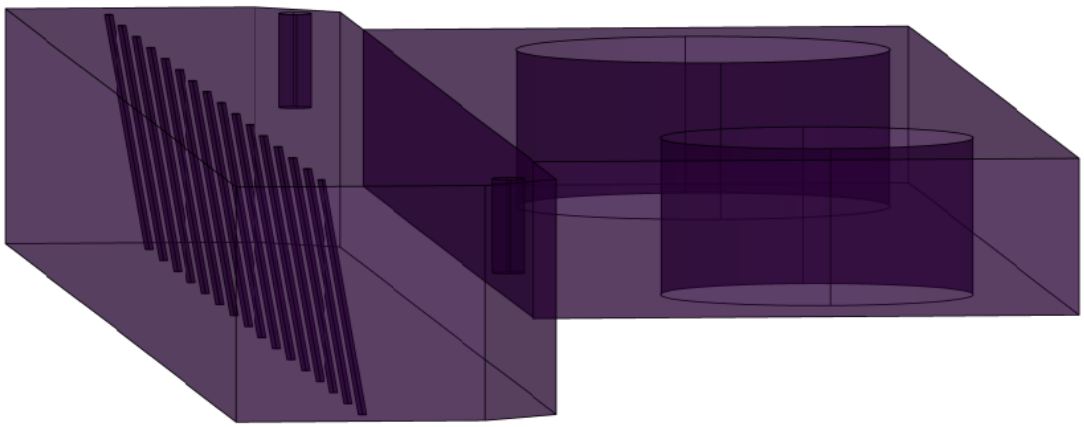

Figure A.4: Schematic diagram of the lower stainless steel block, showing the angled holes to ensure the filaments make a good sliding electrical contact without being fixed in place, this allowing for filament expansion.

This design achieved one of the main objectives – fitting filaments was simple using this design. First tightening one end of the filament to the tension weight, it was then pushed through the lower block and the slot in the lower W plate. At the other end, it was fed through

the other W plate slot and through the upper block, and with one hand holding the top of the filament out of the top, the bolt could be tightened, and the filament was fitted and ready for use. Compared to the procedure for the other HF reactors – where a skilled user might be able to fit 3 filaments in 5 min – this design allowed 10 filaments to be fitted in fewer than 3 min.

Another key design feature was the adjustability for different substrate sizes. With the frame built around a pair of threaded rods, adjusting the separation between the blocks was very simple.

The substrate mounting was, likewise, very simple. A central rod was attached to the reactor lid, into which indentations had been placed along the back. These indentations allowed for a grub screw to hold a substrate holder, which was redesigned after the initial design encountered practicality issues. Both designs are shown in Figure A.5.

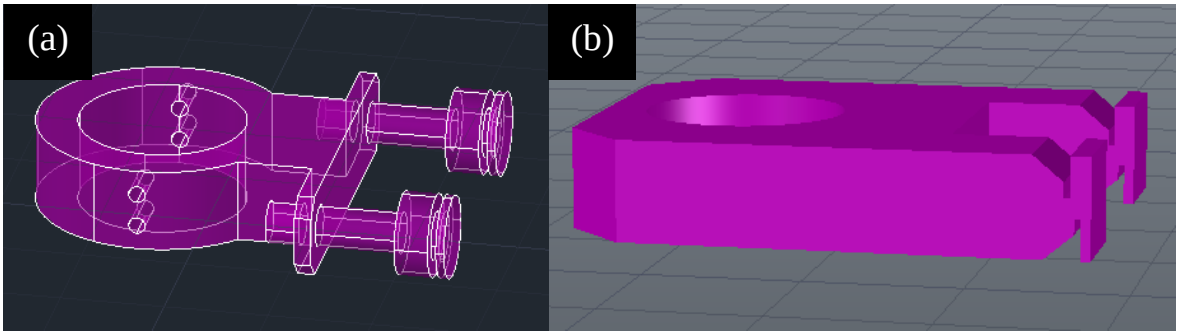

Figure A.5: Schematic diagrams of the substrate holders designed and used. (a) is the initial design using adjustable bolts, (b) is the newer design with fixed separation.

The initial design (Figure A.5(a)) featured a pair of adjustable bolts, which could be used to vary the separation between the filaments and the substrate. On the face of these bolts was a smaller bolt, allowing the substrate to be "pinched" in place. This design encountered numerous issues: the bolts were difficult to align, and following the first growth, they had seized so much that they could barely be adjusted anymore; the smaller bolts were very difficult to work with, given the space between the substrate and the filaments was 3 mm; the "pinching" was easy to accidentally overtighten, resulting in the wafer edge breaking.

As such, the substrate holders were redesigned. The new design (Figure A.5(b)) permitted the spacing between the filaments and the substrate to be either 3 or 4 mm, with one side of each offering each of these. The grooves were designed to be 0.6 mm wide, allowing the 525 µm-

thick Si wafers to fit comfortably without damage, but not loose enough to allow significant variation. These substrate holders were sufficiently easy to make in the UoB workshops that other spacings could be made if desired in future experiments.

Lastly, the lid was designed to allow secure connection between the power supply and the filament array. The copper feedthroughs were connected *via* a joining block to the threaded rods of the filament assembly, with the block bolted to the lid to provide structural strength. While being a simple part, the ceramic used as insulation was liable to crack if anything was overtightened, so great care had to be taken when tightening these bolts.

Initially, the lid had no water cooling, but temperatures during initial testing showed that there was insufficient cooling provided by the water-cooled jacket of the chamber. As such, the underside of the lid had excess material milled out and a plate welded to cover it, leaving a cavity that permitted water cooling to flow through the lid during growth.

A.3 Modifications to the external equipment

In order to facilitate using the new reactor lid, many changes to the supporting equipment were made. First, a pneumatic cylinder was mounted at the top of the cabinet to enable the heavy lid assembly (~10 kg) to be lifted vertically. This also minimised the possibility of any components fouling against the reactor entrance when opening or closing the chamber. This meant that filaments and substrates could easily be fitted *in situ*, with the whole reactor lid attached to the cylinder. This presented a hazard if the chamber was under vacuum when attempting to lift the lid. To prevent this, a key-locked control box was installed, ensuring the pneumatics could not be operated accidentally.

A touchscreen monitor was installed to replace the old pressure gauge readout. This was able to display the pressure to a higher precision than the old unit (which only provided 2 significant figures) but was also designed to simultaneously display temperature readings from the thermocouples and both current and voltage readings from the power supply.

For the much higher power demands of a large-area filament array, a larger power supply had to be fitted. Initially a 125 A, 24 V dc, 3 kW power supply was installed. Testing was performed using this power supply – discussed in further depth in Section 6.4 – but it was identified that the maximum potential difference was only just sufficient for the apparatus. In order to have sufficient capacity, both regarding overall power and voltage available, a larger

10 kW power supply was installed, with maximum outputs of 210 A and 48 V dc. This power supply also featured a “current control” mode which would be better suited to HF CVD than the 3 kW unit. This is because the resistivity of the filaments changes over time as they carburise, so maintaining consistent conditions is more easily achieved as the current does not change. However, due to limitations with cooling the chamber sufficiently, this unit was not tested by the time of writing this thesis.

Several of the interlocks had to be repaired after the many years of the chamber not being used regularly. Alongside this, the vacuum pump was overhauled to return it to good performance, as most of the internal components had begun to degrade.

A.4 Testing of the large-area hot filament CVD reactor

Initial growth runs were performed on 50 × 25 mm Si wafers. This size was chosen as it allowed for several filaments to be used but without pushing the limits of the equipment. These samples were seeded by manual abrasion. Runs were carried out for 1 and 10 h, with both samples exhibiting a growth rate of ~0.5 μm h^{-1} determined by cross-sectional SEM, which is comparable to the growth rate of the smaller HF reactors.

Figure A.6 shows SEM images of the first test, a 1 h growth with only 2 filaments fitted and 10 mm separation between the filaments. Figure A.7 shows Raman spectroscopy (514 nm excitation) data from the same areas. In the area between the filaments, the diamond film has good uniformity, and showed a sharp diamond (1332 cm^{-1}) peak, although this is alongside a sizeable graphitic band. The area of the film from directly beneath a filament showed similar results although there are many pinholes in the film. The diamond growth only becomes visibly worse ~5 mm outside of the area of the filaments, although the film still shows a strong diamond peak. Due to a fault with the current meter, the current was unknown, with the potential difference maintained at 11.3 V.

However, the primary purpose of this run was to prove that the basic design worked and that scaling up could be done. The subsequent 10 h run used 4 filaments each 100 mm long, and the power supply provided an average of 80 A at 11.5 V. This growth run also made use of the improved substrate holders. Figure A.8 shows the diamond from the centre of the 50 × 50 mm wafer, showing excellent diamond growth with large grain sizes, and good uniformity across the sample

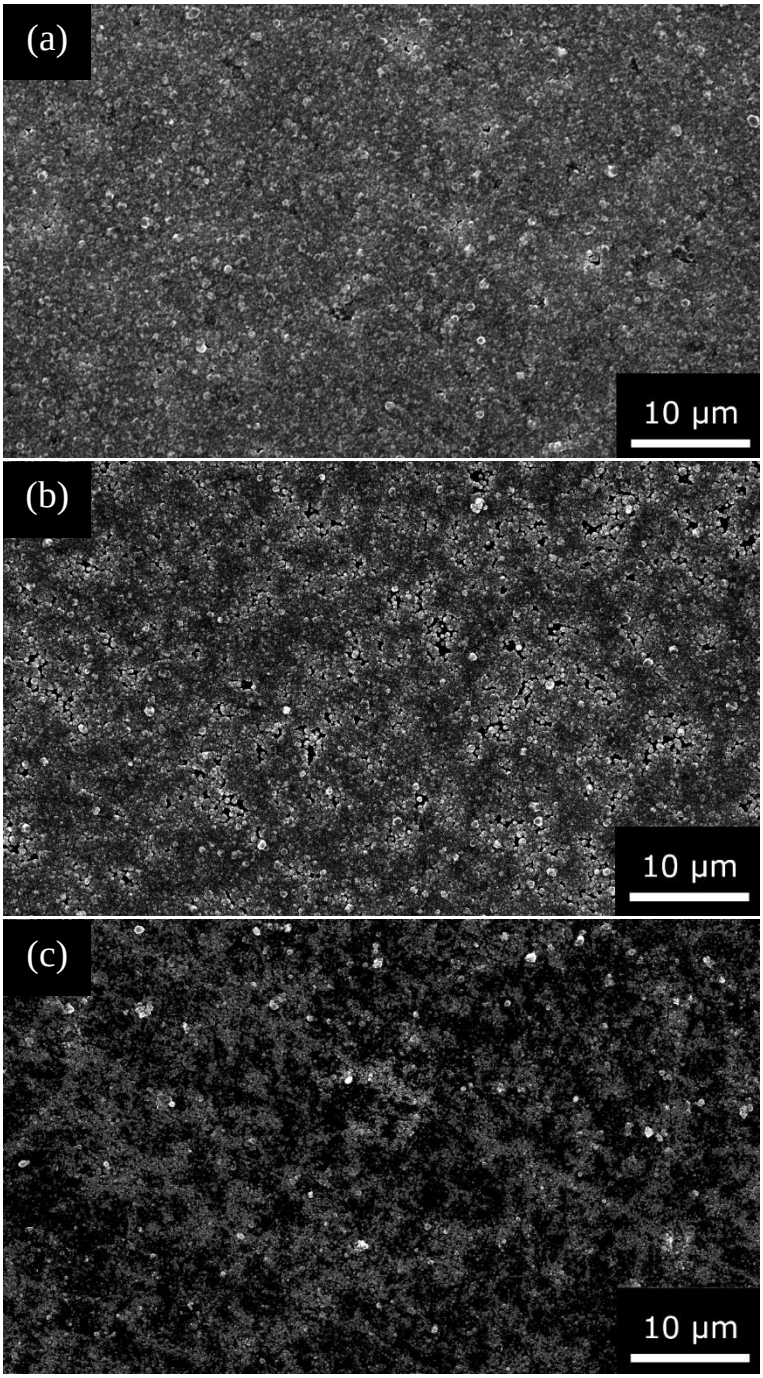

Figure A.6: SEM images of 1 h growth (~1 μm of diamond) with 2 filaments. (a) was from between the filaments, (b) was beneath one filament, and (c) was on the outside of the filaments.

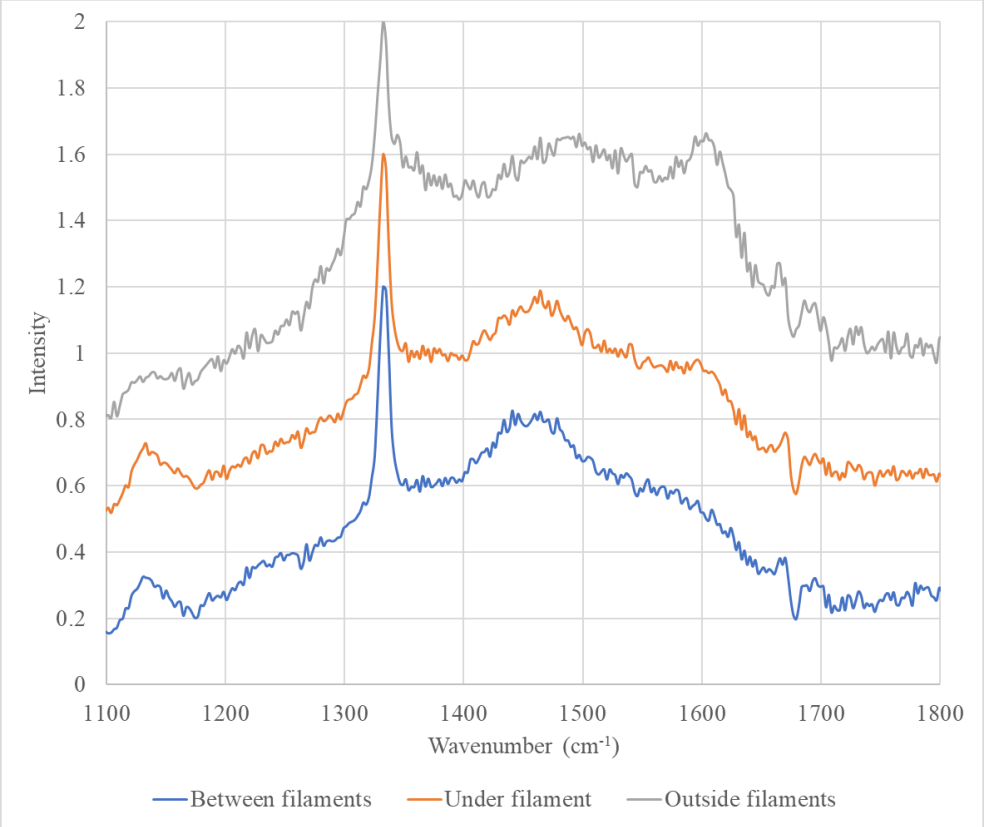

Figure A.7: Raman spectroscopy of 1 h growth with 2 filaments. All three locations show a strong diamond peak, but significant graphitic presence too.

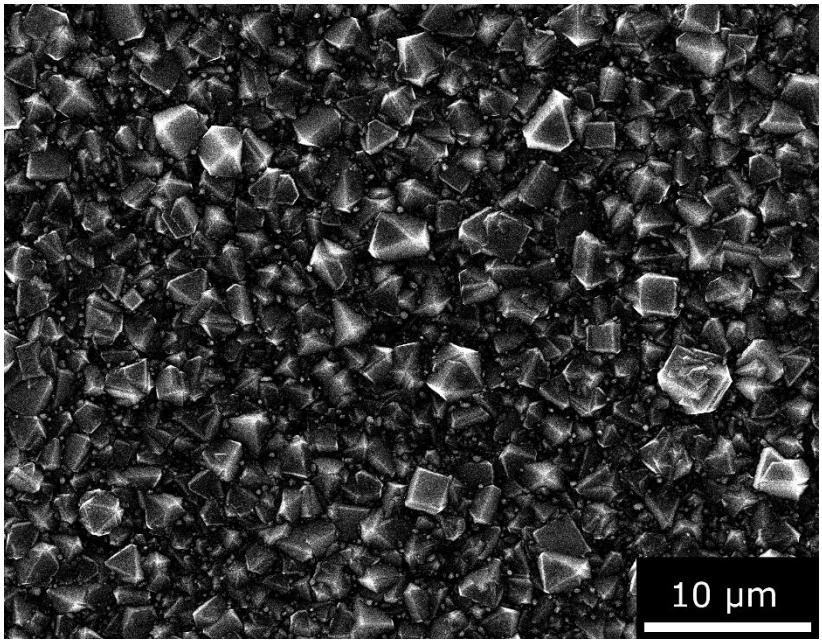

Figure A.8: SEM image of 10 h growth using the large-area hot filament reactor.

A.5 Conclusions and future work

Following a period of reactor design and redesign, a functioning large-area hot filament diamond CVD reactor has been built, and high-quality growth with good uniformity has been performed on Si wafers 50 × 50 mm in size.

The larger power supply that has now been installed should enable larger areas to be grown with better control, once suitable cooling has been tested.

Scaling-up should be continued, with the new power supply able run the reactor at up to 16 filaments, 200 mm long, which should allow substrates up to 150 mm to be grown on. Given how close the LA HF reactor is to being ready for large scale testing, the reactor should be capable of depositing polycrystalline diamond uniformly on 100 mm Si samples by early 2022.

References

1 *EU Pat.*, EP3155631A1, 2017.

2 NeoCoat Hot Filament Diamond CVD Systems, http://sekidiamond.com/neocoat/, Accessed 22/09/21.

Appendix B: EDX data of self-assembled polymer micelles

B.1 Micelles prior to conversion

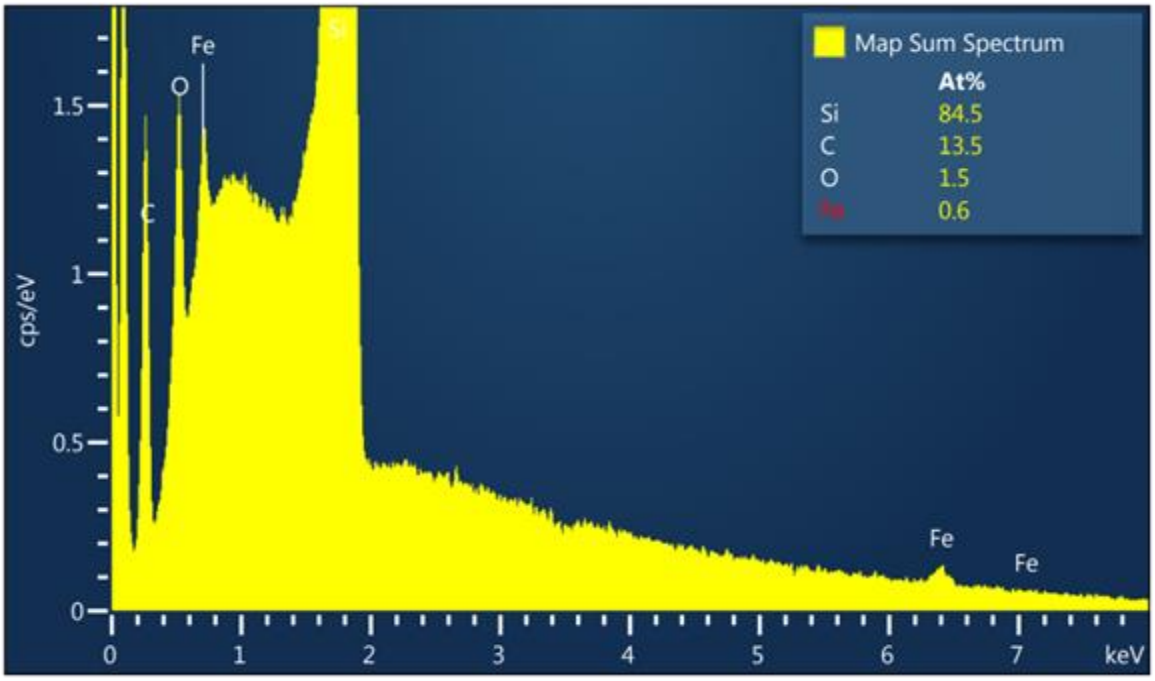

Figure B.1: EDX plot of micelles prior to conversion. An Fe peak is present, showing the polymer seed component.

B.2 Micelles following conversion

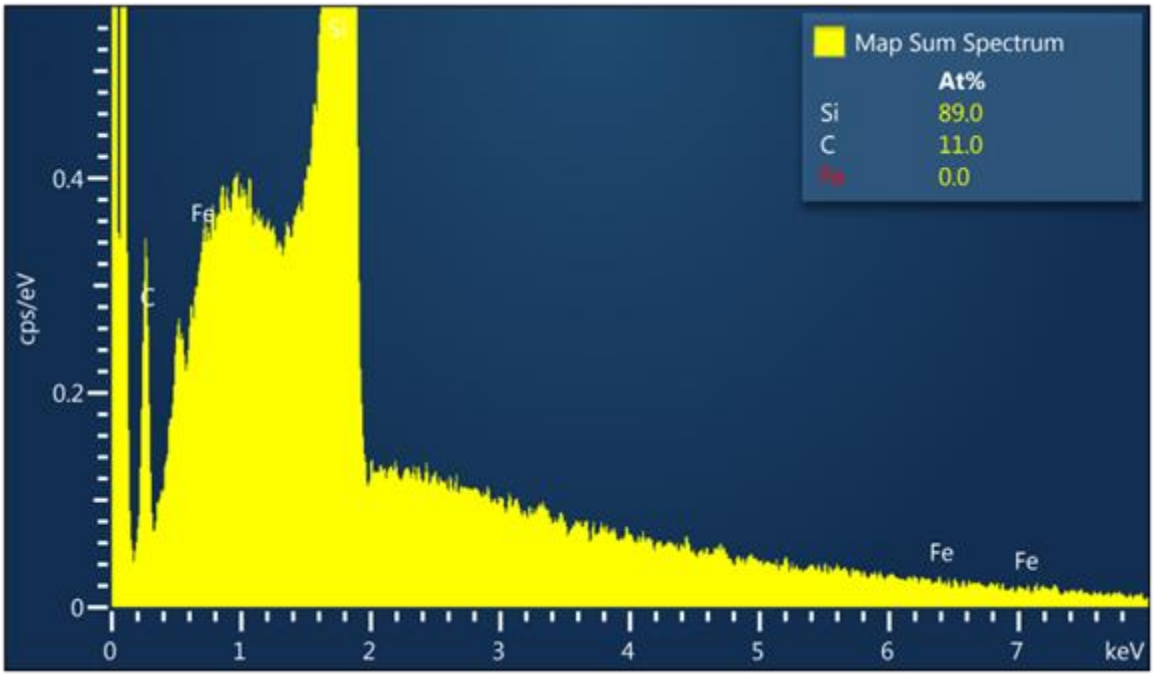

Figure B.2: EDX plot of micelles following conversion. The Fe peak is no longer present.